

UNIVERSITY OF MISKOLC

Faculty of Earth Science and Engineering

Institute of Mineralogy and Geology



MISKOLCI
E G Y E T E M
UNIVERSITY OF MISKOLC

Mikoviny Samuel Doctoral School of Earth Sciences

Head of the Doctoral School: Dr. Péter Szűcs, professor

**“GEOLOGICAL AND GENETIC MODEL OF METAL-ORGANIC
COMPOUNDS FORMATION IN LATE PALAEOZOIC ORGANIC-RICH
SEDIMENTS, USING EXAMPLES FROM HUNGARY AND
KAZAKHSTAN”**

PhD DISSERTATION

By
MEDET JUNUSSOV

Scientific supervisors:

Prof. Dr. Ferenc Mádai, & Dr. Hámorné Vidó Mária habil

Miskolc, 2022

HUNGARY

TABLE OF CONTENTS

List of Figures	v
1. Introduction	1
1.1 Distribution of ore association of OM.....	1
1.2 Definition of gold associated with OM	3
1.3 Debate on the genetic association of gold mineralisation with OM.....	4
1.4 Aim and objectives.....	7
1.5 Methodology	7
1.6 Study area: Hungary and Kazakhstan	8
2. Regional geology of the mineral deposits	9
2.1 Geological settings of W-Mecsek	9
2.1.1 Exploration history of W-Mecsek	9
2.1.2 Tectonic and magmatic settings of W-Mecsek.....	10
2.1.3 Stratigraphy of W-Mecsek	16
2.1.4 Ore mineralisation in the organic-rich sedimentary formation.....	18
2.2 Geological settings of Bakyrchik	20
2.2.1 Exploration history of Bakyrchik.....	20
2.2.2 Tectonic and magmatic settings of Bakyrchik	21
2.2.3 Stratigraphy of Bakyrchik	24
2.2.4 Ore mineralisation in the organic-rich sedimentary formation.....	26
3. Samples and Methods	26
3.1 Sample collection and sample preparation	26
3.1.1 Sampling procedures of W-Mecsek	27
3.1.2 Sampling procedures of Bakyrchik	28
3.2 Sample preparation of W-Mecsek and Bakyrchik	30
3.3 Analytical methods for ore minerals	31
3.3.1 Optical microscopy and electron microscopy	31
3.4 Analytical methods for OM	34
3.4.1 Organic Petrology	34
3.4.2 Infrared analysis	34
3.4.3 Raman analysis	34
3.4.4 Organic elemental analyser	35
3.4.5 Total organic content (TOC)	35
3.4.6 Bitumen and kerogen extraction.....	35
3.5 Experimental methods for samples in W-Mecsek and Bakyrchik	36
3.5.1 An experiment of samples in W-Mecsek	37
3.5.2 An experiment of samples in Bakyrchik	38

4. Microscopic petrography of W-Mecsek and Bakyrchik samples	39
4.1 Microscopic petrography of W-Mecsek samples	39
4.2 Microscopic petrography of Bakyrchik samples.....	41
5. Analytical and experimental results	42
5.1 The results of W-Mecsek samples	42
5.1.1 Organic petrology and vitrinite reflectance of W-Mecsek samples.....	42
5.1.2 Ore mineralogy	45
5.1.3 Mineralogical and chemical composition.....	46
5.1.4 Electron microscopic observation of OM and ore minerals	46
5.1.5 X-Ray maps of OM for carbon and sulphur content	48
5.1.6 Thermal maturity and reflectance.....	50
5.1.7 Total organic content (TOC) and organic elemental (H, N, S) analysis.....	53
5.1.8 Functional group composition and soluble OM analysis	54
5.1.9 Sequential extraction experimental results.....	55
5.1.10 LA-ICP-MS.....	56
5.2 The results of Bakyrchik	59
5.2.1 Organic Petrology	59
5.2.2 Ore mineralogy	62
5.2.3 Mineralogical and chemical composition.....	63
5.2.4 Electron microscopic observation of OM and ore minerals	63
5.2.5 X-ray maps of OM for carbon and sulphur	65
5.2.6 Thermal maturity and reflectance.....	66
5.2.7 Total organic content (TOC) and organic elemental (H, N, S) analysis.....	69
5.2.8 Functional group composition and soluble OM analysis	69
5.2.9 Experimental results.....	71
5.2.10 LA-ICP-MS.....	74
6. Discussion	76
6.1 W-Mecsek: geological occurrence and genetic model	76
6.1.1 Source of OM and Au	76
6.1.2 Generation and maturation of OM	76
6.1.3 Migration and entrapment of OM and Au.....	80
6.1.4 Geological model and genetic linkage of OM and Au	83
6.2 Bakyrchik: geological occurrence and genetic model	84
6.2.1 Source of OM and Au	85
6.2.2 Generation and maturation of OM and Au.....	85
6.2.3 Migration and entrapment of OM and Au.....	87
6.2.4 Geological model and genetic linkage of OM and Au	88
6.3 Summary: Similarity and differences between W-Mecsek and Bakyrchik	91

6.4	Further investigation works	93
7.	Conclusions	93
8.	References	95
9.	Appendices	119

List of Figures

Figure 1 Variscan orogenic belt, mineralised by gold deposits within the zone of tropical climate during Late Carboniferous and relationships for gold mineralisation and coal deposition along Variscan Orogen, and means of supply of gold to coal (detrital l, hydrothermal). (modified after (Boucot, et al., 2013); (Parnell, 2019)).....	2
Figure 2 Diverse origins of OM (bitumens), relative to sedimentary	6
Figure 3 (a) Map of Hungary with the location of the Mecsek Mountains. (b) Geological map of the Mecsek Mountains with the distribution of the Kővágószőlős Sandstone Formation (KSF) and the Boda Claystone Formation; modified after (Konrád & Sebe, 2010) (Emese, et al., 2022). Legend: 1-Neogene sediments; 2-Jurassic and Cretaceous sediments and Cretaceous volcanic rocks; 3-Triassic sediments (sandstones, carbonates and evaporites); 4-Late Permian-Triassic Kővágószőlős Sandstone Fm; 5-Late Permian Boda Claystone Fm; 6-Palaeozoic; 7-fault; 8-strike-slip fault; 9-thrust fault; 10-syncline and anticline; 11-W-Mecsek U ore deposit.....	11
Figure 4 Pre-Alpine structural units of the Tisza Mega-unit.....	12
Figure 5 Exposure of the Mórággy Granite (After (Szederkényi, 1987)).....	13
Figure 6 Paleogeographic reconstruction of Late Palaeozoic continental basin	16
Figure 8 Geological cross-section of the Northern (A) – Southern (A') the direction in the Western-Mecsek Anticline (modified after (Barabás, 2013)). Legend: 1-Neogen; 2-Mecsek coal formation (Late Triassic-Early Jurassic); 3-Misina Formation (Middle Triassic); 4-Patacs Siltstone Formation and Jakabhegy Sandstone Formation (Early-Middle Triassic); 5 Kővágószőlős Sandstone Formation with uranium ore mineralisation (Late Permian-Early Jurassic); 6-Boda Siltstone Formation; 7-Structural zones.....	19
Figure 9 Tectonic framework.....	21
Figure 10 a) Geological map of the Chara shear zone, simplified from (Buslov, et al., 2004), (Daukeev, et al., 2008); b) Geological map of the Bakyrchik ore field. Simplified from (Daukeev, et al., 2004).....	23
Figure 11 General schematic development of magmatic intrusions of the Kunush complex; (modified after (Kuzmina, 2011)).....	23
Figure 12 Lithostratigraphic column of Qalba gold province showing lithological	24
Early Hercynian island-arc level (D ₃ -C ₁) related to derivatives of andesite-basaltic island volcanism and synchronous argillaceous-siliceous-calcareous and flysch deposits. The ore-bearing rocks are represented by effusive rocks and subvolcanic bodies with basic and intermediate compositions, siliceous siltstones, and limestones. Epigenetic gold mineralisation (pre-ore stage) is spatially related to the volcanogenic siliceous-carbonate-terrigenous formation (C _{1v2-3}) (Kuzmina 2011). (see in Figure 13).....	25

Figure 13 Geological cross-section of the Bakyrchik gold deposit (modified after Dyachkov et al., 2017).....	25
Figure 14 Overview map of a closed uranium mining area in W-Mecsek.....	27
Figure 15. An overview map of the study area (a) showing the sampling area marked with broken lines and fragments of nine samples (b) from separated three groups.	29
Figure 16 Total samples collected from both mineral deposits:	30
Figure 17 General review of samples preparations of W-Mecsek and Bakyrchik mineral deposits: a) powder samples for XRD; b) powder samples for WD-XRF; c) polished sections (upper is W-Mecsek and lower is Bakyrchik), and d) thin sections.....	31
Figure 18 LA-ICP-MS measurement on particles of OM (a) and.....	33
Figure 20 The review of one of the experiments. Sequential extraction method:.....	37
Figure 22 General overview of drill core samples (between 883-886 m).....	40
Figure 23 Transmitted microscopy images under plane-polarised light of hydrothermal quartz veins (qtz) with (a) opaque minerals (op) and (b) OM (typical pyrobitumen) in the samples Bak 2.5. Scale: 200 μm	42
Figure 26 Uraninite minerals (white greyish grains, indicated by red arrows) associated with OM: a) uraninite with pyrobitumen (PB); b) uraninite with vitrinite (V1).....	45
Figure 27 EMPA-BSE images with EDS measurement showing chemical	47
Figure 28 EPMA-BSE images of euhedral pyrite grains with arsenic content in grey (a), and sulfosalt minerals with high arsenic (and copper) element (b), (unit in wt%) of the sample – WH2-72.	48
Figure 29 EMPA-EDS X-Ray map with quantitative results of fractured vitrinite particle (V1) associated with framboidal pyrites in quartz matrix: BSE image (a); EDS measurement (b), and X-Ray mapping of the image (c and d): in the image (c) fractured vitrinite is shown in blue within the rock matrixes (denoted albite in cyan, quartz in green, K-feldspar in brown, pyrite in dark blue and titanium oxide in white); and in the image (d) sulphur content of vitrinite (dark orange) and pyrite (light orange) with surrounding silicates (in green quartz and dark green K-feldspar) from the sample – WH2-76. (OM-organic matter and py-pyrite).....	49
Figure 30 Raman microscopy measurement of non-fluorescing bitumen (B1) and pyrobitumen (PB), and autochthonous vitrinite telinite (V1) showing Raman spectra (left side) of D and G peaks and optical photomicrographs (right side) under cross-polarized light.....	52
Figure 31 FTIR analysis and comparison of organic fractions: (a) molecular structure of lignin with silica nanocomposites (modified from (Weizhen, et al., 2017)); (b) OM with rock matrices of carbonate free, shown the sample of WH2-77 (indicated no carbonyl in frame).	54
Figure 33 Representative time-resolved LA-ICP-MS depth profiles for Au, Ag, U and Th along a liner track through grains of OM in the sample of WH-2-065. (Scale 100 μm in the photomicrograph).	58

Figure 34 Representative time-resolved LA-ICP-MS depth profiles for Au and Ag along a liner track through pyrite grains of pyrite in the sample of WH-2-072.....	58
Figure 35 Photomicrographs of fracked reworked, (a) angular vitrinite (V1) particles.....	60
Figure 36 Photomicrographs of solid bitumen normal reflected light in oil immersion filling in hydrothermal quartz veins: a) very tiny filamentous and diffuse solid bitumen (B1) (sample Bak 2); b) filamentous and diffuse solid bitumen with pyrobitumen (sample Bak 1) and the pyrobitumen spongy feature at left indicates that asphaltene type solid bitumen could transform to pyrobitumen; c) vitrinite, telinite sample Bak 5); d) Egg like a humic type of vitrinite with the growth of euhedral pyrite crystals (py) in the middle and diffuse solid bitumen in the surrounding (sample Bak 1). Left: parallel polarised light in oil immersion. Right: ultra-violet fluorescent excitation, uranium-containing fluid inclusion is visible. Scale: 10 μm	61
Figure 38 Photomicrographs of ore microscopy: a) cubic pyrite (py), acicular.....	62
Figure 39 BSE images showing the chemical composition of vitrinite (V) and.....	64
Figure 41 EMPA-EDS X-Ray map for vitrinite: BSE image (a) and EDS.....	65
Figure 42 Raman microscopy measurement of reworked vitrinite (V), two types of pyrobitumen (PB) and kerogen with Raman spectra (a) of D and G peaks, and optical photomicrographs under cross-polarized light (b – kerogen, c – vitrinite, and d – B1 and PB). Scale: 10 μm	68
Figure 43. FTIR analysis and comparison of organic fractions: (a) molecular structure of lignin with silica nanocomposites (modified from (Weizhen, et al., 2017)); (b) OM with rock matrices from the rock samples (no carbonyl is indicated in the frame).	71
Figure 44 Triangular diagram of the gold in pyrobitumens, vitrinite, Arsenopyrite, and pyrite ratio in three sample groups of a total of nine samples (Denoted by colour: black for group I; violet for group II, red for group III, and samples in the brackets).....	72
Figure 45 LA-ICP-MS images of spot analyses on grains of OM (light grey).	75
Figure 46 Representative time-resolved LA-ICP-MS depth profiles for Au, Ag, C.....	75
Figure 48 EMPA-BSE images of primary vitrinite V1 showing framboidal pyrite growths of bacterial colonies comprising bacterial sulfate-reduction in the OM texture. Black – OM, dark grey – quartz, grey – dolomite, white grey – Fe-Mg carbonate, imaged from the sample WH2-073.	79
Figure 49 Primary syngenetic model of the accumulation of uranium ore deposit in W-Mecsek. (modified after (Barabás, 2013), and (Virágh & Vincze, 1967))Legend: 1) Fluvial floodplain sediment; 2) Peat-forming sediments; 3) Different groundwater tables; 4) Ore accumulation lenses; 5) Sub-surface water flow; 6) Oxydated and intermediate rock types; 7) Intermediate and reductive rocks border; 8) Mean groundwater level.	81
Figure 25 Photomicrographs in reflected normal light and fluorescence UV light	121
Figure 32 LA-ICP-MS data: a) LA-ICP-MS representative time-resolved depth	123
Figure 37 Reflected light micrographs. Bakyrchik deposit: Rock sample of “A”: (a) Hexahedral pyrite crystal with acicular-prismatic arsenopyrite; (b) Pyrite framboidal aggregate; (c) Pentagonal	

pyrite cross-sections and tabular arsenopyrite twin; (d) hexahedral pyrite in growth with tabular arsenopyrite; (e) Tabular-arsenopyrite twin. Rock sample of “B”: (f) Hexahedral crystal of pyrite.

.....	123
Figure 40 Micrographs of sulphide minerals with points for elemental measurement: a) acicular-prismatic arsenopyrite associated with cubic pyrite crystals, b) tabular-arsenopyrite twin, c) pentahedral pyrite crystal with tabular-arsenopyrite twin, d) integration of acicular-prismatic arsenopyrite and pentahedral pyrite crystal; e) hexahedral pyrite crystal; f) tabular arsenopyrite crystal, g) cubic pyrite crystal with galena inclusion, h) acicular-prismatic arsenopyrite with crystals of cubic pyrite. (asp-arsenopyrite, py-pyrite, gn-galena).....	125
Figure 47 Representative time-resolved LA-ICP-MS depth profiles for Au, Ag, As, Pt, Fe and S along a liner track through grains of arsenopyrite in the sample of Bak 2.4. (Scale is 100 µm in the photomicrograph).....	125
Figure 50 Schematic model formation of gold within OM and arsenic sulfide minerals of W-Mecsek.....	126
Figure 51 Schematic model of the formation of gold compounds of OM and arsenic sulfide minerals of Bakyrchik.....	127

List of Tables:

Table 1 Total samples collection of W-Mecsek.....	28
Table 2 Total samples collection of Bakyrchik.....	29
Table 4 Vitrinite reflectance measurements of the six selected rock samples.	44
Table 6 Relevant Raman parameters for organic materials for the selected rock.....	52
Table 7 Total organic carbon (TOC %), H, N and S of eight whole-rock samples.	53
Table 8 Results of extracted metals from the whole rock samples in the three stages.	55
Table 13 Elemental concentration (on average wt%) in textures of arsenic.....	65
Table 14 Relevant parameters of the Raman spectra of selected samples (Bak 1, Bak 2, Bak 2.4, Bak 2.5) for estimated temperatures and estimated organic maturity.....	68
Table 15 Total organic carbon (TOC %) H, N and S of nine whole-rock samples.	69
Table 17 Similarity and differences between studied mineral deposits.	92
Table 3 Sampling preparation of W-Mecsek and Bakyrchik.....	128
Table 5 Quantitative results of minerals and amorphous organic matter.....	128
Table 9 LA-ICP-MS spot analyses measurement on the OM of the sample.....	129
Table 10 LA-ICP-MS spot analyses measurement on the grains of pyrite of.....	130
Table 11 Continued.....	130
Table 12 Quantitative results for minerals and amorphous matter.....	131
Table 16 Concentrations of extracted noble metals of whole-rock samples at the.....	132

ACKNOWLEDGEMENTS

During my PhD study at the University of Miskolc, I have been supported by many people who motivated and contributed to completing this work.

Firstly, I would like to thank my supervisors, Prof. Dr Ferenc Má dai and Dr Mária Hámorné Vidó, for their constant encouragement and considerate supervision throughout the whole doctoral program. Then, my special thanks to Prof. Dr Földessy János (for the W-Mecsek uranium ore deposit) and Dr Zamzagul Ahmetova (for samples of the Bakyrchik gold deposit) for supporting the rock samples of two mineral deposits.

Dr Kristály Ferenc of the Institute of Mineralogy and Geology, University of Miskolc is thanked for the measuring of XRPD and EMPA. Dr Tóth Tivadar and Dr Fintor Krisztián of the Department of Mineralogy and Geochemistry, University of Szeged are thanked for supporting me in using the laboratory infrastructure and carrying out the Raman measurement. Dr Edit Király of the Mining and Geological Survey of Hungary is thanked for helping me with the LA-ICP-MS measurement.

Special thanks to the Institute of Chemistry, at the University of Miskolc, for access to the laboratories, supply of chemicals, and assistance during the experimental works and analytical measurements. Namely thanks to Dr Olivér Bánhidi for supporting me with his advice in my sequential extraction experiment and with ICP-OES measurements, Dr Gábor Muránszky who helped me with the bitumen extraction, fractionation experiment and organic elemental measurement and Dr László Vanyorek in the kerogen separation experiment and Infrared spectroscopy measurement)

Besides my advisors, I would like to thank the reviewers: Prof. Dr János Földessy and Dr Béla Raucsik, for their insightful comments, encouragement and the challenging questions that compelled me to widen my research.

My warm gratitude to Délia Debus for sample preparations; Ferenc Móricz for cutting samples and helping me with WD-XRF measurement; and many thanks to Richard Zoltán Papp, Máté Leskó and Lívía Majoros for their help and advice in social, departmental and experimental works.

Finally, I would like to thank my parents and wife for their support and encouragement over the years - this is dedicated to them.

Medet Junussov

1. Introduction

1.1 Distribution of ore association of OM

Today, the mineral resources associated with OM provide many unresolved problems for mineral exploration (e.g. its difficulties for mineral reserve evaluation and ore body contouring, etc.) and metal extraction (its low recovery with classical technology) from metal-organic compounds formations. Because insufficient attention and investigations on metal-organic compounds formation as host rocks of varied mineral resources, investors and mineral explorations are unaware of its great potential.

OM has been utilised for more than 100 years and is currently being used by the industry as raw material for some valuable metals like uranium, silver, and gold (Seredin & Finkelman, 2008). High gold and silver contents of coaly OM up to the commercial grades were first discovered at the end of the 19th century in the Wyoming and Utah coal basins of the United States (Noddack, 1936). Other research of (Goldschmidt & Peters, 1933); (Burnet, 1986); (Finkelman & Brown, 1991); (Meitov & Rodionov, 1993); (Seredin, 2007); (Seredin & Finkelman, 2008) are also deal with the gold mineralisation. The higher concentration anomalies of precious metals often occur in sedimentary basins with the basement of various compositions of granites, volcanic rocks, and other sediments like shales and limestones (Seredin & Finkelman, 2008). These basins are located within the Au- and PGE-bearing districts or far away from known ore deposits and occurrences. The OM-rich rocks contain tens, hundreds, or thousands of times greater gold concentrations to the Clark value (Seredin, 2007). For this reason, the anomalously high concentrations of gold deposits in the coal basins may have economic potential for primary extraction or by-product recovery (Seredin, 2007); (Seredin & Finkelman, 2008).

Other interesting objects OM are directly associated with the largest deposits of uranium, gold, polymetals, phosphor, and rare elements. Globally, it is widely named giant deposits such as Phosphoria (Western USA), Broken Hill (Australia), Carlin (Nevada), Mount Isa (Australia), Witwatersrand (South Africa), McArthur River (Australia), Mansfield (USA), Rammelsberg (Germany), Outokumpu (Finland).

Mineral deposits associated with OM are widely distributed globally because more organic carbon compounds originate and propagate in sedimentary rock. One of the largest ore mineralisation with organic-rich sedimentary formations on earth is South China, with 1600 km² in a west-east direction, 18,300 km² in Sweden, and more than 1000 km² in eastern and central USA. Economically, the mineral deposits are potential targets in noble

metals explorations and productions, as (Bowell, et al., 1999) reported amorphous carbon from the Getchell mine in Nevada (USA) containing 2-3 ppm Au (average grade of the whole rock), (Emsbo & Koenig, 2007) described veins of reworked OM the El Rodeo deposit (Dominican Republic) containing up to 100 ppm Au. (Hallbauer, 1986) described gold as intimately associated with hydrocarbons in the Witwatersrand (South Africa), where 40% of the gold is in reefs with carbon seams, containing the whole rock average grade of around 5-7 ppm Au.

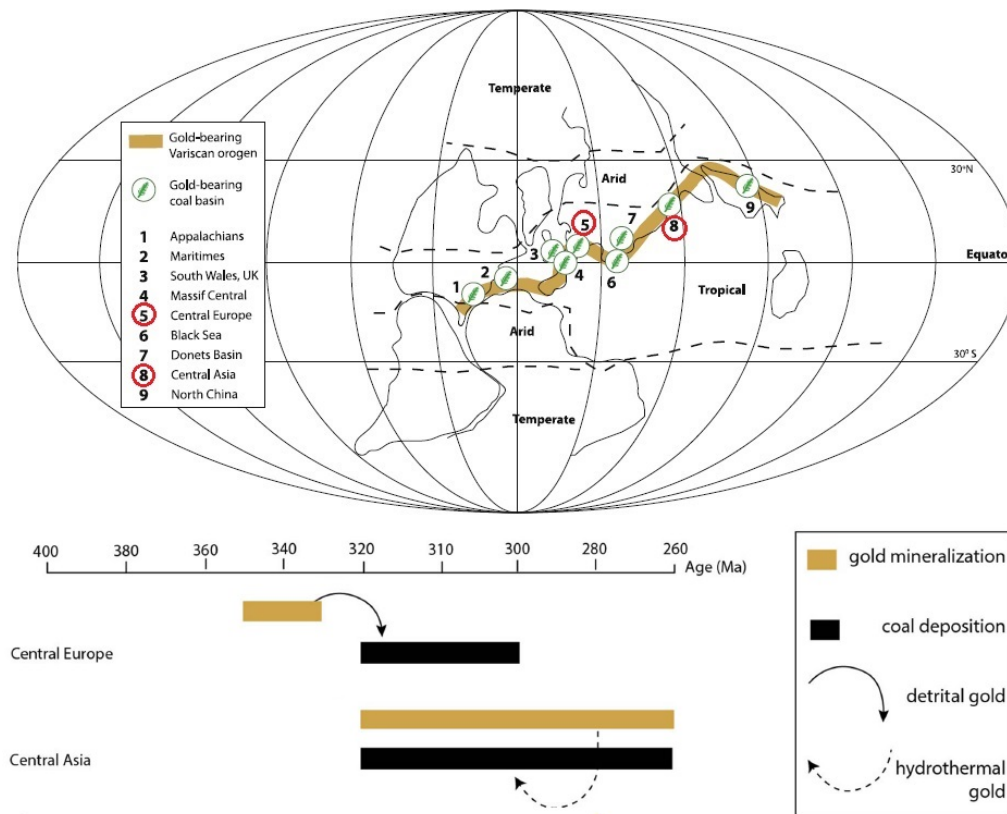


Figure 1 Variscan orogenic belt, mineralised by gold deposits within the zone of tropical climate during Late Carboniferous and relationships for gold mineralisation and coal deposition along Variscan Orogen, and means of supply of gold to coal (detrital, hydrothermal). (modified after (Boucot, et al., 2013); (Parnell, 2019)).

It is globally disturbed and enriched with gold in organic-rich sedimentary formations, is related to Carboniferous Variscan cycling of gold into a global coal reservoirs (Figure 1), and was mineralised by gold ore in coal basins from 410 to 310 Ma

over 10,000 km from the Appalachians to China (Parnell, 2019), which is the studied deposits, located in Central Europe and Central Asia, are considered in more detail below.

Central Europe on gold mineralisation occurs in palaeoplacers in several basins and mineralises coalified plant material (Klominsky, et al., 1979); (Malec, et al., 2012.). It is variably mixed with silver, mercury, platinum and selenium. Traces of gold have been detected in pyrite in coal (Bielowicz & Misiak, 2017), and the resulting about 1 ppm gold (Franus, et al., 2015).

In Central Asia, gold mineralisation overlapped with sedimentation in coal-bearing sandstone-mudrock successions in Kazakhstan (Levitan, 2008). The gold occurs in carbonaceous sediments and cross-cutting quartz veins and is particularly concentrated near thrust surfaces. It resides in pyrite and arsenopyrite in the quartz at up to 150 ppm (Levitan, 2008).

1.2 Definition of gold associated with OM

The ore metal association with the OM has been expressed as metal-organic compounds (or complexes) in many publications on gold associated with OM in ore deposits (Saxby, 1976); (Langmuir, 1979); (Giordano, 1994); (Giordano & Kharaka, 1994). As (Langmuir, 1979); and (Giordano & Kharaka, 1994) defined metal-organic compounds as when the metal cation is structurally attached to one or more organic ligands by direct bonding to electron donor atoms other than carbon most commonly, they are oxygen, sulphur, and nitrogen.

Organic materials are often found in gold-bearing sulphide deposits, where gold is invisible (Jiuling L., et al., 1997); arsenic-rich sulphide minerals are usually enriched in gold, which is genetically associated with organic materials (Hanping, et al., 1999). Therefore, a positive correlation exists between gold content and organic carbon, an active chemical agent in ore-forming processes (Parnell, et al., 1993); (Giordano, 1994); (Giordano & Kharaka, 1994). It was assumed that gold sulphide ores and organic materials are deposited together as a result of precipitation caused by changes in temperature, pressure, and pH of the gold-bearing fluid (Romberger, 1988) with the formation of metal-organic compounds, where OM can play a significant role in the metallogenesis of a sulphide gold deposit (Gatellier & Disnar, 1989); (Parnell & McCready, 2000); (Ross, et al., 2011). The so-called “invisible gold” was first described by (Bürg, 1930), is *ionic gold* (or submicroscopic form) in the form of a solid solution structurally binding in arsenian pyrite (Cabri, et al., 1989); (Cook & Chryssoulis, 1990); (Fuxin, et al., 2001);

(Vikent'ev, et al., 2006); (Wu, et al., 2016); (Volkov & Sidorov, 2017); (Osovetsky, 2017); (Large & Maslennikov, 2020), which is not detectable even by electron microscopy (Cook & Chryssoulis, 1990); (Large & Maslennikov, 2020),. It accounts for 10-15 % of world gold production, and gold content generally increases with arsenic content (Fleet, et al., 1993), possibly related to arsenic content in the host mineral (Cabri, et al., 1989), which is common in arsenian pyrite (Cook & Chryssoulis, 1990), since gold can substitute Fe in the arsenian pyrite lattice (Wu & Delbove, 1989).

As direct thermal cracking of OM at great burial depths (Waples, 2002), which it is generally related to magmatic activity and hydrothermal fluid convection at temperatures from 60°C to 400°C (Simoneit, 1994), (Simoneit, 2000) and (Simoneit, 2018) accumulation of metals occurred in the transformation from liquid bitumen, later precipitated as solid bitumen and, finally into solid bitumen. Solid bitumen, as defined by (Stasiuk, 1997), is a high-temperature form of solid bitumen (Jacob, 1989), a highly aromatic and insoluble bituminous substance (Glikson, et al., 2000); (Huc, et al., 2000) of higher rank (more than Ro=2%). It has no fluorescence or weak (brown, wavelength > 650 nm) fluorescence (Glikson, et al., 2000) and occurs as petroleum (Rogers, et al., 1974); (Milner, et al., 1977); (Hunt, 1978); (Jacob, 1989).

Nevertheless, gold extraction of OM is difficult, even in using a well-known gold cyanide complex, OM is difficult to treat and requires pre-cyanidation processes to liberate the gold. The main reasons are gold in intimate association with and locked in the carbonaceous matter and sulphide minerals as gold in solid solution (Osseo-Asare, et al., 1984).

1.3 Debate on the genetic association of gold mineralisation with OM

The source of gold, origin roles of the OM and thermal alteration of OM in the deposits have been extensively debated and are still not quite clear.

Different models regarding the gold source have been proposed: (1) The source bed hypothesis suggests that gold is derived mainly from the gold-rich strata during the deep circulation of meteoric water. The water was driven either by high geothermal gradients during regional extension and accompanying magmatism (Liu & Geng, 1985); (Hofstra, 1995); (Ilchik & Barton, 1997) or as a result of regional metamorphism and dehydration of these same metasedimentary rocks (Philips & Powell, 1993). Some researchers have proposed that the gold, heat, and fluid (formation water) come from the host rocks. (2) In models proposing a magmatic link, gold is derived from a stock or pluton (Sillitoe &

Bonham, 1990); (Zhu, et al., 1998); (Liu, et al., 1999). A variation on the magmatic model proposes that plutons simply provide the thermal energy necessary for focussing a hydrothermal system (Arehart, et al., 1993); (Yang & Dong, 1994). In this case, gold was derived largely from sedimentary rocks with little or no contribution from the plutons. (3) The mixed source model suggests that gold and fluid are derived from multiple sources, including host rocks, magmatic rocks, and lower or middle crustal rocks (Tosdal, et al., 1998). A few researchers have proposed that the gold is mainly derived from the mantle (Ni, et al., 1997); (Zhu, et al., 1998) or a mixture of mantle and crust (Zhu, et al., 1998). Ore deposits are closely associated with OM since the host rocks, and the ores typically contain variable amounts of OM.

Concerning the origin and role of OM, two theories have been debated. According to the first theory, the evolution of OM is a separate event, and the OM and gold are related only in so far as they accumulated in the same structural traps (Presnell, 1993). The second theory considers OM the dominating factor controlling leaching, migration, and deposition (Lin, et al., 1993.); (Liu, et al., 1994). The formation of metal-organic compounds has been investigated by many authors (Radtke & Scheiner, 1970); (Baskakova, 1970); (Saxby, 1976); (Emsbo & Koenig, 2007); (Parnell & McCready, 2000); (Ross, et al., 2011); (Migdisov, et al., 2017) in coal, bitumen and solid bitumens in which gold occurs in soluble and insoluble fractions from a few tenths of ppb to several thousands of ppm (Crocket, 1991); (Wood, 1996); (Razvozhzaeva, et al., 2002); (Ross, et al., 2011); (Fuchs, et al., 2016). The role of metal-organic compounds in the migration and entrapment of gold has been reported by several authors (Baskakova, 1970); (Saxby, 1976); (Boyle, 1979); (Giordano, 2000); (Migdisov, et al., 2017); (Simoneit, 2000) and (Simoneit, 2018). The OM of phenolic aromatic and thiophenic sulphur compounds in hot aqueous ore fluids can favour the transportation of metals (Giordano & Kharaka, 1994); (Giordano, 2000).

The concept of (Parnell, et al., 1993); (Parnell, 2019) about the origin of OM (bitumen) in ore deposits, which is still relevant, following several diverse origins (Figure 2):

1. Diagenetic origin: locally derived under immature thermal conditions, i.e., before source rock enters the "oil window." Bitumens of this type occur particularly within sequences of carbonate source rock and are commonly fracture-bound because of the brittle nature of the source rock.
2. Residues of petroleum are deposited along the migration pathway of petroleum or within a hydrocarbon reservoir. Solid bitumens are produced from "normal" oil by

several alteration processes including biodegradation, water washing, and deasphalting.

3. Distillates around igneous bodies which have intruded into rocks rich in organic matter. Extruded lavas may also contain distillate bitumens. Such bitumens are of very local origin. Fronts of migrated bitumen can be observed at a limited distance from many dykes and sills.

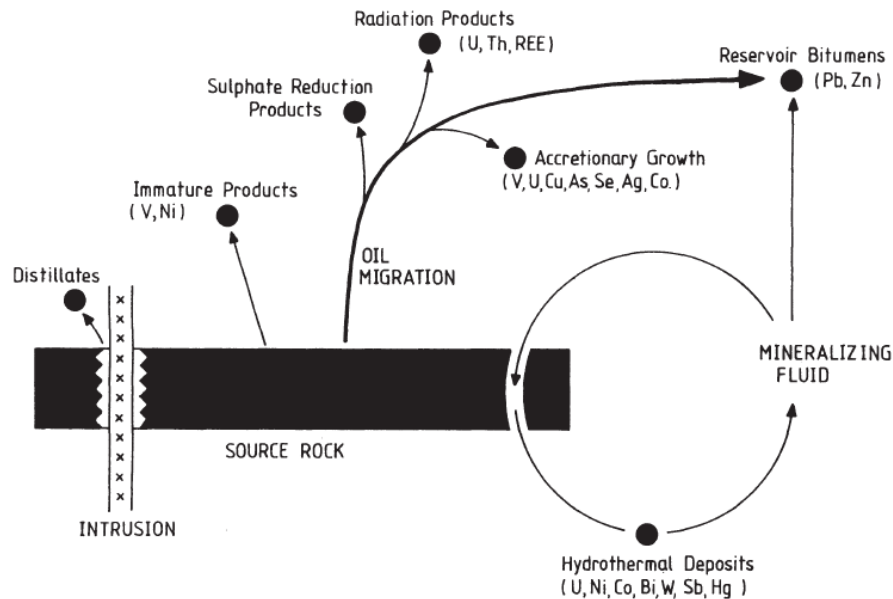


Figure 2 Diverse origins of OM (bitumens), relative to sedimentary source rock (Parnel, et al., 1993).

4. Products of OM are caught up in hydrothermal systems through distillation or leaching of organic-rich country rock by hot fluids.

5. Accretionary nodules of bitumen in sedimentary rocks which grow by progressive replacing of the rock around a nucleus.

6. Deposits of solid bitumen around radioactive minerals (uraninite, monazite, zircon, etc.), precipitated by polymerisation/condensation of fluid hydrocarbons induced by radiation.

7. Deposits of solid bitumen related to sulphate reduction processes in oil reservoirs or in migration pathways.

The thermal alteration of OM in uranium deposits is still debated. Because similar thermal alterations in OM as in uranium deposits (i.e. increased thermal maturity, aromatisation, and decreased H/C ratio) are described in the works of (Eakin & Gize,

1992); (Sýkorová, et al., 2016); and (Machovič, et al., 2021); and as hydrothermal deposits of gold and base metals are described by (Parnel, et al., 1993); (Glikson, et al., 2000).

1.4 Aim and objectives

Several research papers, petrographical and geochemical investigations in Hungary and Kazakhstan, have been published on the organic-rich sedimentary uranium ore or gold deposits of W-Mecsek and Bakyrchik. Still they are rather general and have considerations on the aspects of gold mineralisation within sulphide ores, but no OM. The primary objective of this study is to bring some new concepts as to the role of OM in the formation of ore deposits. On a broad scale, it is hoped that this study will throw some light on the role of OM in hydrothermal ore-forming processes. The secondary objective is to contribute to understand the source of OM, and gold transport and preservation within OM in the deposits. The first objective was attained through (1) determination of the total organic carbon content and organic components; (2) establishing the degree of maturation of the OM; (3) analysis of the extractable hydrocarbons in the ores; (4) observation of the occurrence of the OM in the ores; (5) observation of ore association with OM; (6) determination of gold concentration in OM; (7) comparison of gold values between OM and arsenian pyrite. The above objectives have enabled us to infer the source of the OM in the ores (autochthonous versus allochthonous) and to evaluate the association between the gold mineralisation and the maturation of the OM. Furthermore, a sequential extraction experiment was conducted to liberate gold from soluble fractions of OM and ore minerals closely associated with OM.

1.5 Methodology

Geochemical investigations of two mineral deposits were selected for sampling, analytical observation, and laboratory investigation to fulfil these objectives. Sampling was carried out in the ore mineralisation zone. Observation of the occurrence of OM in both deposits and the laboratory under the microscope has been carried out. Coal petrological and geochemical methods such as vitrinite reflectance, extractable organic components grouping, and organic elemental analysis of the samples were used to determine the type, content, maturation, and biomarkers of the OM in the samples. A sequential extraction experiment to determine the gold concentration in OM (and arsenic sulphide minerals) was carried out for the possible contribution of OM to gold enrichment. Samples of organic-

rich sedimentary rocks from the ore mineralisation zone were analysed for Au and Ag and other trace elements (As, Cu, Zn, and Pb), including radioactive elements and platinum group elements (PGE). The ICP-OES and LA-ICP-MS methods were adopted to analyse these elements and to determine (1) their mobility during hydrothermal alterations, (2) whether the mantle was a possible source of Au mineralisation, and (3) geochemical prospecting possibilities. The samples' Au, Ag, and As contents were analysed to examine the possible relationship between their enrichment and association with OM. The type, content, maturation, and biomarkers of the OM in the samples were compared to two deposits to verify the significance of the allochthonous OM and the genetic relationship between OM and gold mineralisation. The precious element patterns of the samples were compared with OM and arsenic sulphide ore minerals. The result of this study has been carried out with the published data to present an overall idea of the geology, the geochemical characteristics, and the prevailing ideas on the genesis of these deposits.

1.6 Study area: Hungary and Kazakhstan

Gold is found with various grades of other metals, mainly occurring with OM of various uranium ore deposits in Hungary, revealed in many publications, listed by (Szalay, 1954); (Benkő & Szadeczky-Kardoss, 1957); (Szalay & Almássy, 1956); (Kiss, 1958), (Kiss, 1960); (Ódor, 1969); (Varga, et al., 1972); (Kádas, 1983), (Selmeziné & Vincze, 1987). (Kádas, 1983) described that Au forms concentrations up to 2 ppm accompanied by REE (the highest Y, 1000 ppm) in the Mecsek coal basin and is found mostly in the reduced variety of Permian-Early Triassic Sandstones in the W-Mecsek Mountains (Kiss, 1958), (Kiss, 1960). Moreover, (Barabás & Konrád, 2000); and (Barabás, 2010) indicated that gold was enriched in the same area of the Permian Kővágószőlős Sandstone Formation (KSF) with high uranium content. (Barabás & Konrád, 2000); and (Barabás, 2010) found that the uranium was concentrated in carbonaceous sedimentary rocks derived from the granite of the Mórággy complex (Szalay, 1954). The uranium metal is bound by complexation and sorption by functional groups (Idiz, et al., 1986) and other metals (vanadium, manganese, and strontium) (Almássy & Szalay, 1956); (Ódor, 1967); (Szilágyi, 1971). The adsorption of the metal within organic humic acid is favourable to the cation exchange of the insoluble humic acid (Szalay, 1969). Other metals of V, Mn and Sr with elevated concentrations of the organic fractions in the Hungarian organic-rich sedimentary formations (Almássy & Szalay, 1956); (Ódor, 1967); (Szilágyi, 1971) As (Barabás, 2010) mentioned, the uranium accumulation of the Late Permian Kővágószőlős Sandstone

Formation (KSF) is closely connected on the one hand to the primary weathering processes of the denudation surface of the Late Carboniferous magmatic rocks as a primary ore formation, and on the other origin is the epigenetic dissolution from the granitoid complex underlying the host rock. The uranium migrates in the surface and subsurface waters easily. The dissolved uranium precipitates when transported to a reductive environment or highly adsorbing materials like OM, clay minerals, and iron oxides. The accumulation is usually the most intensive in the intermediate transition zone of the oxidising and reducing environment. Hydrodynamics caused the uranium to entrap in reducing sediments; the uranium would be precipitated and gradually enriched, resulting in the formation of commercial concentrations of uranium.

Kazakhstan has plenty of gold deposits in an organic-rich sedimentary sequence located in the Eastern part. They occur in the West Qalba gold-bearing belt of the Irtysh–Zaissan (or Ob-Zaissan) tectonic zone (Goldfarb, et al., 2014), is 30–100 km wide, extends northwestward for 800 km (Shcherba, 2000) The West Qalba gold-bearing belt includes >450 gold deposits within occurrences of organic-rich sedimentary formations of the Carboniferous period. Mineralisation occurs as zones with finely disseminated Au-containing pyrite–arsenopyrite ores in carbonaceous–carbonate terrigenous rocks and gold-polysulphide ores. The Bakyrchik is one of the largest Au deposits in the West Qalba gold-bearing belt of Eastern Kazakhstan. This shows that OM is more attractive for improving understandings of the origin, transport, and storage of gold with OM, which will help develop more reliable exploration programs for the OM-ore association in the deposit.

Another reason, the Bakyrchik gold deposit remains little known in international publications. Previous studies have mainly focused on the mineralogy of gold and gold-bearing fields (Kovalev, et al., 2014). Still, the source of gold, the occurrence of OM, and roles of OM in gold mineralisation are currently poorly constrained.

2. Regional geology of the mineral deposits

2.1 Geological settings of W-Mecsek

2.1.1 Exploration history of W-Mecsek

The first exploration of the uranium ore deposits started in 1952 (Miloš, 2017) by using airborne and surface radiometry in the W-Mecsek sedimentary basin. The uranium ore deposit was discovered by A. Földvári and T. Szalai in 1954 (Kassai, 1980); (Érdi-

Krausz & Harsányi, 1997). The mining started in 1956 and the extraction finished in 1997 because of the high cost of production and the mining problems of the deep operation and high temperature) (Érdi-Krausz & Harsányi, 1997). Total extracted uranium was about 21,000 t from this ore deposit (Barabás & Konrád, 2000); (Barabás, 2010); (Miloš, 2017). Since 2006, four uranium exploration project areas have been covered by seven exploration licences of the Wildhorse Energy Ltd. in the W-Mecsek Mountains and the vicinity of Bátaszék, Dinnyeberki and Máriakéménd area. Large-scale remediation activities have been carried out on the Mecsek uranium mining and processing area from 1998 to 2008 (Nuclear Power, 2022).

2.1.2 Tectonic and magmatic settings of W-Mecsek

The study area was the Mecsek Mountains which lie in the Southern Central part of Hungary, about 220 km south-west of Budapest. Its largest centre is Pécs city. On the western part of the Mecsek Mountains is found the W-Mecsek uranium ore deposit, a known extension surfaced in the vicinity of Kővágószőlős village. The Mecsek Mountains occur in the southwestern part of the Tisza Mega-unit (Haas & Hámor , 1998). The Tisza Mega-unit forms the basement of the Eastern Pannonian Basin in the southern parts of two Mega units, Transdanubia and Mid-Hungarian, and the northern part of the Mecsek-alja strike-slip fault zone (Szederkényi, et al., 2012), shown in Figure 3 a and b. The unit belongs to the Variscan orogenic collage, accreted during the Carboniferous–Permian (C-P) (Szederkényi, et al., 2012).

The large-scale displacements of the ALCAPA and Tisza Mega units led to the formation of a prevalent shear zone in the Early Oligocene to Early Miocene defined as the Mid-Hungarian Zone (the names Mid-Hungarian Fault Zone or Mid-Hungarian Shear Zone are also used) (Balla, 1984); (Csontos, et al., 1992); (Fodor, et al., 1998), (Csontos & Vörös, 2004); (Schmid, et al., 2008). Felsic and intermediate metavolcanite, serpentinite, shallow marine limestone, and dark grey radiolarite were encountered in the Mid-Hungarian zone (Haas, et al., 2010).

The Transdanubian Range Unit consists of slightly metamorphosed Variscan rocks unconformably overlain by unmetamorphosed Alpine sequences. The structural setting of the Transdanubian Range is determined by a large NE–SW trending synform accompanied by antiforms along both of its limbs (Haas, et al., 2010). In Hungary, the Transdanubian Unit has Late Permian to Jurassic sedimentary sequences with deeper water carbonates in

the Triassic and pelagic shale in the Jurassic was encountered. They were strongly affected by tectonism and generally suffered low-grade metamorphism (Árkai, 1991).

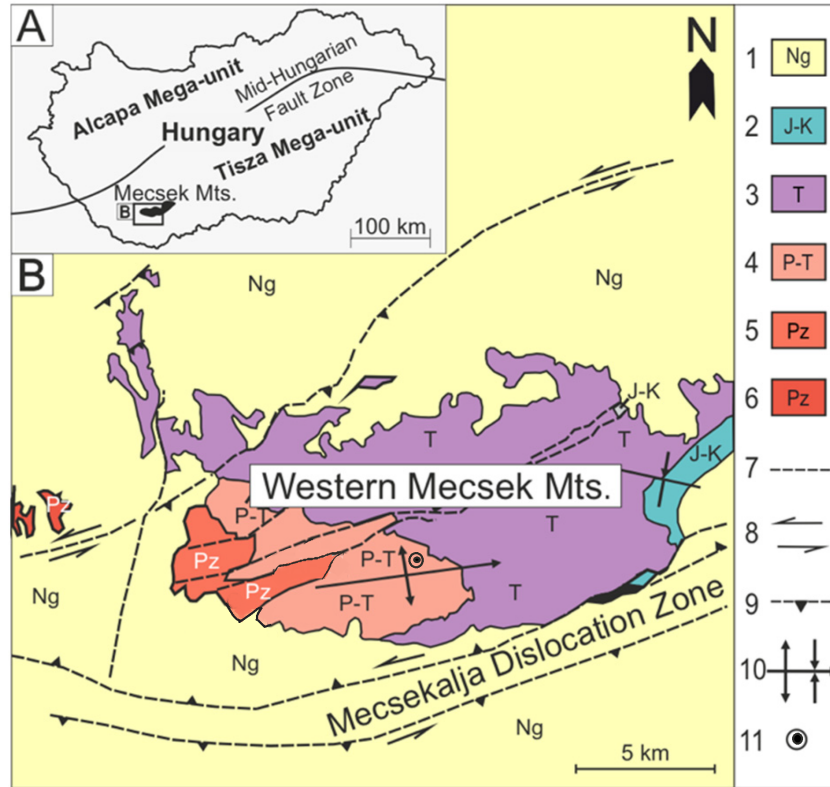


Figure 3 (a) Map of Hungary with the location of the Mecsek Mountains. (b) Geological map of the Mecsek Mountains with the distribution of the Kővágószőlős Sandstone Formation (KSF) and the Boda Claystone Formation; modified after (Konrád & Sebe, 2010) (Emese, et al., 2022). Legend: 1-Neogene sediments; 2-Jurassic and Cretaceous sediments and Cretaceous volcanic rocks; 3-Triassic sediments (sandstones, carbonates and evaporites); 4-Late Permian-Triassic Kővágószőlős Sandstone Fm; 5-Late Permian Boda Claystone Fm; 6-Palaeozoic; 7-fault; 8-strike-slip fault; 9-thrust fault; 10-syncline and anticline; 11-W-Mecsek U ore deposit.

Tectonic evolution can be established for the Hungarian part of the Tisza Mega-unit (Haas, 2012). The Tisza Mega-unit is a Variscan orogenic collage accreted during the Carboniferous–Permian, becoming part of the European continent. The European Variscan orogeny occurred when crystalline rock associations were formed by mega, macro and microfolding, shearing and blastomylonitisation. Palingenetic granite belts were formed in the axial zones of synclines. However, the Late Variscan low pressure and high-

temperature regime (late orogenic heating in the 330–270 Ma period) undoubtedly contributed to the granitisation (Haas, 2012). The post-Variscan formation has non-metamorphic (locally anchimetamorphic) molasse-type oversteps sequences that cover the crystalline basement of the Tisza Mega-unit. The Tisza Mega-unit can be subdivided into subunits bounded by fracture zones of secondary importance (Kovács, et al., 2000); they are: Slavonia–Drava Unit (Terrane) includes subunits of Babócsa and Baksa (1); Kunság Unit has subunits of Mórágý and Kőrös (2); and Békés Unit includes subunits of Kelebia, Csongrád, Battonya and Sarkadkeresztúr (3), shown in Figure 4.

The Kunság Unit extends over the area located between the Middle Hungarian

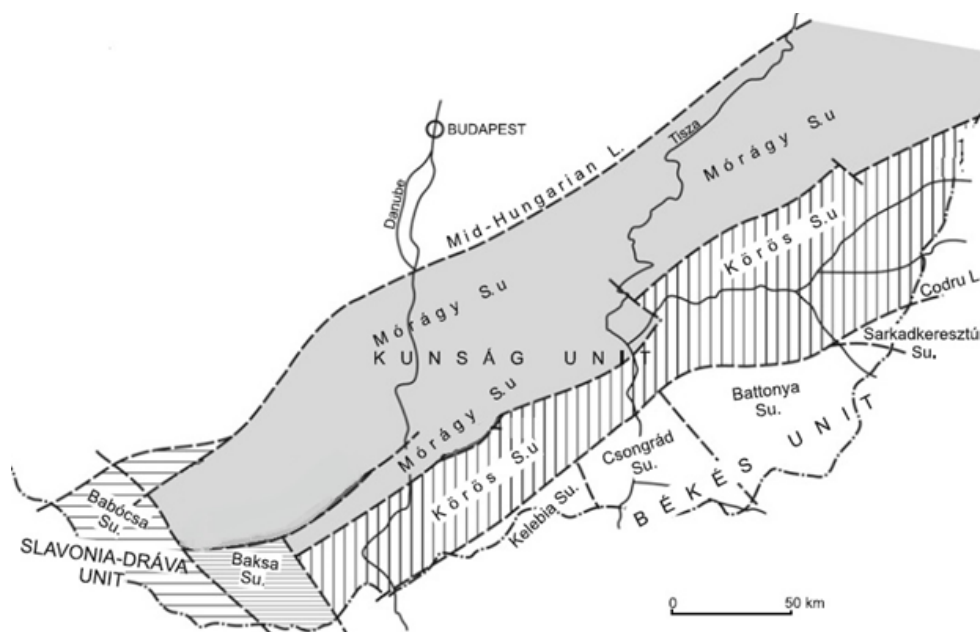


Figure 4 Pre-Alpine structural units of the Tisza Mega-unit
(After (Szederkényi, 1997)).

Lineament and the Mecsekalja Fracture Zone (Figure 4). The Kunság Unit forms the basement of the Mecsek and Villány zones (Szederkényi, 1997); (Kovács, et al., 2000). This unit includes crystalline rocks that only crop out in the Mecsek Mts (Haas, 2012), mainly granitic formations of the Mórágý complex. Variscan granitoids characterise the Mórágý Complex (basement of the Mecsek Zone). According to earlier interpretations they are (I- or S-type) "synorogenic" granitoids (Buda, 1996); (Klötzli, et al., 1999). However, according to the latest results, they were formed by continent-continent collision during the post-closure uplift stage (Buda & Dobosi, 2004). They are I-type, calc-alkaline, high-K and high-Mg-bearing large intrusion(s), with small lamprophyre-derived, ultrapotassic, Mg-Ca-

rich, low Al and Si intrusions or enclaves (durbachite). Many allanites were crystallised in the enclaves and the enclosing granitoids. Allanite is the major REE-bearing mineral which controls the whole-rock REE patterns. It is oxidised ($\text{Fe}^{3+}/\text{Fe}^{\text{tot}} \approx 0.4$), characteristic of I-type granitoids.

The Mórág complex constitutes the Mórág-Kecskemét granitoid range and the accompanying migmatite (agmatite)-gneiss mica-schist flanks on both sides. The most

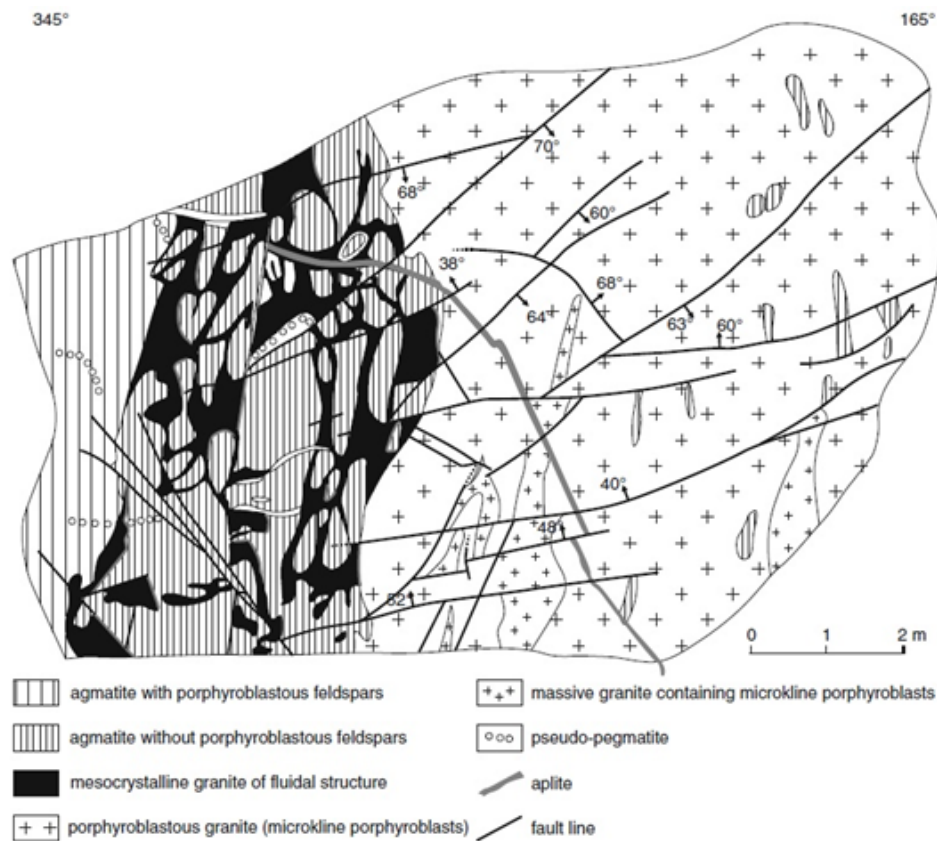


Figure 5 Exposure of the Mórág Granite (After (Szederkényi, 1987)).

characteristic part of the complex is the granitoid range itself. Forming an axial belt of an ENE-WSW-striking synclinal zone, this body is about 200 km long and 25–30 km wide, forming a continuous zone from Szigetvár (South Transdanubia) to Szolnok (central part of the Great Hungarian Plain) (Jantsky, 1979:). It is a granite-granodiorite-diorite rock association; 340–354 Ma old (U/Pb dating; (Klötzli, et al., 2004)); the 307–312 Ma age data can be regarded as cooling time (Lelkes-Felvár & Frank, 2006). It contains biotite and amphibole-rich xenolites (Figure 5) dated at 440–400 Ma (Rb/Sr ages; (Svingor & Kovách, 1981)), suggesting that a pre-Variscan metamorphic event.

Detailed investigations were conducted to establish a radioactive waste repository in the Mórág Hills (SE Mecsek). All rocks in this body are of monzonitic character. In contrast to the former hypothesis about the migmatitic (agmatite) origin of granitoids (Szádeczky-Kardoss, 1959), the major characteristics of the rock association indicate a rather plutonic than migmatitic origin (Király, 2009). The granitoids are syn-collisional, S-type, mixed meta-, and peraluminous (Buda, 1981), (Buda, 1990), (Buda, 1996). They are accompanied by crystalline schists showing typical polymetamorphism which flank the syncline. In the first phase of Variscan deformation, a Barrow-type event occurred at 6–8 kbar pressure and 14–26°C/km thermal gradients (Szederkényi, et al., 1991). In the second phase, a low-pressure/high-temperature retrogression occurred along the Mecsekalja Fracture Zone and in the eastern continuation of Mecsek Mts. (Lelkes-Felva'ri, et al., 1989) with late kinematic (322 Ma) andalusites. Subsequently, the granitic rocks were affected by multistage deformation (Maros, et al., 2010).

Paleomagnetic data bear evidence of coordinated movements of the Mecsek area with Europe from the Carboniferous to the earliest Cretaceous; after that, a major anti-clockwise rotation took place during the paroxysm of volcanism at 135 Ma or somewhat later at about 120 Ma (Harangi & Árváné-Sós, 1993).

In the junction area of the Slavonia–Dravia and Kunság Units (region of the Mecsek and Villány Mts), a fault-controlled basin was formed after the Variscan Orogeny, in which up to 3500 m of Late Carboniferous to Late Permian molasse sediments accumulated, with significant rhyolitic volcanism in the Early Permian (Kovács, et al., 2000). The European Variscan Orogenic Belt is genetically controlled by a post-collisional to extensional tectonic regime associated with intense magmatic activity, often having a bimodal (basaltic–dacitic/rhyolitic) character (Szemerédi, et al., 2020).

The Late Palaeozoic volcanic rocks are dominantly altered (K-metasomatized, hydrothermally altered, and low-grade metamorphosed) and significantly vary in petrographic features and geochemical characteristics. Regarding felsic volcanism, the zircon U–Pb ages vary from ~ 300 Ma (Latest Carboniferous) to ~ 245–240 Ma (Latest Permian–Earliest Triassic), suggesting a long-lasting magmatic activity during the Permian–Carboniferous (Ondrejka, et al., 2018).

In the western part of the Tisia Terrane, the only outcrop of these formations is known in the eastern part of the Mecsek Mts at Gyűrűfű and Dinnyeberki area, (Szemerédi, et al., 2016), known by several deep boreholes, associated with the previous uranium ore exploration work, pierced such lithologies (Szemerédi, et al., 2020)..

Permian felsic volcanic rocks in Hungary occur in two mega-units of different geological histories that are the Tisza Mega-Unit and the ALCAPA Mega-Unit (Szemerédi, et al., 2020). Felsic pyroclastic rocks dominantly represent the Tisza MU, while lavas are subordinate and present only within the northern foreland of the Villány Mts (Szemerédi, et al., 2016), (Szemerédi, et al., 2017). Permian volcanic rocks' unsorted, massive appearance originates from pyroclastic flow (ignimbrite) (Szemerédi, et al., 2020).

Permian felsic volcanic rocks showing similar petrographic features appear in Alpine zones. They are collectively named Gyűrűfű Rhyolite Formation in the Hungarian lithostratigraphical literature, after the locality of the single outcrop, near the village of Gyűrűfű in the W-Mecsek Mts (Fülöp, 1994). Most Permian volcanic rocks (Szederkényi, 1962); (Fazekas, 1987); (Barabás Stuhl, 1988) are considered rhyolitic–dacitic lava flows in the drillings and outcrops; however, recently, occurrences in the W-Mecsek Mts were reinterpreted as of pyroclastic origin (Szemerédi, et al., 2016). In this area, the small unique outcrop between the villages of Gyűrűfű and Dinnyeberki is represented by rhyolitic ignimbrites (Szemerédi, et al., 2016), and numerous boreholes penetrated pyroclastic rocks as well. The new U-Pb zircon geochronological data analysis shows that the W-Mecsek Mts at the Gyűrűfű outcrop have the youngest coherent age (267.4 ± 0.6 and -1.4 Ma or ~ 281 Ma) (Szemerédi, et al., 2020).

Trace-elements geochemical data shows that the Permian volcanic rocks of the Tisza MU consist of higher enrichment in all the REEs, excluding the Eu element (Szemerédi, et al., 2020). Moreover, the rocks are characterised by enrichment in Rb, K, Th, and U and depletion in Ba, Nb, Sr, P, and Ti (Szemerédi, et al., 2020). The REE, U, Th, Y, and Zr elements were mobilised by hydrothermal fluids that might have leached these elements from accessory minerals, particularly from fractured and metamict zircon or apatite, monazite, and xenotime (René, 2014). Petrographic observations revealed the scarcity of zircon and other accessory minerals, a possible sign of hydrothermal alteration. Mobility of REE, U, Th, Y, and Zr is most common but not restricted to F-rich hydrothermal solutions related to alkali igneous suites (Rubin, et al., 1993). The formation of uranium ore deposits is often associated with the mobility of these immobile elements (René, 2014). Uranium mineralisation is known in the W-Mecsek Mts, close to the outcrop of the Gyűrűfű Rhyolite (Dinnyeberki uranium ore deposit, (Vincze, et al., 2011); (Konrád, et al., 2012)). On the other hand, hydrothermal sulfidic mineralisation (related to dykes filled with quartz, pyrite, siderite, hydromuscovite, hematite, chalcopyrite etc.; (Fazekas & Vincze, 1991) is presumably formed due to the interaction of the felsic volcanic (host) rock

with hydrothermal fluids. These local ore formations could be feasible sites of accumulation of the immobile elements leached from Permian volcanic rocks (Szemerédi, et al., 2020).

2.1.3 Stratigraphy of W-Mecsek

The Variscan post-orogenic sedimentation began earlier in the Villány area than in the Mecsek one. It produced a Late Carboniferous and Early Permian, molasse-type overstep sequence draped over the crystalline basement's eroded surface (Barabás Stuhl, 1988). It covers the basement between the Villány Hills and Mecsek Mts.

Terrestrial sediments and volcanic rocks had filled up the continental rift troughs of the Tisza Mega unit by the end of the Permian. In the Early Triassic, the marine transgression only reached the innermost zones of the mega-unit. Based on the basis of

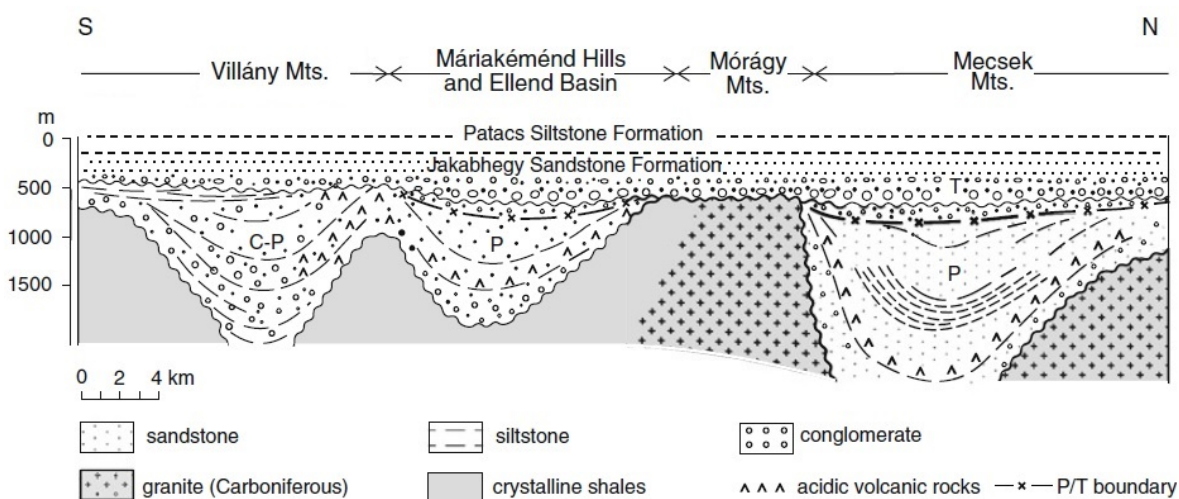


Figure 6 Paleogeographic reconstruction of Late Palaeozoic continental basin in the area of South Transdanubia (After (Haas, et al., 1986)).

sporomorph studies, the Permian/Triassic boundary can be drawn within the upper part of the fluvatile Kővágószőlős Sandstone (Barabás & Barabás-Stuhl, 2005), which represents the final stage of filling of the Late Palaeozoic rift troughs (Figure 6).

The Mecsek area shows varying stratigraphy and strongly varying thickness. Permian formations cropping out in the Mecsek Mts occurring Late Carboniferous–Permian ones only for 30–40 years due to uranium prospecting. The oldest such overstep formation is of the Late Carboniferous age. The next overstep stage is represented by the Early Permian Korpád Sandstone and/or Gyúrúfű Rhyolite, which appear in every unit but

do not cover them entirely. The third stage occurred in the Early Triassic as manifested by the widespread extension of the Jakabhegy Sandstone (Haas, 2012)., described in more detail below.

A 2500–3200 m-thick Permian sequence of the Kunság unit has various types of Late Carboniferous crystalline rock (granite, crystalline schist, serpentinite) that occurs in the entire area of the Mecsek Mts (Szederkényi, et al., 2012). The crystalline rock, mainly locally anchimetamorphic granite, gives the basement underlying the molasses-type sequences of non-metamorphic rocks (Szederkényi, et al., 2012). They occur in the axial zone of the W-Mecsek brachianticline the Permian rocks are at the surface (Barabás, 1979); (Barabás-Stuhl, 1981). (Barabás, 2013) indicated that the Permian succession of the W-Mecsek includes the following formations from old to young (shown in Figure 6).

The Early Permian (P₁) formation:

The Korpád Sandstone Formation consists of 300–320 m-thick, variegated (red, grey and green) but predominantly red, coarse-grained sandstone and conglomerate. As a basal formation, the Korpád Sandstone overlies the granite of the Mórággy Complex, which is 200 km long and 25–30 km wide; it is I-type affinity of Variscan high-K and Mg-rich plutonic rocks in 340–354 Ma old (U/Pb data) located in the western sector of the W-Mecsek containing rich in accessory minerals. Among the others, zircon is very frequent; the euhedral and usually twinned titanite, ilmenite, apatite and rutile also occur. Its upper boundary is an erosional surface covered by the Middle Permian Gyűrűfű Rhyolite Formation, formed ca. 266.8 ± 0.2 Ma (U/Pb data) consisting of a reddish-brown or reddish-purple volcanic body of 50–130 m thickness (Fazekas, 1987). (Balogh & Kovách, 1973) explained that the upper boundary of the formation is a typical erosional surface, and the whole rock Rb/Sr age is 277 ± 45 Ma.

Middle Permian (P₂) formation:

The Gyűrűfű Rhyolite Formation was deposited due to continental rift rhyolite volcanism. It deposited the red coloured continental sediment called Cserdi Conglomerate Formation which is interfingering with Bodai Siltstone Formation.

As a transgressive sequence, the Cserdi Conglomerate Formation is a typical fluvial conglomerate, sandstone of various grain sizes and siltstone of 250-1000 m thickness; it overlies the eroded surface of the Gyűrűfű Rhyolite. It gradually passes upward into the overlying Boda Siltstone Formation.

The Boda Siltstone Formation is not continuous in the entire basin. In the NE direction, it develops from the underlying Cserdi Conglomerate with a 100 m-thick

transitional interval, and a similar transitional zone occurs at the top of the formation. The formation comprises a 900 m-thick, monotonous, reddish-brown siltstone as a record of natron lake formation with a few fine-grained sandstone and dolomite-rich interlayers (Barabás, 2013).

The Late Permian (P₃) formation:

The KSF is the youngest lithostratigraphic unit of the W-Mecsek Permian sequence consisting of uranium ores mainly in its upper part (Barabás & Konrád, 2000). The thickness of the formation varies from 150 to 1400 m from W to E. Four members of the KSF were distinguished, from down upwards: (1) the Bakonya Sandstone Member consists of variegated (red, green and grey) sandstone with disseminated chalcopyrite and galena enrichments; (2) the Kővágóóttős Sandstone Member contains grey arkose sandstone and siltstone with characteristic plant remnants and a greenish uranium ore-bearing level in its uppermost segment; (3) the Cserkút Sandstone Member is composed of red sandstone beds, and (4) finally the Tótvár Sandstone Member consists of a violet gravel-rich sandstone (Barabás & Konrád, 2000).

The Early Triassic (T₁) formation:

The Jakabhegy Sandstone Formation relates to the Early Triassic period, in which the above-mentioned red sandstone covers the Paleozoic sediments (Barabás-Stuhl, 1981). A new sedimentary cycle began with coarse conglomerate and red sandstone deposition in the Early Triassic. These sequences extended over a large area, far beyond the Permian rift troughs, even onto the eroded surface of the Variscan metamorphic complex (Haas, 2012). A coarse conglomerate at the base of the red siliciclastic formation occurs in 1–10 m thickness (Figure 7). The size of the components may attain 20 cm, and quartz, rhyolite, ignimbrite, and granite are the most common rock types encountered. Above the conglomerate unit, the 150–400 m-thick formation comprises cross-bedded sandstone (Haas, 2012).

The Patacs Siltstone Formation occurred in the NE direction during the E Triassic period and is represented by fine-grained shallow marine red siltstone and green claystone (Barabás-Stuhl, 1981). (Figure 7).

2.1.4 Ore mineralisation in the organic-rich sedimentary formation

The W-Mecsek uranium ore occurs in the Late Permian Kővágószőlős Sandstone Formation (KSF) of the Late Permian sediments occurring in the Permian-Triassic anticline of the Mecsek Mountains (René, 2014), see in Figure 8.

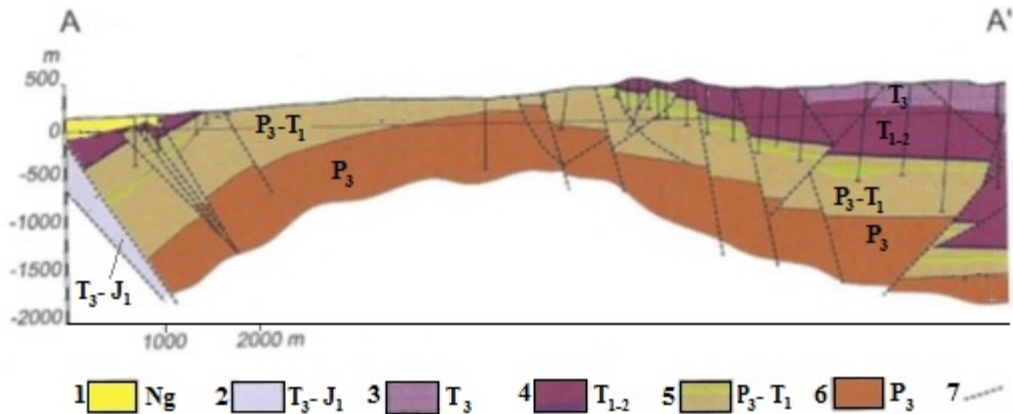


Figure 7 Geological cross-section of the Northern (A) – Southern (A') the direction in the Western-Mecsek Anticline (modified after (Barabás, 2013)). Legend: 1-Neogen; 2-Mecsek coal formation (Late Triassic-Early Jurassic); 3-Misina Formation (Middle Triassic); 4-Patacs Siltstone Formation and Jakabhegy Sandstone Formation (Early-Middle Triassic); 5 Kővágószőlős Sandstone Formation with uranium ore mineralisation (Late Permian-Early Jurassic); 6-Boda Siltstone Formation; 7-Structural zones.

The uranium ore deposit is from the Late Permian age, and KSF represents a fluvial depositional environment, where the thickness of the formation reaches 600 m (René, 2014). The uranium ore lenses and bodies located in the upper zone of the KSF (Virágh & Vincze, 1967), detailed exploration was carried out during the 1950s, yielding detailed data on the characteristics of the unit, which were lastly summarised by (Barabás & Konrád, 2000); (Barabás, 2013). The uranium ores in the KSF are of polygenic origin (Virágh & Vincze, 1967) as they show stratiform pennaccordance, disseminated and transversal enrichments (Barabás, 2013), and a result of prolonged autochthonous mineralisation of the fluid infiltration with occurring three different colours of grey, green and red of the sandstones due to redox potential, such as grey sandstone with terrestrial plant remains relates to the strong reduction, the green is typical for the transitional intermediate of redox zone and red sandstone as a result of the strong oxidation (Vincze, 1987). The uranium concentrations occur in the grey rocks or the green lenses of sandstones between the grey and red zones (Barabás & Konrád, 2000). The thickness of uranium-bearing sandstone varies from 15 to 90 m (René, 2014). Most ore bodies are located in a depth interval between 650 to 800 m depth (IAEA Report, 2014). The recent resource estimate re-evaluation is uranium ore 17 946 t, with an average uranium concentration of 0.117% (IAEA Report, 2014). The occurrence of gold is poorly known in the sequence. Some

sporadic analysis indicated gold might be enriched at a maximum of 6.5 g/t which relates to the reductive carbonaceous matter rich intercalations (Földessy, 1998).

2.2 Geological settings of Bakyrchik

2.2.1 Exploration history of Bakyrchik

Bakyrchik was discovered in 1944. Exploration and mining activities in the province can be traced back to the 1950s by the Soviet geologists through systematic mapping, geophysical and soil geochemical surveys targeting potential gold resources. It only received little attention in the past owing to poor accessibility (Soloviev, et al., 2020). In 1953–1954 was confirmed that it largely occurs in catalysed carbonaceous sedimentary rocks in an extended (~18 km) auriferous tectonic zone (Soloviev, et al., 2020). Mining of higher-grade “oxidised” Au ores commenced in 1955 and by 1997 the Bakyrchik mine had produced ~30 t Au (Maslennikov, et al., 1997). From 1996 to the early 2010s, several drilling campaigns targeting deeper, “reduced” (“double-refractory”) Au ores were undertaken by Western operators (Cox, et al., 2010); (Blakley & Cox, 2004). In 2014, the Bakyrchik deposit was acquired by Polymetal JSC, that in 2020 reported the JORC-compliant reserves of 8.5 Moz Au (average 6.3 g/t Au) and additional resources of 3.5 Moz Au (average 5.4 g/t Au) at 3 g/t Au cut-off for underground and 1.0 g/t cut-off for open-pit mining, in part of the Central Zone of the deposit. The much greater speculative (“prognostic”) endowment has been estimated at 50 to 100 Moz Au by various authors (Maslennikov, et al., 1997); (Rafaylovich, 2009) in the deeper and other parts of the shear zone (Qyzyl). Open-pit mining recommenced in 2018, with the current (2020) rate of 2.0 Mt per annum. The Ore Reserve estimate for Bakyrchik incorporates data from the 29.9 km drilling campaign (168 drill holes) conducted in 2015-2020 (Polymetal, 2022).

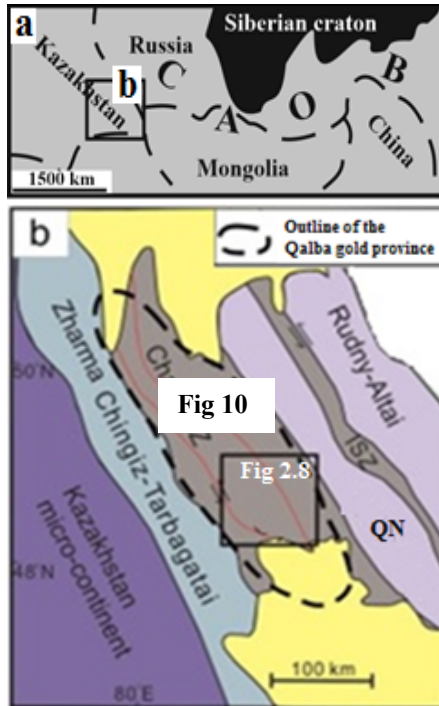


Figure 8 Tectonic framework

of the Central Asian Orogenic Belt and Kazakhstan microcontinent.

ISZ = Irtysh shear zone; QN = Qalba-Narym The outline of NW-SE trending Qalba gold province is also shown. (modified after Glorie et al. (2012);

al., 2009.) reported $^{40}\text{Ar}/^{39}\text{Ar}$ and sensitive high-resolution ion microprobe (SHRIMP) U-Pb ages of the gold deposits in the Qalba province, ranging from 306.6 ± 3.8 Ma to 248.3 ± 3.4 Ma.

The Chara shear zone in CAOB was formed by the collision between the Siberia craton and the Kazakhstan microcontinent due to the closure of the Ob-Zaisan Ocean (part of the Paleo-Asian Ocean) in the late Carboniferous (Windley, et al., 2007). It is several hundred kilometres long, NW-SE trending, and extends from eastern Kazakhstan to the Chinese Altai in Xinjiang, China (Li, et al., 2015). Different terranes bound it due to a series of accretionary events during the late Paleozoic (Buslov, et al., 2004). The Chara shear zone separates the Siberia-derived Qalba-Narym (fore-arc accretionary complex), Rudny Altai and Gorny Altai terranes (island arc systems) and the Kazakhstan-derived active margin of the Zharma-Chingiz-Tarbagatai terrane (Buslov, et al., 2001) (Figure 9 b).

During the last half of the century, many companies from different countries of South Africa, Australia, USA, and UK were working. Still, no positive production technology (Malchenko, 2017) because the bulk (90%) of Au is a structurally bonded or lattice gold and presents as double-refractory gold in the lattice of sulphide ore minerals (Umarbekova & Dyusembaeva, 2019). Moreover, the production of gold affects the environment due to high values of OM and arsenic contents in ores (Polymetal, 2022)

2.2.2 Tectonic and magmatic settings of Bakyrchik

The Bakyrchik Au deposit is included in the Qalba gold province (Kam-Hung, et al., 2017). In eastern Kazakhstan, the Qalba gold province is located in the western part of the Central Asian Orogenic Belt (CAOB) (Figure 9 a & b). The gold deposits are distributed along the Chara shear zone, defining the Qalba gold province (Kam-Hung, et al., 2017). (Naumov, et al., 2012) and (Kovalev, et

The Chara shear zone is marked by three types of ophiolitic *mélange* of different origins (Buslov, et al., 2004): 1) the Cambrian to early Ordovician *mélange* composed of high-pressure metamorphic rocks and gabbro (Buslov, et al., 2003), 2) the Ordovician *mélange* containing blocks of serpentinitised peridotite, gabbro, and amphibolite (Iwata, et al., 1997); (Safonova, et al., 2012), and 3) the Carboniferous to early Permian NW-SE oriented ophiolitic *mélange* representing the lithospheric fragments of the Ob-Zaisan Ocean closed in the late Carboniferous (Iwata, et al., 1997); (Buslov, et al., 2001), (Buslov, et al., 2004). These ophiolite *mélanges* are associated with 5000-m-thick Silurian to Carboniferous sedimentary successions (Safonova, et al., 2012). These successions are fore-arc materials derived from both the Kazakhstan microcontinent and Siberia craton during the evolution of the Ob-Zaisan Ocean (Buslov, et al., 2004). The Silurian strata are composed of alternating limestone, siltstone and chert, whereas the Late Devonian strata are mainly dominated by chert and siltstone with minor amounts of pillow basalts (Iwata, et al., 1997). These sequences are overlain by Carboniferous fore-arc turbidite and intermediate to felsic volcanic rocks that define an active continental margin in the Carboniferous. Intrusions in the Chara shear zone are rarely exposed, and those that do occur are present as small plutons and dyke complexes. They have mostly formed between the late Carboniferous and Triassic (Lyons, et al., 2002); (Vladimirov, et al., 2008). The Chara shear zone is characterised by complex regional scale folding, shearing and faulting with an NW-SE trend. The deformation has created foliations in the rocks and juxtaposed different geological units. Large-scale strike-slip faults were activated during the Permian. The timing of sinistral deformation of the Irtysh shear zone in the Kazakhstan segment, which is situated ~80 km northeast of the study area, is constrained to be ~290 to 265 Ma (Buslov, et al., 2004), (Vladimirov, et al., 2008), although the Irtysh shear zone was reactivated in the Mesozoic (Glorie, et al., 2012). Sinistral strike-slip deformation of the Chara shear zone was most likely coeval with the Irtysh shear zone (Li, et al., 2015). Some workers have suggested that such events are likely related to the collision between the Siberian craton and the Kazakhstan microcontinent and their differential rotations for the major continental blocks (Buslov, et al., 2001); (Buslov, et al., 2003).

(Lubecky, et al., 2008) and (Wong, et al., 2017) have explained that the Bakyrchik gold deposit was formed in an ophiolite Irtysh-Zaisan suture zone relating to post-tectonic plate collisions of the Kazakhstan microcontinent and the Siberian craton in the Late Carboniferous (C₃), which includes the Late Palaeozoic Variscan Orogenic tectono-magmatic event (Parnell, 2019). (Parnell, 2019) considered the deposit one of the most

important gold occurrences related to the global coal depositions of Variscan gold formation during the Late Carboniferous (300 Ma). During the tectono-magmatic event, the collision contributed to the formation of the Kunush granitic batholith in the Late Carboniferous-Early Permian (C₃-P₁) (Rafaylovich, 2009) and the Qyzyl thrust fault (Dyachkov, et al., 2017). The Qyzyl thrust fault (2 km long and 30–50 dip in the north) lies

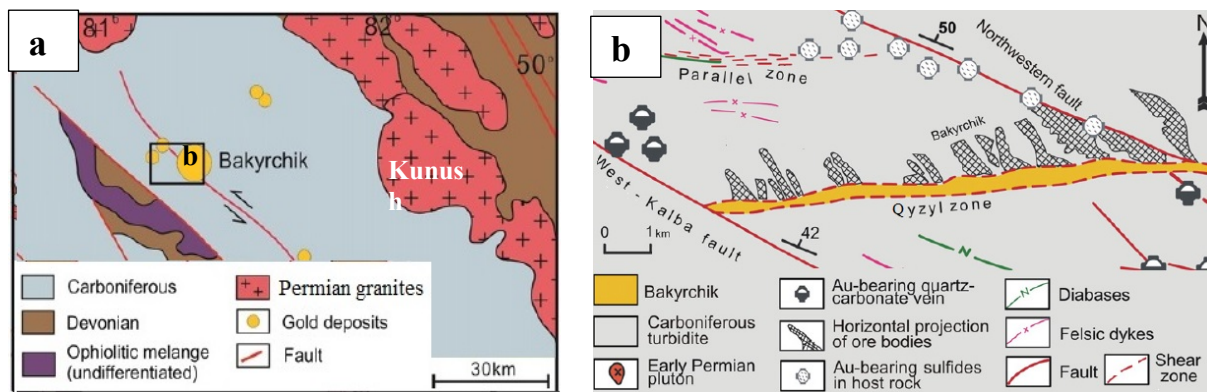


Figure 9 a) Geological map of the Chara shear zone, simplified from (Buslov, et al., 2004), (Daukeev, et al., 2008); b) Geological map of the Bakyrchik ore field. Simplified from (Daukeev, et al., 2004).

within the ore bodies and occurs in carbonaceous-terrigenous rocks of molasses and limnic coal-bearing formations of the Middle-Late Carboniferous (C₂₋₃) Bukon suite in the Middle-Late Carboniferous (C₂₋₃) (Dyachkov, et al., 2011); (Umarbekova, et al., 2017b), as shown in Figure 10 a and b.

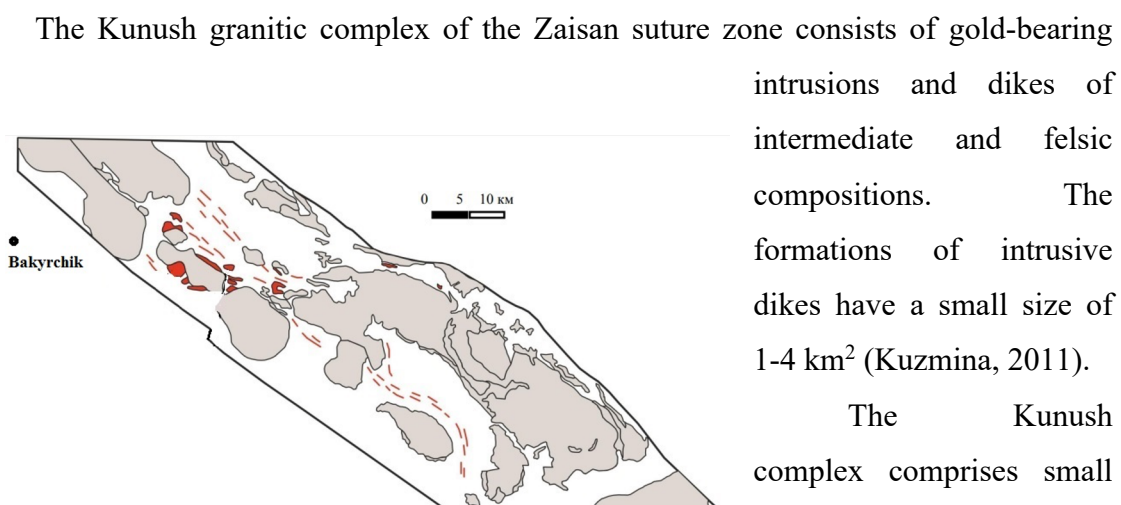


Figure 10 General schematic development of magmatic intrusions of the Kunush complex; (modified after (Kuzmina, 2011).

The Kunush granitic complex of the Zaisan suture zone consists of gold-bearing intrusions and dikes of intermediate and felsic compositions. The formations of intrusive dikes have a small size of 1-4 km² (Kuzmina, 2011).

The Kunush complex comprises small masses of tonalite and granodiorite; and several vein generations of

porphyritic granodiorite, porphyritic tonalite and porphyritic granite (Figure 11). The magmatic intrusions are composed of quartz 25-35%, oligoclase 30-40%, potassic feldspar 15-20% and ore minerals 1-2%. The texture of magmatic intrusions is porphyritic, constantly included its veins quartz of globular forms and prismatic crystals of felsic plagioclase, matrices consisting of microgranitic aggregate (Kuzmina, 2011).

U-Pb isotope data show that the magmatic intrusions of the Kunush complexes range from 306,7+8,7 Ma to 299+2,3 Ma (Kuzmina, 2011).

2.2.3 Stratigraphy of Bakyrchik

Qalba gold province (Fig 12 a) in the Irtysh-Zaisan suture zone of the Kazakhstan microcontinent and the Siberian craton tectonic plate collisions formed in three stages: oceanic (D₃), transitional (D₃-C₁), and continental (C₂-T₁) (Lubecky, et al., 2008).

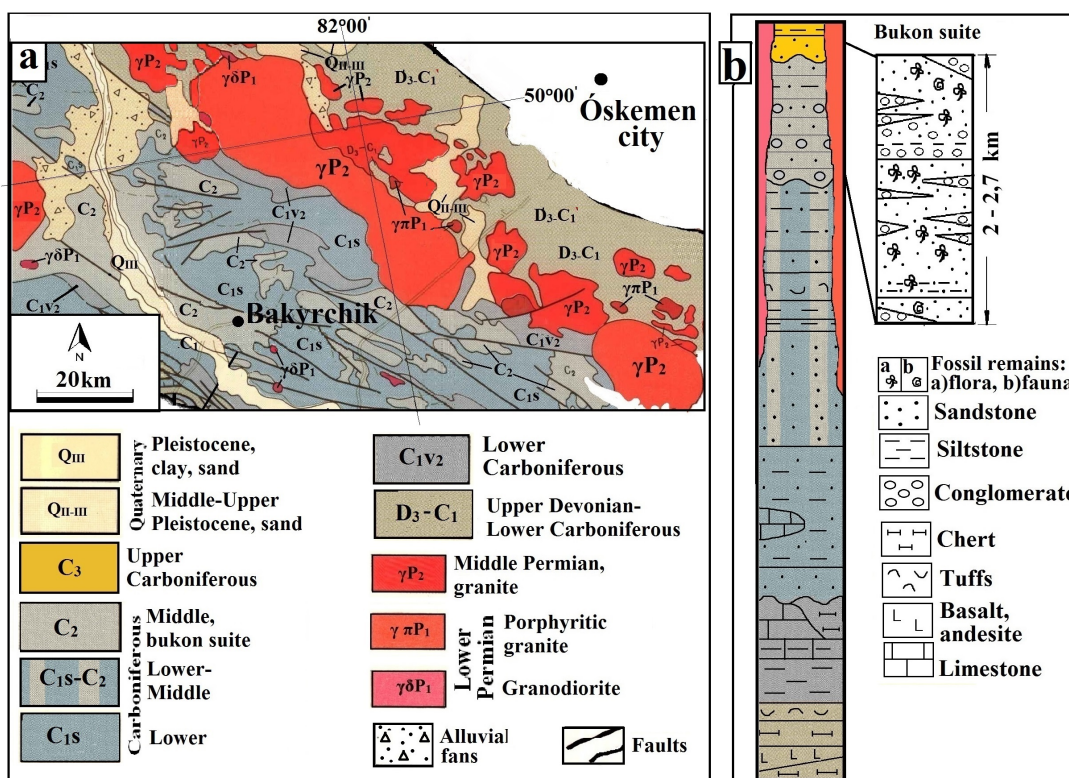


Figure 11 Lithostratigraphic column of Qalba gold province showing lithological facies of Bukon suite of the Bakyrchik deposit (modified from (Trubnikov, 1976); (Umarbekova, et al., 2017b).

The recent structure of the Bakyrchik deposit shows a terrigenous basin, including a Carboniferous sequence from the marine in the Late Devonian - Early Carboniferous (D₃-C₁), coastal-marine in the Middle Carboniferous (C₂), and continental carbonaceous

molasses in the Middle-Late Carboniferous (C_{2-3}) (Lubecky, et al., 2008) see Figure 12 b. The lower part of the stratigraphic sequence comprises a 1500 km thick carbonate and volcanogenic shales and volcanoclastic sandstones containing lenses and interlayers of siliceous sandstone and carbonaceous-cherty siltstones. The upper part of the sequence consists of 600–800 m thick sandstone with layers of carbonaceous siltstones with fossil remains. Carbonaceous-terrigenous sequences are cut through by a magmatic formation (depth 3–3.5 km), which is paragenetically associated with ore mineralisation, and within its single stocks and numerous dikes of tonalite porphyries, and diorite porphyries forming belts of the northwestern and sublatitudinal strike (Rafaylovich, et al., 2011); (Umarbekova, et al., 2017b), see in Figure 12 b.

Late Devonian (D_3) formation:

Early Hercynian island-arc level (D_3-C_1) related to derivatives of andesite-basaltic island volcanism and synchronous argillaceous-siliceous-calcareous and flysch deposits. The ore-bearing rocks are represented by effusive rocks and subvolcanic bodies with basic and intermediate compositions, siliceous siltstones, and limestones. Epigenetic gold mineralisation (pre-ore stage) is spatially related to the volcanogenic siliceous-carbonate-terrigenous formation (C_{1v2-3}) (Kuzmina 2011). (see in Figure 12)

Early Carboniferous (C_1) formation:

Early Hercynian pre-collision level (C_{1s}) comprises sediments of marine low-

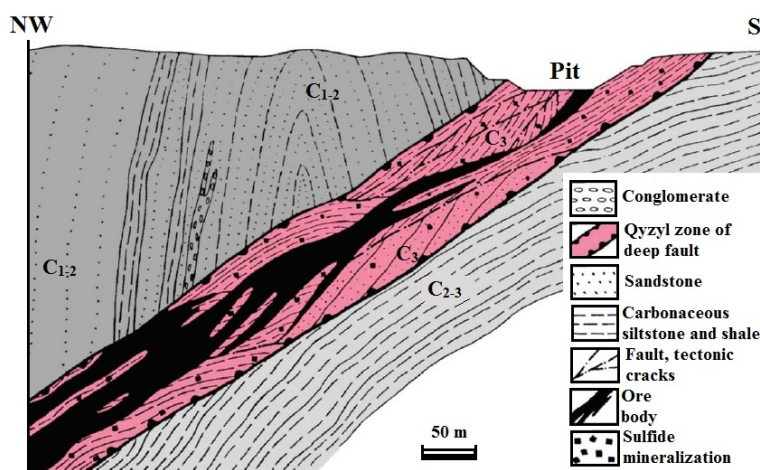


Figure 13 Geological cross-section of the Bakyrchik gold deposit (modified after Dyachkov et al., 2017).

faults of the north-western, sub-latitudinal, and north-eastern directions (Kuzmina 2011).

Middle-Late Carboniferous (C_2-C_3) formation:

carbon graywacke (molassoid). The mineralisation is genetically associated with minor intrusions and dikes of the granodiorite-tonalite formation (C_3-P_1) (Kunush complex). Known vein fields are located in the over-intrusive zones of small massifs of granitoids. Deposits are controlled

Endogenous gold mineralisation reveals a close connection with hypabyssal gabbro-diorite (C₂₋₃) and tonalite-granodiorite (C₃-P₁) formations (Kunush complex) (Kuzmina, 2011).

The middle Hercynian collision level (C₂-C₃) combines molasses limnic carbonaceous (black shale) strata of the Bukon (C₂₋₃) suite. Characterised by terrestrial lithogenesis conditions and drainage of the basin sedimentation. The strata include terrestrial grey-coloured molasses, fluvio-limnic and boggy carbonaceous black shale lithofacies. Gold mineralisation has a dual nature: primary sedimentary and juvenile, associated with small intrusions and dikes of the Kunush complex (C₃-P₁) (Narseev, et al., 2001)

2.2.4 Ore mineralisation in the organic-rich sedimentary formation

The gold reserves of the deposit are 410 t, on average 8–9 g/t (Goldfarb, et al., 2014); (Dyachkov, et al., 2017). Gold mineralisation is enriched in the Qyzyl shear zone and is of a stratiform type (Zhautikov & Maulenov, 1985) formed in the Middle-Late Carboniferous (C₂₋₃) (Dyachkov, et al., 2011). The bulk (90%) of gold in the deposit occurs as an “invisible gold” type, bound to the lattice of arsenian pyrite and arsenopyrite (Umarbekova & Dyusembaeva, 2019) and gold concentrates in a structure of amorphous OM (Marchenko & Komashko, 2011). Gold is enriched with arsenic sulphide minerals in OM (0.2%–0.4%) in host siltstone rocks (Rafaylovich, et al., 2011); (Azerbaev & Zhautikov, 2013). The presence of gold in the carbonaceous matter has a sedimentogenic origin associated with Ag (Azerbaev & Zhautikov, 2013). The total carbon content of the organic carbon and carbonates is 0.3%–26.5% in the host rocks and 2.5%–6% in ore zones (Rafaylovich, et al., 2011). In ore zones, the content of arsenopyrite ranges from 0.3% to 15% while arsenian pyrite varies between 1.5% and 22% (Rafaylovich, et al., 2011). I. The gold content in OM can reach 10%–30% (Marchenko, 2010), while the gold content in arsenopyrite can reach more than 150 and 60 ppm in arsenian pyrite (Levitan, 2008), respectively. Platinum group metals (PGE) are also common in arsenian pyrite and arsenopyrite-bearing ores, up to 1 ppm (Rafaylovich, et al., 2011), and in nanostructured particles of organic materials in the deposit (Marchenko & Komashko, 2011). The content of OM in the Bakyrchik gold deposit is around 24 million tons (Mizernaya, 2001).

3. Samples and Methods

3.1 Sample collection and sample preparation

3.1.1 Sampling procedures of W-Mecsek

This part of the study was carried out on drill core samples of the borehole WHEI/2 ($46^{\circ} 6' 8.856''$ N - $18^{\circ} 10' 49.188''$ E) located 15 km west of Pécs city. Samples from the mining area of the closed uranium mine of W-Mecsek (no shown, Figure 14 a) were from a depth of between 33.79 m to 950 m. The samples were collected during the exploration campaign conducted by Rotaqua Kft, organised by János Földessy and sampling was performed by Szabolcs Tóth and Attila Kasó from 2016 to 2017.

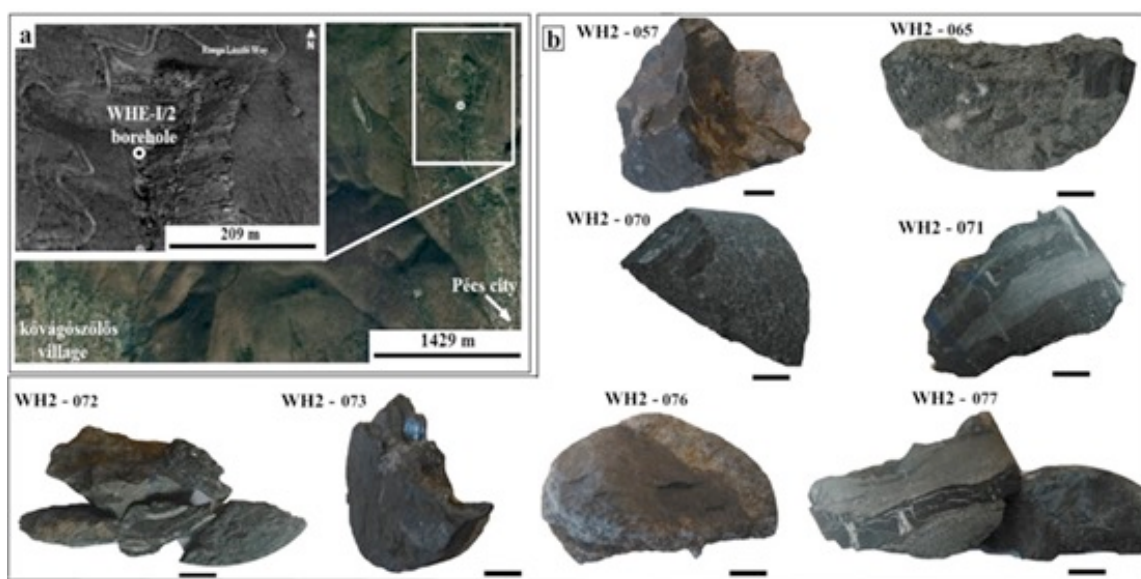


Figure 14 Overview map of a closed uranium mining area in W-Mecsek showing the drill well WHE-I/2 (a) and collected hand specimens of the drill core samples (b).

Scale for rock fragments – 1 cm.

Eight samples were selected for the drill core samples from 832 m to 907 m (total studied samples 75 m) regarding the KFS. Other samples of Cserkút Sandstone from 34 m to 815 m related mainly to red and green sandstones, whereas the selected grey sandstones of the Kővágóöttös Sandstone solely occurred from 815 to 950 m. The data belongs to the red and green sandstones found with minor uranium (up to 96 ppm) and low-grade of precious metals (Au 1 ppb – 24 ppb, Ag 1 ppb – 2 ppm) of the Rotaqua company.

The main three reasons for the selection of the samples (all grey sandstones) having grey colour are; (1) they occurred in a strong reduction zone, (2) they were of the comparatively higher amount in the carbonaceous matter (average 12 wt%), and, (3) gold occurs more in the reductive carbonaceous matter of the grey sandstones (Földessy, 1998).

The sample label was shortened from the same borehole's name as WHE-I/2 to WH2 (see Figure 15 a) and shown in the samples in Figure 15 b, lithology and collection depth in Table 1. The rock samples are related to mixed siliciclastic-carbonate rocks.

Table 1 Total samples collection of W-Mecsek.

№	Samples	Depth (m)	Mass (g)	Density (g/cm ³)	Lithology and texture
1	WH2-057	831.4	189.90	2.7	fine grained dolomitic silty sandstone with carbonaceous shale layers
2	WH2-065	847.6	81.90	2.6	medium-grained silty sandstone with dolomite and carbonaceous shale lenses
3	WH2-070	865.9	36.20	2.8	medium-grained dolomitic silty sandstone with carbonaceous shale lenses and sulphide inclusions
4	WH2-071	870.0	27.40	2.6	carbonate-rich silty sandstone with carbonaceous shale lenses
5	WH2-072	870.5	40.54	3.2	fine grained dolomitic silty sandstone with thin carbonaceous shale lenses and presence of disseminated sulphide
6	WH2-073	883.3	65.27	2.7	coarse-grained carbonate-rich sandstone intercalation with fine-grained carbonaceous silty clay layers
7	WH2-076	895.6	102.11	2.6	coarse-grained dolomitic silty sandstone with carbonaceous shale lenses
8	WH2-077	907.5	78.22	2.7	medium-grained carbonate-rich silty sandstone with inclusions carbonaceous shale lenses

Note: it is shown whole-rock density.

3.1.2 Sampling procedures of Bakyrchik

The samples were collected from the sulphide-ore-bearing carbonaceous-sedimentary formation in the Bakyrchik gold deposit near to Auezov village, East Kazakhstan (Figure 15 a).

Nine rock samples have been selected from organic-rich sedimentary bedrocks in three mineralisation zones near the open-pit's shear zone (see in Figure 16 a) for analytical and experimental observations. The first three samples related to the lower zone of pre-ore mineralisation (carbonaceous-sulphide ore formation), the second three ones represent the main ore mineralisation zone (arsenic-rich sulphide ore formation), and the last three samples of the third group (antimony-rich ore formation) were collected from the upper surface zone of post-ore mineralisation.

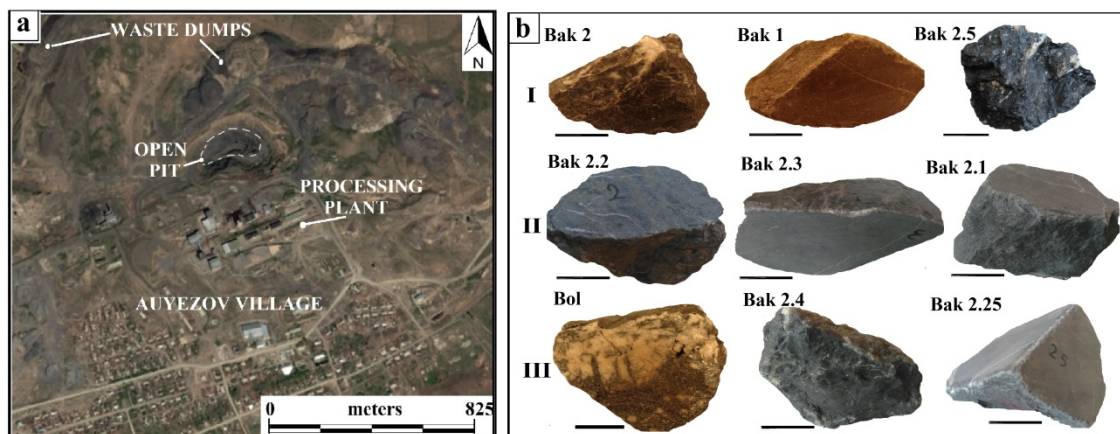


Figure 15. An overview map of the study area (a) showing the sampling area marked with broken lines and fragments of nine samples (b) from separated three groups.

The first three samples (Bak 2; Bak 1; Bak 2.5) of the first (I) group are carbonaceous-siltstone rocks;

The next three samples of the second (II) group (Bak 2.1; Bak 2.2; Bak 2.3) are arsenic sulphide-rich carbonaceous-siltstones; and

The last three samples (Bol; Bak 2.4; Bak 2.25) of third (III) group are antimony sulphide-rich carbonaceous-siltstone rocks (Figure 15 b).

The sample's density ranges from 2.8 g/cm³ to 5.6 g/cm³. Handly separated solid bitumen density is an average of 2 g/cm³ and its hardness ranges from 2.5 to 3 (in Mohs scale), see Table 2.

Table 2 Total samples collection of Bakyrchik.

№	Mineralisation groups	Samples	Mass (g)	Density (g/cm ³)	Lithology and texture
1	I - carbonaceous-sedimentary pre-ore mineralisation	Bak 1	123,24	2.5	fine-grained siltstone rocks with dark grey organic matter inclusions
2		Bak 2	190,40	2.6	black organic-rich fine-grained siltstone rocks
3		Bak 2.5	760	2.9	black carbonaceous-siltstone rocks with fine grained quartz inclusions
4	II - arsenic sulphide ore mineralisation	Bak 2.1	600	2.7	organic-rich fine-grained siltstones with arsenic sulphide-quartz veinlets
5		Bak 2.2	1840	3.2	arsenic sulphide-rich carbonaceous-siltstones with fine grained quartz
6		Bak 2.3	1910	3.3	arsenic sulphide-rich carbonaceous-siltstones
7	III - antimony sulphide ore	Bol	765	2.9	antimony sulphide-rich carbonaceous-siltstone rocks with fine grained quartz grains

8	mineralisation	Bak 2.4	920	2.9	carbonaceous-siltstone rocks with antimony sulphide-quartz veinlets
9		Bak 2.25	794	2.8	antimony sulphide-rich fine grained siltstone rocks with minor organic matter inclusions

Note: it is shown whole-rock density.

3.2 Sample preparation of W-Mecsek and Bakyrchik

Generally, 17 rock samples (eight samples of W-Mecsek and nine samples of Bakyrchik) have been chosen from the two mineral deposits of W-Mecsek and Bakyrchik, respectively. They are organic-rich sedimentary rocks associated with sulphide minerals (Figure 16). All rock samples have been prepared in three ways as powder specimens with a size below 70 μm , polished sections of the whole rock and thin sections for further analytical measurements (see in Table 3).



Figure 16 Total samples collected from both mineral deposits:

A-Mecsek and B-Bakyrchik.

Powder samples of size 10~63 μm (shown in Figure 17 a and b) were crushed in a tungsten carbide ring mill and then an agate mortar, homogenised and portioned for further measurements. General 17 powder samples for Wavelength Dispersive X-ray fluorescence (WD-XRF), 17 powder samples for X-ray powder diffraction (XRPD), and Soxhlet extraction were done; two ones on each sample (WH2-073, WH2-077; Bak 2.2 and Bak 2.5). Six carbonate-free powders were used for the Fourier-transform infrared spectroscopy (FTIR) with an attenuated total reflectance (ATR) attachment and seven powders for organic elemental analysis (OEA) after removing inorganic carbonate minerals within 10% hydrochloric acid. Bulk and sequentially separated sample's gold concentration was determined by inductively coupled plasma-optical emission spectroscopy (ICP-OES) from

12 powder samples, analytical technique parameters and experiments are described in detail in the subchapters of 4.3 and 4.4.

The polished sections (shown in Figure 17 c) in the study have a total of 43 specimens (16 samples of W-Mecsek and 27 samples of Bakyrchik) and 8 thin sections of each deposits (~30 μm thick) for inorganic and organic petrography, ore microscopy, electron microscopy, micro-Raman spectroscopy and laser ablation inductively coupled plasma mass spectrometry (LA-ICP-MS).

All the petrology mentioned above, analytical instruments and laboratory works were carried out at the University of Miskolc, except the Raman measurement which was carried out at the University of Szeged; the vitrinite reflectance measurement at the company of MOL in Budapest; and LA-ICP-MS measurement was performed in the Mining and Geological Survey of Hungary in Budapest.

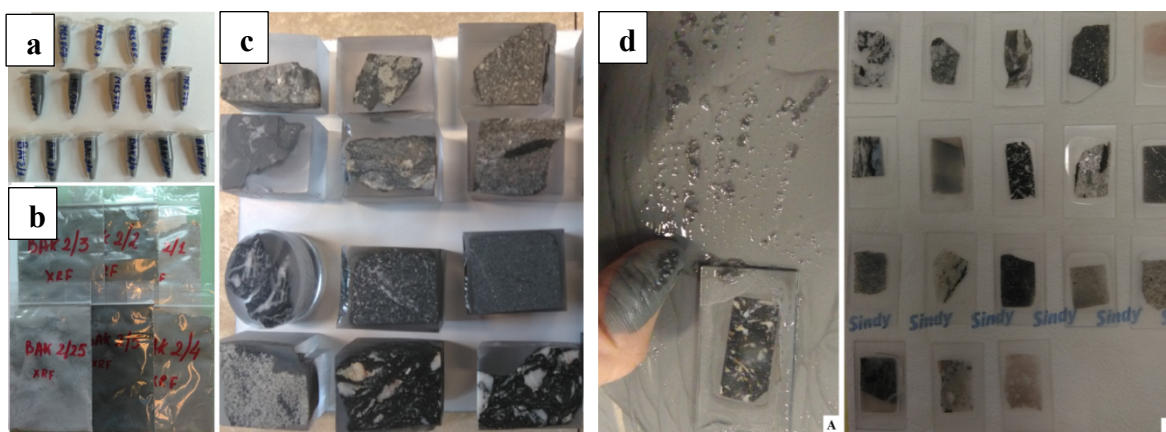


Figure 17 General review of samples preparations of W-Mecsek and Bakyrchik mineral deposits: a) powder samples for XRD; b) powder samples for WD-XRF; c) polished sections (upper is W-Mecsek and lower is Bakyrchik), and d) thin sections.

3.3 Analytical methods for ore minerals

3.3.1 Optical microscopy and electron microscopy

Zeiss AxioImager (A2m) microscope for imaging in incident normal light; and a photography camera (AxioCam MRc5) were used to observe the sulphide ore minerals with the computer program AxioVision Rel. 4.8 by Carl Zeiss MicroImaging (GmbH) for transmitted and reflected light modes. The objectives are to describe the morphology and the nature of the different types of sulphide and uranium ore minerals.

The electron probe microanalysis (EMPA) with backscattered electron (BSE), energy dispersive spectroscopy (EDS) and X-ray mapping was carried out on a JEOL SXA 8600 Superprobe (20 KeV and 20 mA) for elemental analysis for major sulphide ore minerals (arsenopyrite, arsenian pyrite, stibnite and valentinite) and minor ore minerals of uranium and very tiny grains of framboidal pyrite, galena and sphalerite. Moreover, the technique was used to evaluate elemental concentrations in grains of OM, including contents of sulphur, chlorine, phosphorous and others.

3.3.2 XRPD and WD-XRF

Mineral inclusions of samples were determined by XRPD (BRUKER D8 ADVANCE Cu-K α 40 kV, 40 mA). Wavelength Dispersive X-ray Fluorescence (WD-XRF, RIGAKU Supermini Pd source, 50 kV-4 mA) measured selected elemental compositions of minerals.

3.3.3 LA-ICP-MS and ICP-OES

Many authors have indicated that gold-bearing OM and sulphide minerals can not be determined directly with optical or electron microscopy but requires more sophisticated techniques, such as laser ablation inductively coupled plasma mass spectrometry (LA-ICP-MS) (Henderson, et al., 2019) and digestion methods (Varshal, et al., 2000); (Dold & Fontboté, 2001); (Henrique-Pinto, et al., 2015); (Usmanova, et al., 2017), because gold occurs in the structure of solid matrices, or as discrete inclusions smaller than 1000Å (100 nm) (Cook & Chryssoulis, 1990); LA-ICP-MS allows the detection of low levels of trace element enrichment (Butler, et al., 2007); (Wagner, et al., 2007); (Deol, et al., 2012); (Diehl, et al., 2012); (Zheng, et al., 2013); (Steadman, et al., 2021).

In this case, we have selected two ways with using techniques for measuring precious metals in OM (additionally, sulphide ore minerals) such as LA-ICP-MS, using spot analyses on grains of OM, and additionally for sulphide minerals as well; and ICP-OES, using liquid extracts after digestion process of the experiment. Moreover, LA-ICP-MS provides similar sensitivity, precision and accuracy data compared with total digestion ICP-OES data; for analysing gold in OM (pyrobitumen) (Henderson, et al., 2019) and for sulphide minerals as well (Wagner, et al., 2007); (Diehl, et al., 2012), (Kexin, et al., 2021).

The U contents are not reportable for the data of LA-ICP-MS and ICP-OES due to elevated backgrounds; moreover, frequently, a close association between U and OM in the

W-Mecsek uranium ore deposit due to previous authors (Szalay, 1954); (Szalay & Almassy, 1956); (Benkő & Szadeczky-Kardoss, 1957); (Szalay, 1969); (Ódor, 1969)(Ódor, 1969); (Varga, et al., 1972); (Kádas, 1983). LA-ICP-MS and ICP-OES have been solely concentrated to measure the concentrations of precious metals (Au, Ag, Pt and Pd) in OM for both ore deposits.

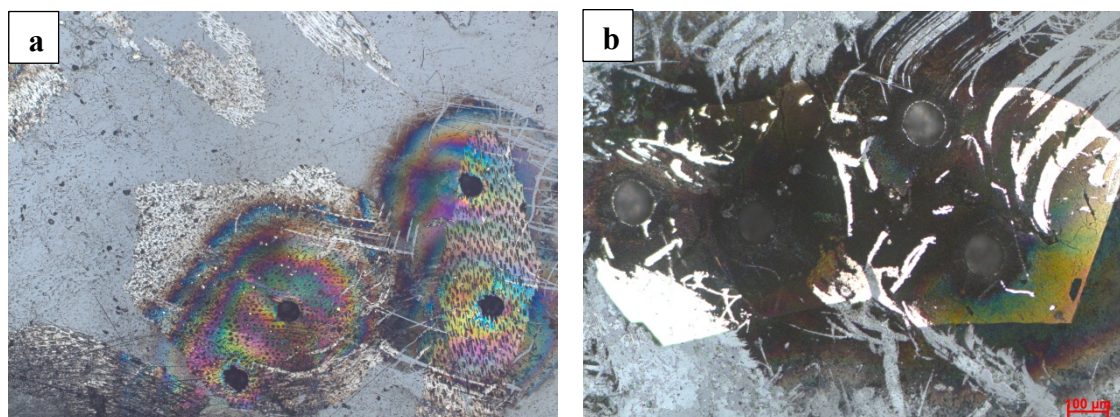


Figure 18 LA-ICP-MS measurement on particles of OM (a) and arsenic-bearing sulphide minerals (b).

LA-ICP-MS, the analytical instrumentation used of a New Wave UP213ss Laser Ablation System with Perkin Elmer Sciex Elan DRC II ICP-MS. Analyses were performed with laser beam diameters of 55–100 μm and at 2–5 Hz repetition rates. The laser beam energy was maintained at about 8 J/cm². The analysis time for each sample was 100 s, which includes 40 s of background measurement with the laser switched off and 60 s of analysis with the laser on. The acquisition time for all masses was set to 0.01 s, with a total sweep time of around 0.6 s. The ICP-MS instrument employed the following parameters: Auxiliary gas flow 1.2 L / min⁻¹; Plasma gas flow 15 L / min⁻¹; Carrier gas flow (He) 0.9 L / min⁻¹; Sampling gas flow (Ar) 0.99 L / min⁻¹ and RF (radio frequency) power 1250 W.

Seven samples of both mineral deposits (WH2-065; WH2-072; WH2-073; WH2-076; Bak 2, Bak 2.4 and Bak 2.5) have been measured by LA-ICP-MS spot analyses focusing on OM particles and a few grains of arsenic-bearing sulphide minerals (Figure 18 a and b). A total of 160 spots were measured for both mineral deposits, 130 spots in grains of the OM and 30 spots in crystal grains of the ore sulphide minerals.

The 110 spots analyses of LA-ICP-MS are related to W-Mecsek samples (50 spots for all bitumen types, 45 spots for vitrinite, ten spots for pyrites) and five spot lines (3 for

OM and 2 for pyrite grains). In detail, 40 spots in WH2-065; 13 spots in WH2-073; 22 spots in WH2-076; 20 spots in WH2-076 and ten spots in WH2-072.

The samples of Bakyrchik were measured by a total of 50 spots analyses of LA-ICP-MS, 32 spots were on particles of OM (17 spots for Bak 2; 5 spots for Bak 2.4; and ten spots for Bak 2.5) and an 18-point analysis was measured on arsenic-sulphide minerals grains (6 spots for Bak 2; 5 spots for Bak 2.4; and seven spots for Bak 2.5).

ICP-OES (720 ES made by VARIAN Inc., Arial Plasma-view, and simultaneous multi-element ICP spectrometer) was used to determine gold concentrations in bulk and sequentially separated samples after the acid digestion of the experiment (more detailed in the next section).

3.4 Analytical methods for OM

3.4.1 Organic Petrology

Reflected-light organic petrography and ore mineralogy were performed on a Zeiss UMSP 50 microscope controlled through a Core i2 Personal Computer. Vitrinite reflectance measurements were made on Axioplan Zeiss microscope extended with J&M spectrometer system of the MOL Ltd. For organic petrology 50x oil immersion objective was used (R.I. of the oil = 1.5180). A Zeiss AxioImager (A2m) microscope was used for imaging in incident normal and fluorescence light. A photography camera (AxioCam MRc5) was used with the computer program AxioVision Rel. 4.8 by Carl Ziess MicroImaging (GmbH). Vitrinite reflectance measurements were carried out according to ASTM D7708-11 (ASTM, 2014) standard for dirpered organic matter thermal matutity determination and performed under monochromatic light of 546 nm, following the procedures outlined by (Taylor, et al., 1998).

3.4.2 Infrared analysis

Fourier-transform infrared spectroscopy (FTIR, Model JASCO- 4200 type A) with an attenuated total reflectance (ATR) attachment was used for determining the molecular structure and composition of OM; selected three samples of WH2-057, WH2-073,WH2-077; and Bak 1, Bak 2.2 and Bak 2.5 for the analysis.

3.4.3 Raman analysis

Raman microscopy (Thermo Scientific DXR Raman Microscope 532 nm Nd-YAG solid-state laser and software OMNIC for Dispersive Raman 8.3.104) was used for thermal maturity and estimated alteration temperature of the OM, acquiring 40 measurement points focused on the petrographically different types of organic materials of the whole rock (WH2-057, WH2-065, WH2-072, WH2-073; and Bak 1, Bak 2, Bak 2.4, Bak 2.5) and each one demineralised concentrated kerogen samples (WH2-073 and Bak 2.5) which were mounted in epoxy resin and polished before. The Raman measurements were collected in an orderly organic phase acquiring 5 - 10 spectra for each sample. The laser beam was focused to a width of about 0.9 μm with a 100X objective changing to 10X and 50 X due to the sizes of organic materials. The numeric aperture (NA) of the objective was 0.90. The beam was aimed perpendicular to the polished section. The peak measurements were collected in the 500 – 3500 cm^{-1} range in the first and second-order regions.

3.4.4 Organic elemental analyser

The organic elemental analyser (OEA, ELTRA's CS-2000) was used for the organic elemental measurement of sulphur, nitrogen and hydrogen in samples. The measurement of organic elements was carried out on seven samples of both minerals deposits. The three samples (WH2-057, WH2-073 and WH2-077) were from W-Mecsek and four (Bak 2; Bak 2.2; Bak 2.4 and Bak 2.5) of Bakyrchik.

3.4.5 Total organic content (TOC)

Total organic carbon (TOC %) content in general seven samples (WH2-057, WH2-073 and WH2-077; Bak 2; Bak 2.2; Bak 2.4 and Bak 2.5) of both mineral deposits was analysed twice each carbonate-free sample (5 g) by the organic elemental analyser (OEA, ELTRA's CS-2000) after 10 % hydrochloric acid treatment (45 ml) under room temperature and 60°C for 20-30 minutes into a water bath.

3.4.6 Bitumen and kerogen extraction

The bitumen extraction analysis (Figure 19 a) was carried out with 100 g of powdered samples of both deposits and extracted into a cellulose thimble of Soxhlet apparatus (Büchi B-811) with a mixture of dichloromethane (837 ml) and methanol (63 ml) at 46°C for three days. Due to the low contents of organic carbon, the extracts were not further separated into fractions of saturated and aromatic hydrocarbons.

The kerogen sample was obtained after removing of carbonates using 10% HCl (for 2 hours, at 60°C in a water bath). Silicates and quartz minerals using 40% HF; 10% HCL (3:1, for 5 hours, at 70°C) into a platinum dish (shown in Figure 19 b) and then the kerogen is separated physically from sulphide minerals by sodium polytungstate (SPT) heavy liquid, described more details below.

Kerogen purification was carried out by the sink-float separation (or heavy liquid separation) method using sodium polytungstate (SPT). The chemical reagent is non-toxic and environmentally friendly. The method with SPT was successful in separating different densities. Kerogen has a density of less than 1.02 g/cm³, pyrite up to 5 g/cm³ and SPT was made with density a 2.0 g/cm³(Figure 19 b). The three different densities were divided into three positions; the upper layer is kerogen, middle SPT and pyrite remains in the bottom (Figure 19 c).

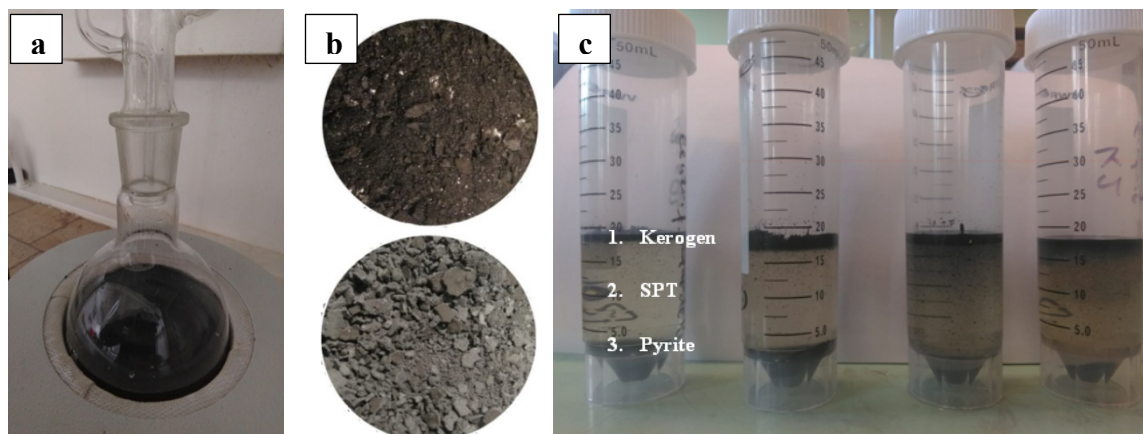


Figure 19 General review of extractions for organic fractions: (a) bitumen extraction; (b) kerogen chemical demineralisation (upper WH2-073 and lower Bak 2.5); c) kerogen physical purification (separations of 1-kerogen, 2-SPT, and 3-pyrite).

3.5 Experimental methods for samples in W-Mecsek and Bakyrchik

A three-stage sequential extraction method has been chosen in the experiment to remove gold and silver from soluble fractions (see in Figure 20 a) in three selected samples (WH2-57; WH2-73, and WH2-77) for the W-Mecsek and nine samples for the Baryrchik. Many authors have practised the experiment (Varshal et al., 1995; Lakatos et al., 1997; Baruah et al., 1998) to extract and evaluate precious metals in organic fractions and sulphide minerals.

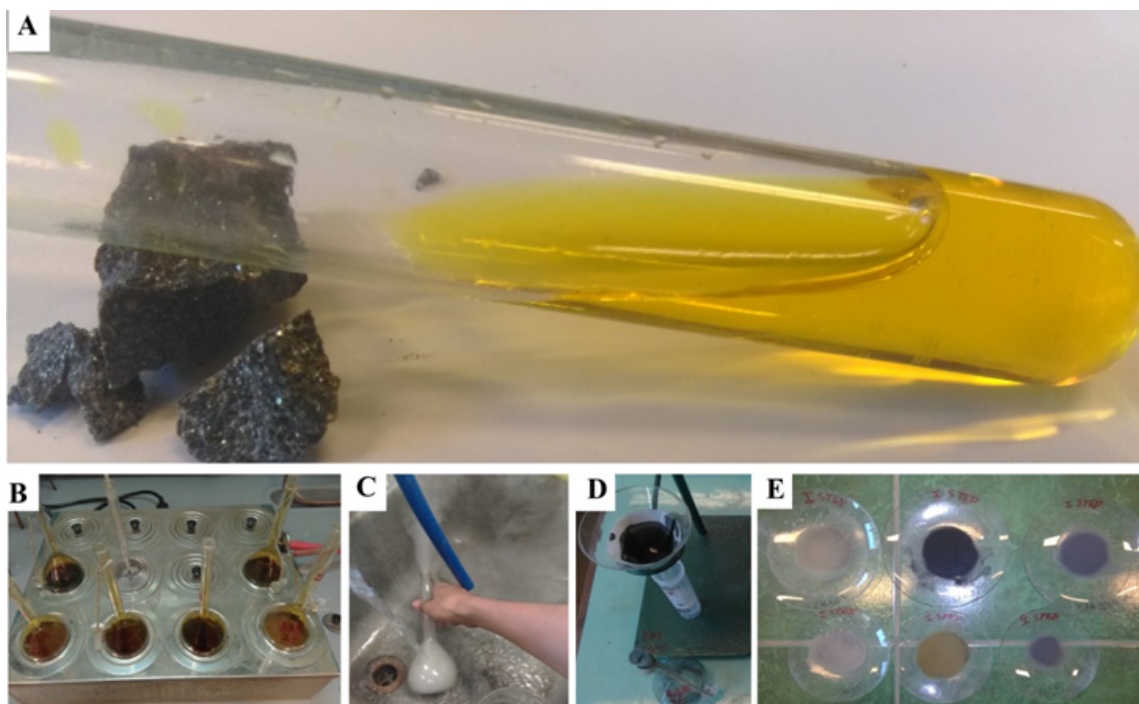


Figure 20 The review of one of the experiments. Sequential extraction method:
 A-soluble extract with Au and other trace metals; B-water bath at 100°C;
 C-extremely high-reaction between H₂O₂ and sulphide minerals;
 D-filtration process; E-preparation for the drying process.

3.5.1 An experiment of samples in W-Mecsek

The experiment was performed by a three-stage sequential extraction method: potassium hydroxide for humic acid (I stage), hydrochloric acid for carbonates, sulphide, sulfate and iron oxide (II stage) and aqua regia (III stage) for iron sulphide, based on (Lakatos, et al., 1997); (Varshal, et al., 2000); and (Henrique-Pinto, et al., 2015). All authors have used sodium hydroxide for OM dissolution. Still, it was preferred to select potassium hydroxide in our experiment because the reagent can be more reactive on samples of high sulphur coal (Mukherjee & Borthakur, 2003), which corresponds with our case.

Experimental materials were gathered such as a test tube rack (woody), funnel and 11 cm diameter of filter paper (Filtrier-Papier Nr. 5893 Blauband Marke Selecta-Germany) for filtration procedures and an oven for drying fractions after filtration on each stage. The chemical reagents of potassium hydroxide (1M KOH) hydrochloric acid (37% HCl), and aqua regia (68% HNO₃ + 37% HCl) are provided at the Chemical Department of Miskolc

University. Eight rock samples contain different amounts of organic phase together with minerals. The samples were crushed separately to less than 63 μm , using an agate mortar and pestle, and reducing the sample size of powders using coning and quartering. After the crushing process, the powder sample compounds of mostly OM and pyrites were weighed at a maximum of 5 g from the selected three samples for the experiment.

In the first stage (I) for organic materials dissolution, 5 g powders were weighted and then mixed manually with 45 ml of 1M KOH added into a glass beaker (100 ml). After the mixing process the glass test tube was placed in a water bath at 70°C water for 2 hours (Figure 20b and c). After this procedure, it was placed in an ultrasonic bath for 15 minutes and then centrifuged at 2500 rpm for 10 minutes. Finally, it was decanted and filtrated for liquid extracts and solid residues (Figure 20 d). The residue materials remained for the second stage.

The second stage (II) is related to dissolving iron oxide, sulfate, sulphide and carbonates from the residual samples from the first stage. The 2.5 g powder samples were added and mixed manually within 22.5 ml of 37% HCl, heating at 60°C for 1 hour in a water bath. The extract was decanted and collected into a plastic test tube. Then the residue was prepared for the next stage by washing with distilled water and left them in the oven for drying (Figure 20 e).

In the third stage (III), sulphide minerals, mostly sulfosalt minerals and arsenian pyrite, the residue materials from the second stage were weighed for 2 g powder samples and it was mixed with 18 ml aqua regia (68% HNO₃ + 37% HCl, 1:3). Then, it was placed in a water bath at 80°C water for 30 minutes. After finishing, the liquid extract was filtered as the former process. ICP-OES measured the liquid extracts of three stages for concentrations of gold, silver, and platinum group metals (Pt and Pd) as well.

3.5.2 An experiment of samples in Bakyrchik

A three-stage sequential extraction method has been chosen in the experiment to remove gold from soluble fractions in nine samples. Many authors have practised the experiment (Beckett, 1989); (Davidson , et al., 1999); (Liang & Jian-Ming, 2016) to extract and evaluate heavy metals of sulphide and organic fractions.

The experiment was performed using a three-stage sequential extraction method based on (Dold & Fontboté, 2001); (Usmanova, et al., 2017). Experimental materials were gathered such as a test tube rack (woody), funnel and 11 cm diameter of filter paper

(Filtrier-Papier Nr. 5893 Blauband Marke Selecta-Germany) for filtration procedures and an oven for drying fractions after filtration on each stage. And the chemical reagents of hydroxyl ammonium chloride ($\text{NH}_2\text{-OH}\cdot\text{HCl}$), hydrogen peroxide (H_2O_2) and aqua regia (HNO_3+HCl) are provided by the Chemical Department of Miskolc University. Nine samples contain the most OM and arsenic sulphide-rich minerals. The samples were crushed separately to less than $63\ \mu\text{m}$, using an agate mortar and pestle, reducing the sample size of powders using coning and quartering. After the crushing process, the powder sample compounds of mostly OM and arsenic sulphide minerals were weighed at a maximum of 5 g from every nine samples for the experiment.

In the first stage is related to dissolving iron oxide and sulphides; the 5 g powder samples were added and mixed manually within 45 ml of 1M $\text{NH}_2\text{OH}\cdot\text{HCl}$ (hydroxylammonium chloride) at pH 4.5. Then the tube was shaken for 2 hours at room temperature. The extract was decanted and collected into a plastic test tube. Then the residue was prepared for the next stage by washing with distilled water and left in the oven for drying at 60°C .

In the second stage (for organic materials dissolution), 2 g powders from the residue of the sample from stage I were weighted and then mixed manually with 18 ml of 30-35% H_2O_2 (hydrogen peroxide) added into a glass beaker (100 ml). After the mixing process, the glass test tube was placed in a water bath at 85°C water for 1 hour. After this procedure, the sample was decanted and filtrated for liquid extracts and solid residues. The residue materials remained for the second stage. This procedure was repeated on other samples nine times, in general, to extract gold from the OM.

In the third stage (for sulphide minerals, mostly arsenopyrite), the residue materials from the first stage were weighed for 1 g powder samples and mixed with 9 ml aqua regia (68% HNO_3 – 37% HCl , 1:3). Then, it was placed in a water bath at 100°C water for 1 hour. After finishing, the liquid extract was filtered as the former process, repeated nine times on other powder samples from arsenic sulphide minerals for gold extraction. ICP-OES also measured the liquid extracts of the three stages for gold concentrations and other noble metals, and XRPD examined the residues of extracts.

4. Microscopic petrography of W-Mecsek and Bakyrchik samples

4.1 Microscopic petrography of W-Mecsek samples

The eight sandstone samples of the drilled cores have a typical occurrence of uranium-bearing carbonaceous detritus within a sandstone matrix containing sulphide (pyrite) and OM (Figure 21 a), composed mainly of quartz, muscovite, feldspar, carbonate and clay.

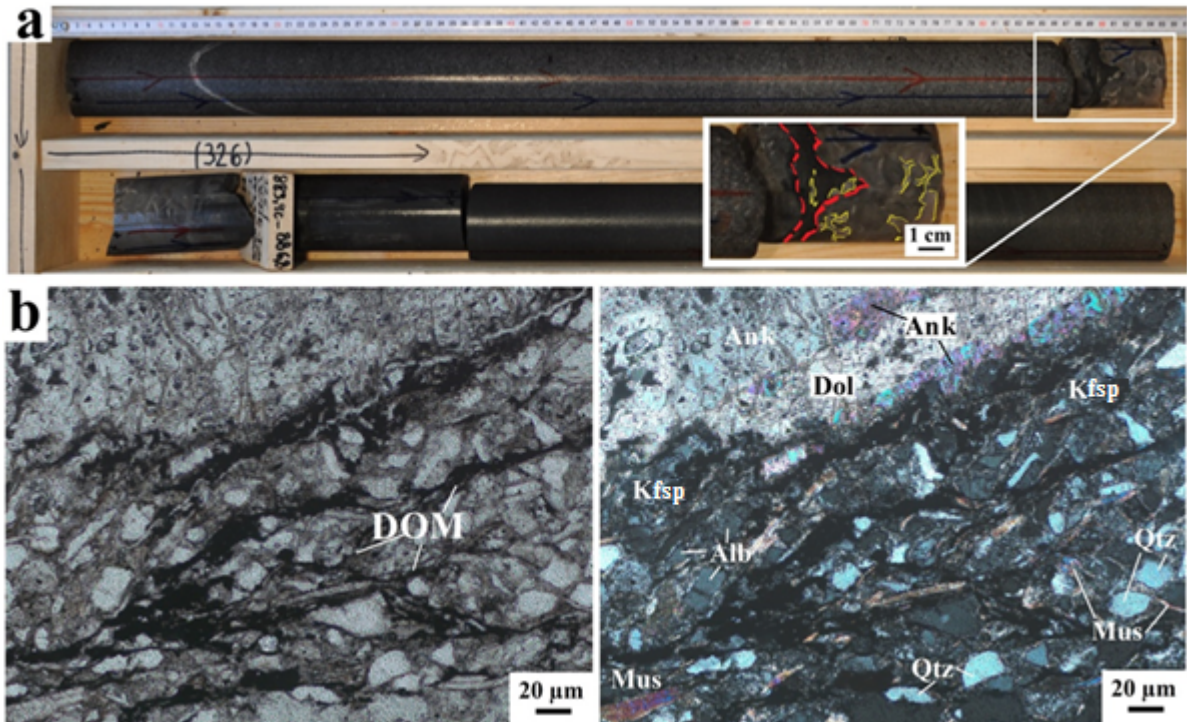


Figure 19 General overview of (a) drill core samples (between 883-886 m), denoted zones of carbonisation (red colour) and pyritisation (yellow colour); and (b) transmitted-light micrograph (left-PPL and right-XPL) of the sample showing the presence of OM (black colour) in voids of quartz rock grains and clay minerals, related to sample WH2-73. Abbreviation: DOM- dispersed OM; Ank-ankerite; Alb-albite; Dol-dolomite; Kfsp-potassium feldspar (microcline); Mus-muscovite; Qtz-quartz.

Quartz appears in anhedral forms, mainly transformed from microcrystalline quartz by recrystallisation (Figure 21 b). The muscovite is anhedral, has a flaked and scaly texture, high-birefringence aggregate, and some crystals are deformed by tectonic stress. Feldspar is mainly microcline, which occurs as anhedral grains and shows a lathlike habit, associated with partly albite and low-grade muscovite. Some feldspar crystals have been altered completely. Enrichment of hydromicas is a hydrothermal alteration widely developed in all samples, which is mainly formed by the hydration of mica and feldspar. The ankerite, Mg-Mn siderite, and dolomite occur as a veinlet texture.

The OM is opaque in the thin sections, and they usually appear as dark and partly brownish-grey fillings of voids and pores. They are optically isotropic under the transmitted light. The OM appears mostly as a filamentous, flow-like texture of bitumen and covers mainly quartz and rock fragment grain boundaries from very narrow (lesser than $1\mu\text{m}$) to broad ($\sim 0.5\text{ mm}$) fillings of voids and micro-cracks or appears as lenses showing the results of migration (Figure 21 b). Detailed descriptions of the OM types are discussed below.

4.2 Microscopic petrography of Bakyrchik samples

The nine rock samples are pelitic rocks abundant in clay minerals and contain typical sulphide and OM: Optically, I could identify muscovite, albite, and illite (with little amount smectite), hydrothermal carbonate minerals (ankerite and siderite), and quartz. Quartz is found as vein and veinlets which penetrate diagonally into laminated clay minerals as secondary minerals, indicating a hydrothermal origin. Hydrothermal quartz presents in the samples and is paragenetically associated with the arsenic sulphide ore minerals, antimony minerals, and solid bitumen as veins and veinlets (Figure 22 a and b).

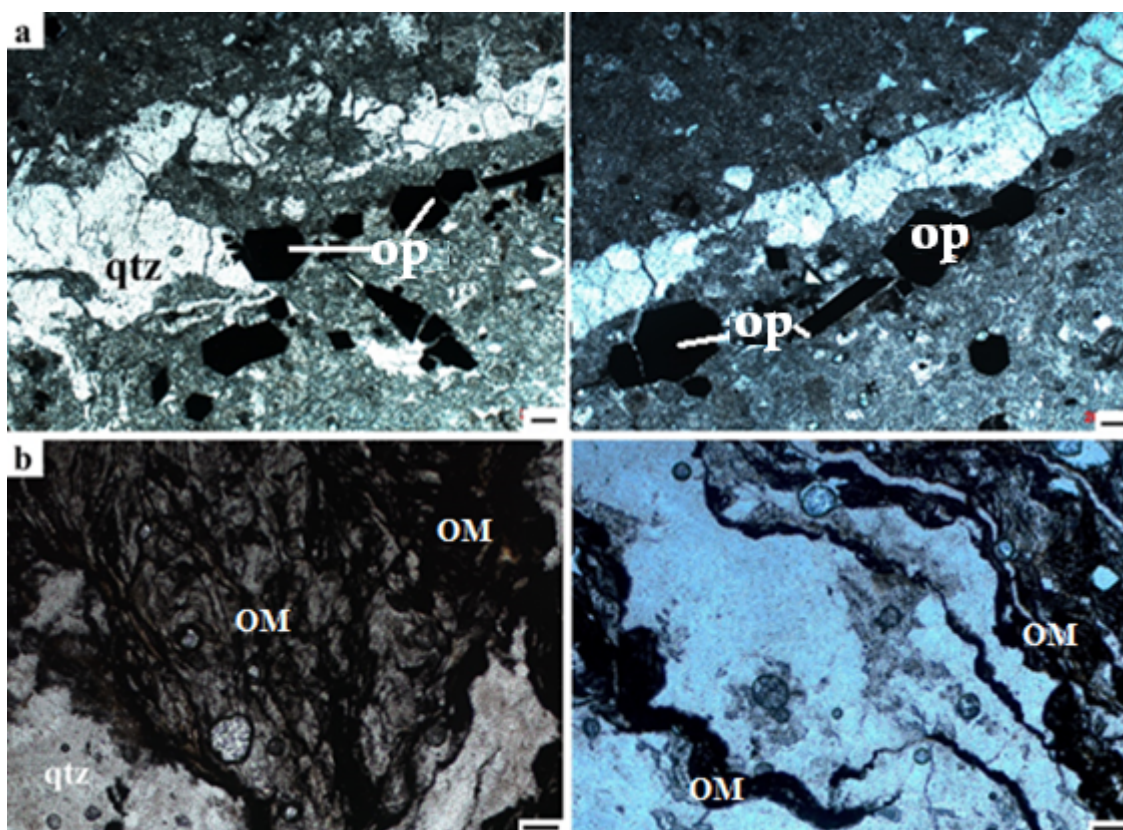


Figure 20 Transmitted microscopy images under plane-polarised light of hydrothermal quartz veins (qtz) with (a) opaque minerals (op) and (b) OM (typical pyrobitumen) in the samples Bak 2.5. Scale: 200 μm .

The studied samples are framework grains, accessory minerals, matrix, cement, and pores. The framework minerals are quartz and feldspar; the accessory mineral is muscovite, a small number of zircon, and rutile. The matrix is mostly clay minerals (mainly illite), while the precipitated cement (authigenic minerals) are quartz cement, carbonate cement, and authigenic clay mineral cement. Muscovite occurs more frequently than other accessory minerals. Plagioclase feldspar (albite) is the most dominant in the samples. The feldspar grains are texturally sub-rounded to sub-angular. Microcline only occurs in minor quantities and is absent in some samples. Illite occurs in high numbers and is the dominant clay mineral in the samples.

The OM is dominantly solid bitumen, I could find it in two types with reflected white light microscopy, which I will discuss in more detail in the organic petrology section. Both are filled with veins (Figure 22 b). Vitrinite and liptinie are seldom present in Bak 1, Bak 2.1, and Bak 2.5 samples. The solid bitumen of samples in thin sections is opaque, and it appears as dark and partly brownish-grey fillings of veins and veinlets. Usually, it is optically isotropic or weakly anisotropic.

It appears as flow-like textures and covers quartz grain boundaries with very narrow (less than $1\mu\text{m}$) to broad ($\sim 0.25\text{ mm}$) rims, filling in voids and microcracks or forming lenses showing the migration results.

Morphological characteristics and paragenetic association with ore minerals are described in more detail in the next sections.

5. Analytical and experimental results

5.1 The results of W-Mecsek samples

5.1.1 Organic petrology and vitrinite reflectance of W-Mecsek samples

The OM is found in six types, which generally occur in most of the samples. They are as follows:

- 1) autochthonous vitrinite from 5-10 μm to 150-200 μm particles (V1),
- 2) and reworked vitrinite V1
- 3) inertinite (I) which occurs in the W-Mecsek samples with 10-30 μm size,

- 4) brownish grey in normal light and non-fluorescing filamentous solid bitumen (B1),
- 5) non-fluorescing solid bitumen as thin veins or void fillings with higher reflectivity pyrobitumen (PB),
- 6) elongated shreds of graphite from 15-100 μm , (G)

1) In W-Mecsek sample, the most common maceral is vitrinite (V1). The particle size varies from 5 μm to 200 μm . Usually, the small size distribution is more common where the rock matrix is coarser, silty type; e.i. in WH2-072 and W2-076 samples between 883.3 and 895.6 m depth interval, respectively. The big vitrinite particles, telinite with visible inner texture and well-preserved cell walls, were found in the uppermost WH2-009 146.5 m (the additional sample) and the lower section of WH2-070, WH2-072, WH2-073 and WH2-076 samples from 865.9 to 895.6 m (Figure 24). Generally, these telinite particles have slightly lower reflectance than the dehydrated vitrinite and pyrobitumen, where cracks and oxidation patterns with lower reflectivity fields in the particle are typical. In the telinite particles, framboidal pyrite crystals are frequent.

There are bigger homogenous texture vitrinite particles where the size can (WH2-073 sample 883.3 m) be more than 100 μm , and in the inner texture 5 μm to 10 μm size inclusions of minerals, or their former place may occur (Figure 24 a-b). In the vicinity of the inner inclusions, oxidation rims and higher reflecting radiation haloes are visible in this vitrinite, desmocollinite.

2) Inertinite (I) is visible in the same silty samples where vitrinite is abundant. The concentration of inertinite is lower compared to vitrinite. Usually, the particle size varies from 10 μm to 60 μm , exceptionally in the uppermost WH-09 sample from 146.5 m where fusinite particle size can reach 200 μm (Figure 24 d).

3) In the wider fracture zones, fractured vitrinite's solid bitumen and deformed structures can occur in the hydrothermally developed quartz matrix (Figure 24 e). In my research work, I called this vitrinite form as reworked vitrinite and use the same signal as other vitrinites, V1.

4) Liptinite is not common. In some places in the big telinite particles, thin elongated forms with higher reflectivity than the telinite indicate their presence.

5) Solid bitumen occurs in two forms. The typical appearance of the non-fluorescing solid bitumen (B1) is dark brown to greyish colour in reflected normal light. Occurs as filamentous fillings between mineral or rock particles or appears as diffuse

brownish precipitation on the polished surface. The other solid bitumen, pyrobitumen, shows much higher reflectivity than vitrinite (Figure 24 c). This maceral appears as dots or in the form of fillings of fractures and voids of quartz and other rock particles (PB). It occurs as a continuous pretty thin membrane in the quartz veins smaller in diameter than 0.3 μm , which is adhered to the wall rocks and follows the crystal borders. This PB type is common in samples WH2-065, WH2-070, WH2-072, WH2-076 and WH2-077, below 847.5 m. Others also appear in the thicker veins and voids between minerals with highly reflecting grey colour and homogenous texture in normal light without fluorescence, usually from 5 μm to 20 μm .

Graphite (G) flakes are rarely found in the lower part of the section in samples of WH2-070 and WH2-076. The graphite flakes of the samples have 5-25 μm in width and 20-40 μm in length. (Figure 24 d).

Bitumens are represented by dark brown to greyish colour filamentous bitumen (B1) and pyrobitumen (PB) in reflected normal light and without fluorescence. The dark brownish filamentous, slightly fluorescing solid bitumen B1 (Figure 25 a, c and d) occurs as fillings between the rock particles from very thin to large fractures and voids of quartz. B1 is associated with autochthonous vitrinite V1 in the voids between cells or cracks. PB fills filling fractures and voids of quartz and appears like discrete dots or filaments, fillings in the thicker veins and voids with grey colour and homogenous texture in normal light without fluorescence in excited illumination (Figure 25 b).

The organic petrography analysis shows that the OM is dispersed (DOM) in six types of two bitumens (B1 and PB), vitrinites (V1), inertinites, liptinites and graphite (G) flake in samples (Figure 24 and 25). The DOM is mostly occurred as void and fracture fillings in quartz grains with weak or absent fluorescence excitation. The DOM is often associated with uranium and sulphide minerals, where the uranium-containing mineral matrix has greenish fluorescence in blue light excitation.

Random vitrinite reflectance (Ror%) of six samples shows that Ro% values range from 1.787 % to 2.252% and correspond to the to anthracite stage of coalification of the terrigenous DOM (Table 4). The lowest reflectance values were measured in sample WH2-076, 895.6 m, where the telinite texture was still recognisable and had lower reflectance than the homogenous vitrinite with dehydration cracks.

Table 3 Vitrinite reflectance measurements of the six selected rock samples.

Samples	WH2-57	WH2-65	WH2-70	WH2-72	WH2-76	WH2-77

Depth (m)	831,4	847,6	865,9	870,5	895,6	907,5
Min	1,720	1,902	1,998	1,600	1,598	2,190
Max	2,988	2,234	2,850	2,897	2,211	2,360
Ror%	2,251	2,113	2,381	2,024	1,787	2,252
STD	0,328	0,087	0,221	0,289	0,142	0,067
Number	20	11	22	18	17	5

Legends: Min: minimum measured reflectance of particle, The measured highest reflectance particle value, Ror%: random vitrinite reflectance, STD: standard deviation, Number: number of the readings, measurement in the sample

5.1.2 Ore mineralogy

The ore minerals in all samples were found in very tiny sizes (between 2 μm and 20 μm), which were difficult to identify by optical microscopy. Nevertheless, the uraninite occurs as a veinlet, needle-like form and mainly euhedral grains in the fractures with dolomite and quartz. It is intimately intergrown with reworked vitrinite and solid bitumen (Figure 26 a and b). The uraninite crystal grains occur up to 20 μm in reworked vitrinite than solid bitumen. Euhedral and needle-like forms of uraninite crystals mainly occurred within reworked vitrinite. The uraninite crystal growth (its size varies between 5-10 μm) is associated with the solid bitumen. Very small nanocrystalline aggregates of uraninite (up to 5 μm in diameter) are present in all solid bitumen veins; there are also rare examples of micron-scale veinlet of uraninite.

Based on uraninite morphology, the uraninite grains in the samples can be divided into two types: (1) detrital, euhedral uraninite, and (2) irregular secondary grains comprising submicrometric aggregates of smaller grains. Electron microscopy determines uranium ore minerals' chemical compositions and morphological fissures, showing more detail in the next sub-chapter.

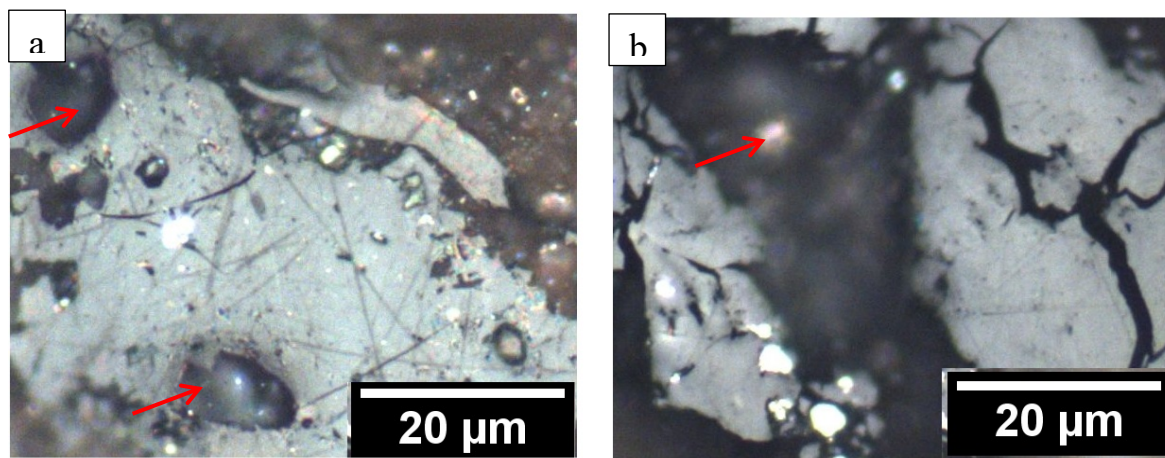


Figure 21 Uraninite minerals (white greyish grains, indicated by red arrows) associated with OM: a) uraninite with pyrobitumen (PB); b) uraninite with vitrinite (V1).

5.1.3 Mineralogical and chemical composition

The eight sandstone samples are composed mainly of quartz, feldspar, carbonates and clay; average values based on XRPD results show that quartz is up to 25 wt%; feldspar minerals consist total of 20.2 wt% of microcline (12%) and albite (8.2%); carbonate minerals range between 7.7 % ankerite (low-grade Mg-Mn siderite) and 19.5% of dolomite; clay minerals have total 14.3% of illite (13%), smectite (0.7%) and kaolinite (0.6%); and traces of muscovite, and titanomagnetite (Table 5).

Chemical compositions of the whole rock samples confirm that major felsic rock-forming minerals consisting of elements Si, Al, Na, K, Mg, Mn, and Ca vary from 2% to 65 % for quartz, potassium and sodium feldspar minerals, and carbonate minerals while minor elements Ti (average 0.28 %) and P (average 0.09 %) form compounds of titanium-oxide and phosphate minerals. Sulphide ore minerals of the whole rock samples consisted of elements As (up to 5027 ppm), Fe (up to 11.1%), Cu (up to 2662 ppm), Zn (up to 315) and Pb (up to 431). The high values of the elements show increasing pyrites in the samples of WH2-071 and WH2-072.

The amorphous matter content ranges from 4 wt% to 31 wt%, in average 12 wt%, mainly, the highest values in the two samples WH2-071 (31 wt%) and WH2-072 (17 wt%), calculated from the XRPD in Table 5 as amorphous material. The pyrite mineral content varies between 0.6 wt% and 33.4 wt%, in average 9 wt%. The pyrite content's highest values are shown in the two samples WH2-071 (14.4 wt%) and WH2-072 (34.4 wt%), as shown in Table 5.

5.1.4 Electron microscopic observation of OM and ore minerals

Microprobe analysis is carried out for the vitrinite (V1) particles associated with diagenetic pyrite crystal growth, and other veined bitumen types. These latter bitumens were also planned to test. Still, individual elements were not applicable due to the detection limit, because the vein fillings and filaments have very thin microtextures, which were also mentioned by other authors before (Belin, 1994); (Cardott, et al., 2007). The diagenetic pyrite growths in the vitrinite particles have a form of globular framboids, sometimes polyframboids in the samples (Hámor, 1994). EMPA-EDS show (Figure 27 a) that the framboidal pyrite is a sedimentary-diagenetic origin with a diameter of 10 microns showing arsenic content up to 1 wt%. The vitrinite contains less than 88 wt% organic carbon, 5.4 wt% oxygen, and a relatively high S content of over 5.5 wt% (Figure 27 a).

Besides the major elements, chlorine was found in the vitrinite in the sample WH2-065 ranging from 0.05 and 0.10 wt%.

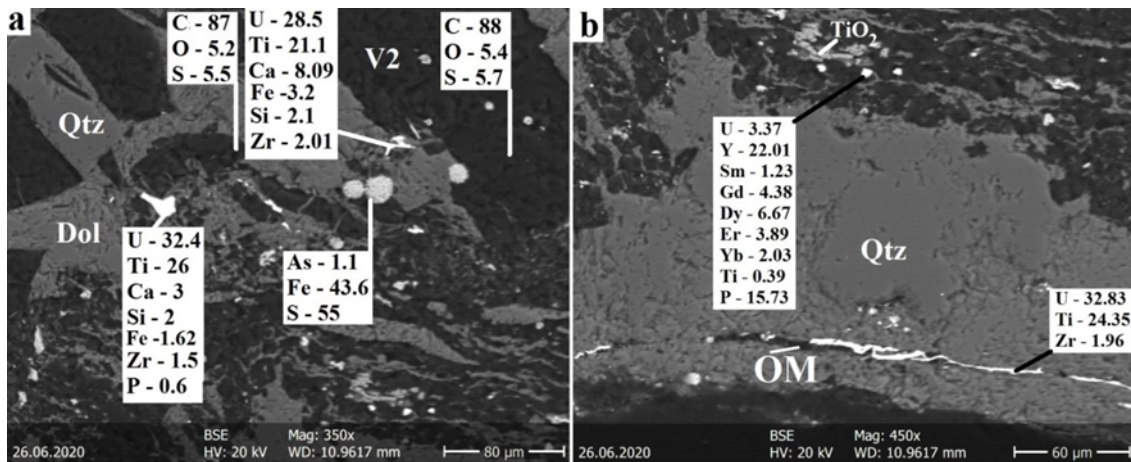


Figure 22 EMPA-BSE images with EDS measurement showing chemical contents of vitrinite (V1) and subhedral Ti-Ca-rich coffinite; and (b) subhedral U and REE-bearing phosphorus minerals and needle-like Ti-rich uraninite within OM in the dolomite veins with quartz grains of the sample – WH2-70. (unit wt%).

The samples found three phases of uranium ores: uraninite (pitchblende), coffinite, and U-REE-bearing phosphorus minerals. The uraninite with titanium occurs as a veinlet or needle-like form in the fractures with dolomite and quartz and is intimately intergrown with OM. The length of needle-like uraninite varies from 10 μm to greater than 100 μm , while the coffinite is around 20 μm . In both minerals, titanium (up to 26 wt%) also occurs in significant concentrations. Calcium (3-8 wt%), silicon (2 wt%), phosphor (up to 0.6 wt% and partly absent), and zirconium (up to 2 wt%) elements enrich solely in the coffinite. Although, the most abundant U mineral is uraninite (UO_2), it slightly deviates from the stoichiometric formula due to titanium and zirconium enrichment.

The second and less common mineral type is the calcium and phosphor-rich coffinite $[(\text{U,Ca})(\text{P,Si})\text{O}_4]$. It forms subhedral flakes in the vicinities of dolomite. We could not find pure coffinite in our samples (Figure 28 a and b). The third type of uranium mineral is the low-grade U-bearing phosphorus mineral with a uranium concentration of up to 3.4 wt%. This type is found in the finely dispersed form of 3 μm in diameter in particles of the vitrinite and the clay minerals. The most significant rare earth elements in the uranium minerals are the following: yttrium (22 wt%), dysprosium (6.7 wt%), gadolinium (4.4 wt%), erbium (3.9 wt%), ytterbium (2 wt%), and samarium (1.3 wt%). Additionally, the

accessory minerals are found in trace amounts of monazite (size, 20-30 μm) and zircon (12 μm) associated with clay minerals and OM of the samples.

Two recrystallised pyrites (cement and euhedral forms) growths occur mostly on clay minerals with the chemical content of arsenic in them up to 4 wt%. The various growths of sulfosalt minerals occur with arsenic, copper, antimony, zinc, and iron vicinity of voids of the euhedral pyrite. Sulfosalt minerals (As-Cu-Sb-Zn-Fe) contain much more copper (37 wt%), arsenic (22 wt%) elements decreasing in order with zinc (5.6 wt%), iron (4.5 wt%), and antimony (1 wt%) (shown in Figure 28 a and b).

Other sulphide minerals such as galena, sphalerite, and antimonite are found as finely disseminated forms and rare or absent in several samples. The galena was found in fractures of potassium-feldspar in the matrix of the vitrinite particles in two samples; its size varies from 3 μm in the sample WH2-65 and to 20 μm in the WH2-077 while the sphalerite in size up to 10 μm and antimonite 5 μm grown up in Fe-Mg carbonate minerals which occur solely in the sample WH2-073. Sphalerite is found up to 10 μm in pores of sample WH2-073, whereas galena occurs in size between 10-50 μm (samples WH2-077) and the framboidal form up to 0.5 μm within the vitrinite as well (sample WH2-065).

We could not find any free grains of precious metals in the vitrinite particles, early diagenetic pyrite, and recrystallised pyrites.

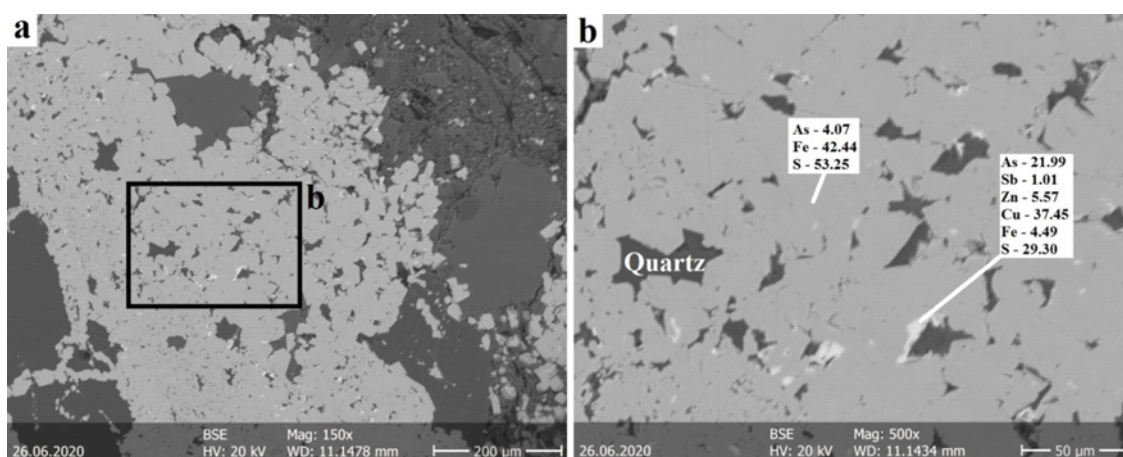


Figure 23 EPMA-BSE images of euhedral pyrite grains with arsenic content in grey (a), and sulfosalt minerals with high arsenic (and copper) element (b), (unit in wt%) of the sample – WH2-72.

5.1.5 X-Ray maps of OM for carbon and sulphur content

The BSE image of Figure 29 a was selected to analyse the vitrinites on the X-ray map indicating elemental analysis values of 86 wt% carbon and 5.7 wt% sulphur. Several greyish-white spots in the clay matrix and at the margins of vitrinites show growths of individual, framboidal, and polyframboidal pyrite crystals with of arsenic content of 0.4 wt% (Figure 29 a and b).

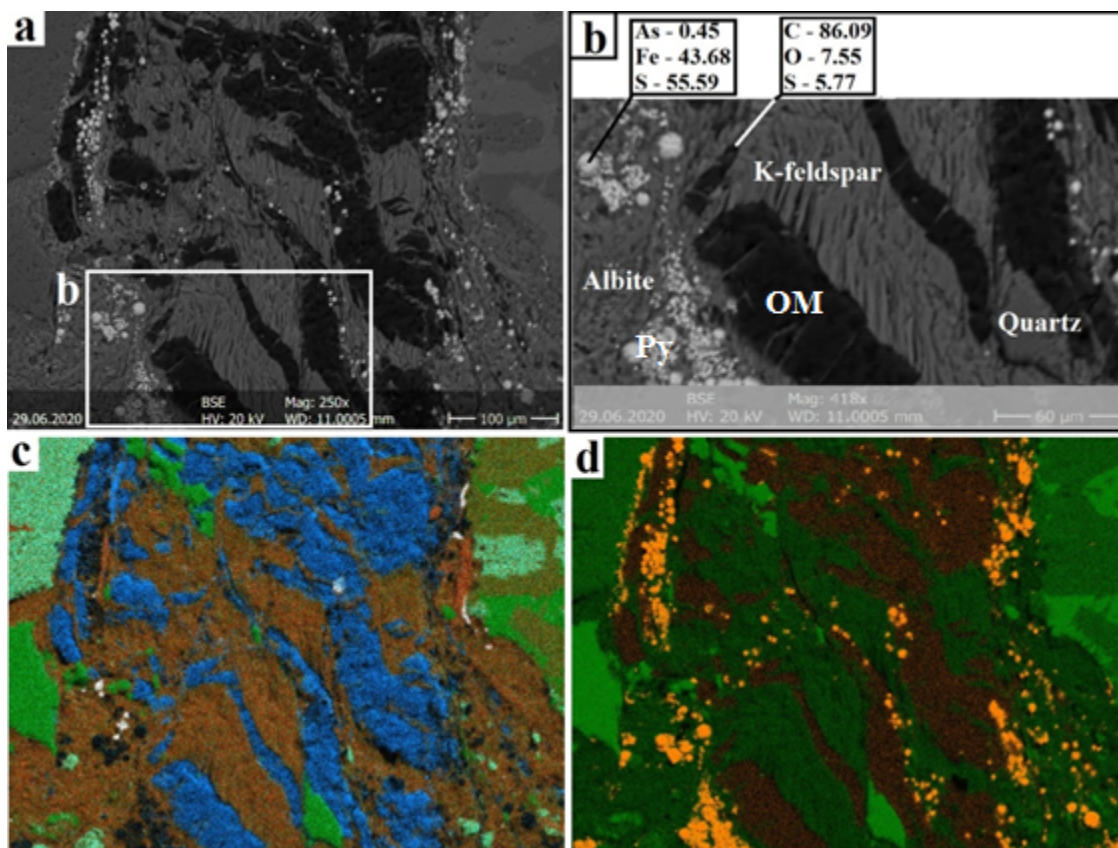


Figure 24 EMPA-EDS X-Ray map with quantitative results of fractured vitrinite particle (V1) associated with framboidal pyrites in quartz matrix: BSE image (a); EDS measurement (b), and X-Ray mapping of the image (c and d): in the image (c) fractured vitrinite is shown in blue within the rock matrixes (denoted albite in cyan, quartz in green, K-feldspar in brown, pyrite in dark blue and titanium oxide in white); and in the image (d) sulphur content of vitrinite (dark orange) and pyrite (light orange) with surrounding silicates (in green quartz and dark green K-feldspar) from the sample – WH2-76. (OM-organic matter and py-pyrite).

(Tseng, et al., 1986); (Harrison, 1991); and (Ward & Gurba, 1998) have measured successfully the amount of organic sulphur in individual maceral grains of OM. (Ward &

Gurba, 1998) have explained that EMPA may detect all organic forms of sulphur content than a chemical combination analysis with pyritic sulphur and sulfate.

The EMPA X-ray map indicates the vitrinites as blue, associated with pyrite (dark blue, see in Figure 29 c) into grains of microcline (brown color) surrounding other minerals' growths. The organic sulphur is associated totally with the vitrinite, denoted in colour as dark orange. In contrast, sulphur of pyrites distributes along and within the vitrinite matrix and into the feldspar grains shown in Figure 29 d as light orange colour.

5.1.6 Thermal maturity and reflectance

The result of Micro-Raman spectroscopy of OM is the following for the non-fluorescing bitumen (B1) and pyrobitumen (PB), vitrinite telnite and vitrodetrinite (V1). The result focuses on the first-order region, which is associated with relatively high intensive two bands of D and G between 1360 – 1600 cm^{-1} (the bands are sensitive to maturity for coals, (Quirico, et al., 2003)) and quite weak bands of D3 at 1515 cm^{-1} and D4 at 1160 cm^{-1} , and the second region associated with relatively low intensity of three S bands at 2700 cm^{-1} , 2940 cm^{-1} and 3200 cm^{-1} following studies of the altered coaly materials for evaluations of (1) altered temperatures and (2) thermal maturity or the corresponding coal rank based on the methods of (Barker & Pawlewicz, 1994); (Quirico, et al., 2005); (Liu, et al., 2013); (Hinrichs, et al., 2014); (Li, et al., 2019a) and (Li, et al., 2019b).

Raman's results indicate that the vitrinite in our samples correlates well with the structural evolution of bituminous coal from in Hunan Province, China in the study of (Li, et al., 2019a).

The Raman measurement concentrates on four parameters like peak height (PH), inter-peak interval ratio (G-D), peak height ratio (R1, for intensity) and full width at half maximum (FWHM). The estimation for the altered temperature of the terrigenous wood origin materials was carried out by the Raman parameters using the earlier temperature calculation formula by (Barker & Pawlewicz, 1994), which was later modified by (Li, et al., 2019a), and called a vitrinite reflectance geothermometers (VRG). The modified formula of (Li, et al., 2019a) the formula (1).

$$T_{\text{peak}} (\text{°C}) = -7.8829 (\text{G FWHM}) + 752.59, \quad (1)$$

is restricted to the temperature range of $\sim 70 - 300^{\circ}\text{C}$ based on peak temperature (T_{peak}) and to the full width at half maximum of the G band (G-FWHM). This algorithm is used

for the OM impacted by active hydrothermal process and anomalously high burial heating in the vicinity of magmatic intrusions, where the vitrinite reflectance (R_o) varies from 0.55% to 3.17% (Barker & Pawlewicz, 1994); (Chen, et al., 2017); (Li, et al., 2019a) or/and radiolytic alteration of OM caused by ionising radiation resulting from the decay of uranium, where increasing vitrinite reflectance of the OM, from about 0.7% to 3.4% in contact with the grain of uranium minerals (Eakin & Gize, 1992); (Machovič, et al., 2021).

The reflectance of the OM of vitrinite particles was determined by laser Raman characteristic peaks (peak height) using the Liu (Liu, et al., 2013) equation, which is equivalent to vitrinite reflectance that can reflect different maturation grades and the surface optical properties of samples (Liu, et al., 2013). The Liu equation is based on the matching relationship between Raman inter-peak interval ($G - D$), and vitrinite reflectance ($vR_o\%$) can be derived as (2)

$$R_{mcR_o} \% = 0.0537 d(G - D) - 11.21, \quad (2)$$

where $R_{mcR_o}\%$ refers to Raman reflectance using Raman parameters; $d(G - D)$ refers to Raman peak interval, which is more applicable for the coaly materials (high maturation stage with mineral inclusion) in a metallic deposit (Liu, et al., 2013), which corresponds well to our case. The regular change of the distance between vibration peaks of G and D and the ratio of their heights with the increase of maturity in samples were calculated to give the equivalent reflectivity of vitrinite ($V1$), showing maturity parameters in Table 6. The reflectance in the two vitrinite types indicates that the OM is in range of medium rank coal with 1.57% $R_{mcR_o} \%$ equivalent vitrinite reflectance, listed by works of (Quirico, et al., 2003) and (Quirico, et al., 2005) according to the standard of ASTM-2798.

The solid bitumens, vitrodetrinite and vitrinites are described separately below, shown in Figure 30 and Table 6. Results were carried out on 10 spot analyses on each particle of the OM. All the studied OM has low intensity (between 515 and 2790) for the D band and high intensity (between 675 and 3625) for the G band of the Raman spectra, respectively. Separately, the veined pyrobitumen (PB, hard to measure with the lowest diameter of 20 μm) is characterised by a wide (up to 231.41 cm^{-1} FWHM) D band at around $1362.0 \pm 4.0 \text{ cm}^{-1}$ and a narrow (up to 74.14 cm^{-1} FWHM) G band at $1601.0 \pm 3.88 \text{ cm}^{-1}$ ($n = 10$) while the non-fluorescing bitumen (B1) has a wide D peak (up to 236.24 cm^{-1} FWHM) at a wavenumber of $1365.7 \pm 1.1 \text{ cm}^{-1}$ and a narrow G peak (up to 79.01 cm^{-1} FWHM) at a wavenumber of $1601.0 \pm 9.0 \text{ cm}^{-1}$.

The autochthonous telinite (V1) is characterized by a wide (up to 235.3 cm⁻¹ FWHM) D band at around 1364 ± 0.8 cm⁻¹ (n = 10) and narrow (up to 78.1 cm⁻¹ FWHM) G band at 1602.0 ± 0.9 cm⁻¹.

The increase of the equivalent vitrinite reflectance of Raman reflectance correlates well with the increasing values of the parameters of inter-peak interval (G-D) and peak height ratio of (Liu, et al., 2013),.

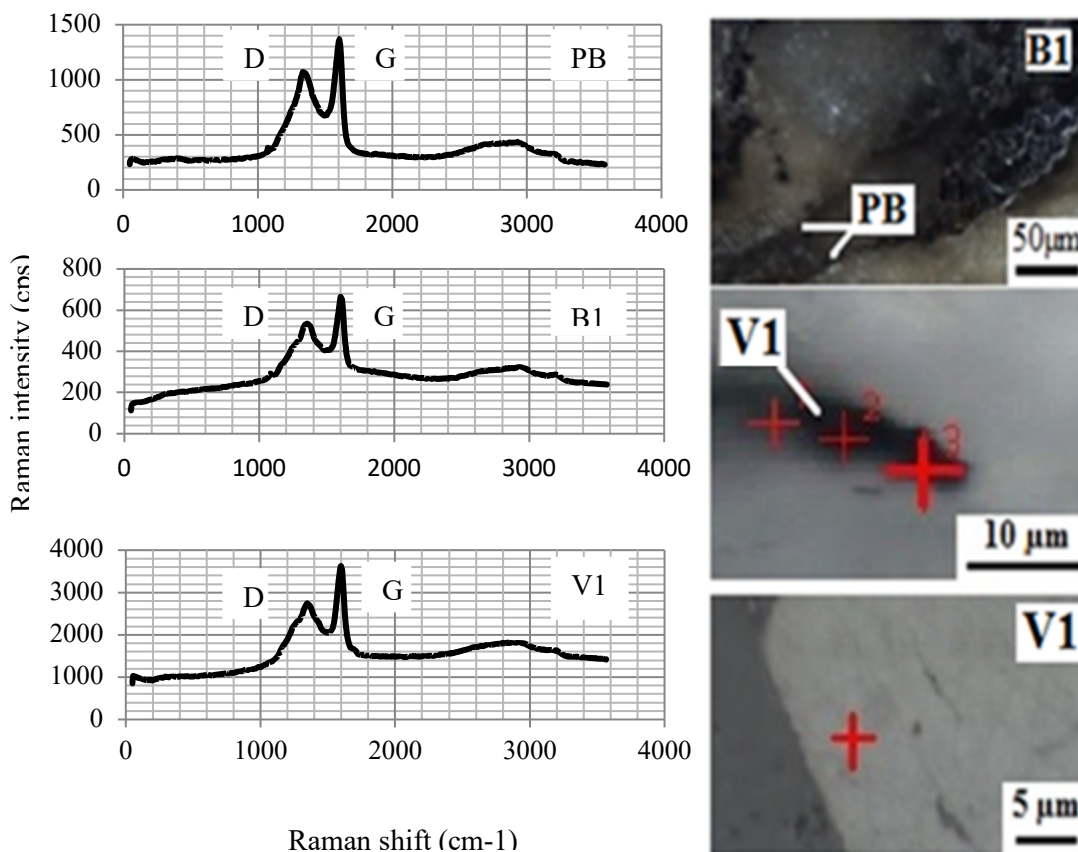


Figure 25 Raman microscopy measurement of non-fluorescing bitumen (B1) and pyrobitumen (PB), and autochthonous vitrinite telinite (V1) showing Raman spectra (left side) of D and G peaks and optical photomicrographs (right side) under cross-polarized light.

Table 4 Relevant Raman parameters for organic materials for the selected rock samples: R1 (PH ratio) = (ID/IG), where ID and IG are the intensity of the D and G band (based on (Li, et al., 2019a)).

OM	RP	RS (cm ⁻¹)	G-D	FWHM (cm ⁻¹)	PH	R1	<i>R_{mcR_o}</i> %	T°C (± 30°C)

PB	G	1601.0	239.0	74.14	1380	0.782	1.62	144.5
	D	1362.0		231.41	1080			
B1	G	1600.1	234.4	79.01	675	0.762	1.37	129.7
	D	1365.7		236.24	515			
V1	G	1602.9	238.1	78.11	3625	0.769	1.57	136.8
	D	1364.8		235.28	2790			

Abbreviation: OM – dispersed OM; PB – pyrobitumen, B1 – non-fluorescing bitumen, and V1 – telinite; RP - Raman peak mark; RS – Raman shift; FWHM - full width at half maximum; PH - Peak height; G-D – Inter-peak interval; R1 – peak height ratio; RmcRo% – Raman reflectance or equivalent vitrinite reflectance calculated from the Raman parameters expressed in equivalent to vitrinite reflectance; T - Temperature. The results from samples: PB from WH2-072; B1 from WH2-073; V1 from WH2-077 and WH2-057.

We can conclude that the Raman method measured much less Raman reflectance RmRo% (up to 1.62 %) of OM than vitrinite reflectance (2.2 %). It may be why vitrinite identification remains the major challenge for many samples (Ronald, et al., 2018). Moreover, inertinite and solid bitumen can be notoriously difficult to accurately distinguish from vitrinite, especially if the OM is in low abundance (< 1% TOC) and finely disseminated, or the solid bitumen component is in high abundance (Ronald, et al., 2018).

5.1.7 Total organic content (TOC) and organic elemental (H, N, S) analysis

Total organic carbon (TOC %) of eight samples was found in various ranges from 0.15 wt% to 1.1 wt% (average 0.83 wt%) in the eight samples. The lowest grade of TOC % was found at 0.15 wt% in the sample WH2-57. The concentration of the OM changes gradually with increasing depth, in a mean value of TOC is 0.61 % of the sample WH2-72 while the highest TOC content is 1.1 % which shows the sample WH2-71 (Table 7).

Table 5 Total organic carbon (TOC %), H, N and S of eight whole-rock samples.

Samples	Depth (m)	TOC % value	H% value	N% value	S% value
WH2-057	831.4	0.15	0.23	0.025	0.16
WH2-065	847.6	0.37	0.97	0.027	3.22
WH2-070	865.9	0.22	0.23	0.033	0.78
WH2-071	870.0	1.10	1.74	0.14	4.80
WH2-072	870.5	0.61	1.31	0.03	2.23
WH2-073	883.3	0.17	0.23	0.027	1.67
WH2-076	895.6	0.39	0.65	0.043	3.54
WH2-077	907.5	0.25	0.52	0.15	5.81

The organic elemental analyser determined hydrogen, nitrogen and sulphur. Hydrogen contents ranges from 0.23 wt% (sample WH2-57) to 1.74 wt% in sample (WH2-71) (average 0.76 wt%) while nitrogen varies from 0.025 wt% (sample WH2-57) to 0.15 wt% sample (WH2-77) (average 0.073 wt%), fluctuated between the samples, respectively.

Total sulphur content varies in the samples from 0.16 wt% (sample WH2-57) to 5.81 wt% (sample WH2-77), and its average value is 2.79 wt%.

5.1.8 Functional group composition and soluble OM analysis

The soluble OM has been used for the interpretation of results of FTIR analysis based on the research works of (Andreas, et al., 2003), (Balachandran, 2014), and (Weizhen, et al., 2017).

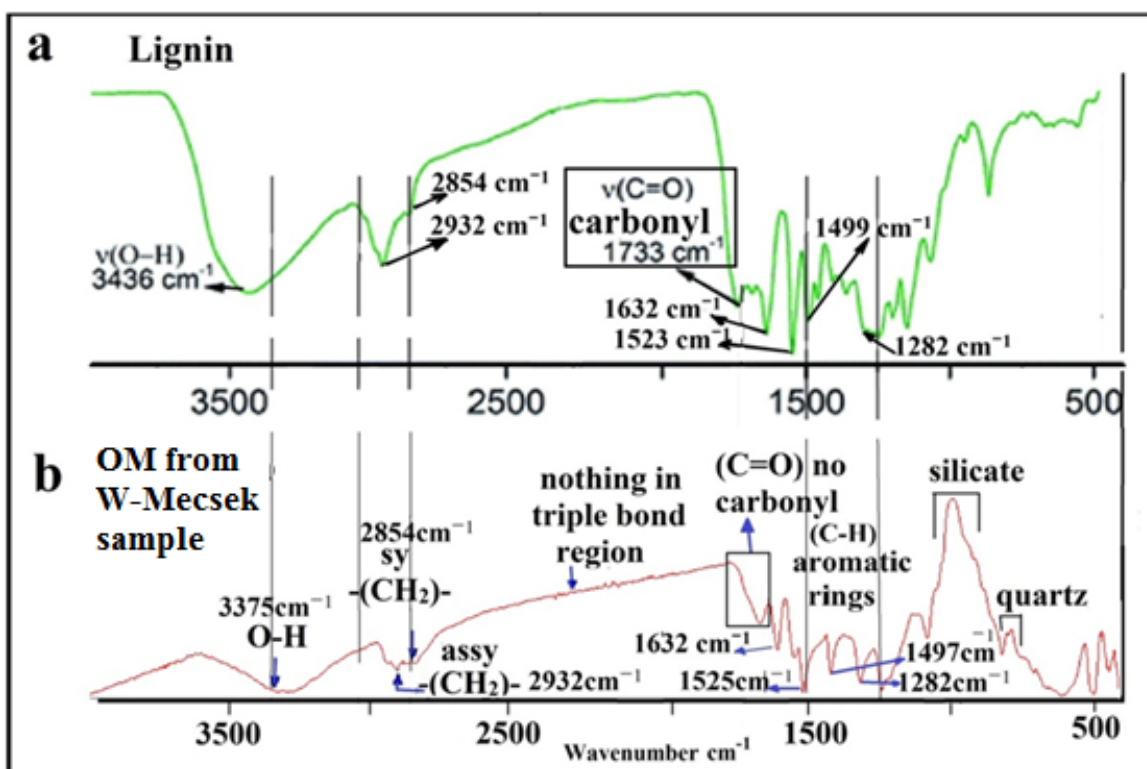


Figure 26 FTIR analysis and comparison of organic fractions: (a) molecular structure of lignin with silica nanocomposites (modified from (Weizhen, et al., 2017)); (b) OM with rock matrices of carbonate free, shown the sample of WH2-77 (indicated no carbonyl in frame).

FTIR spectra assigned the OM composition that the broad peak at 3375 cm^{-1} has the stretching vibrations hydroxyl (O–H) groups (very small amount) and methylene groups appear like anti-symmetric stretching at peak 2932 cm^{-1} and stretching at peak 2854 cm^{-1} , respectively. The peaks at 1632 cm^{-1} , 1525 cm^{-1} , 1497 cm^{-1} and 1282 cm^{-1} to characteristic vibrations from aromatic rings, which is characterised by polycyclic aromatic hydrocarbon. The stretching vibration of C–O for carbonyl groups is absent in the samples.

The OM structure in the samples was compared to identify its exact molecular structure using a pattern of phenolic hydroxyl group material. They compared with characteristic peaks of the phenolic hydroxyl group (Figure 31 a) and the studied OM characteristic peaks (Figure 31 b). The characteristic vibrations from aromatic rings of the phenolic hydroxyl group at 1632 cm^{-1} , 1523 cm^{-1} , 1499 cm^{-1} and 1282 cm^{-1} . These similar characteristic peaks of vibrations reflect the studied OM was continuing similar stretching vibrations of the phenolic hydroxyl group at 2854 cm^{-1} and 2931 cm^{-1} and almost similar to the broad peak of the phenolic hydroxyl group at 1436 cm^{-1} , except the carbonyl stretch of the phenolic hydroxyl group peak at 1733 cm^{-1} , where it is absent in composition of the studied OM. The carbonyl group could be disappeared in the studied OM during a decarboxylation process. Other OM composition and structure functional groups correspond with the phenolic hydroxyl group characteristic of lignin material.

The extractable fraction and the volume of the soluble OM were very small, and it was not fractionated further.

5.1.9 Sequential extraction experimental results

Three sequential extraction stages were used to remove the gold and silver from the soluble OM of the samples, associated with two exchangeable fractions bounding to the OM and arsenic sulphide minerals like pyrite and sulfosalts.

The optical and electron microscope techniques have not confirmed the presence of native gold grains in the OM of the samples and even in the arsenian pyrites and some sulfosalt minerals. The experimental extractions of gold were successful for the previously separated organic fraction and the handpicked, arsenian pyrite bearing minerals. Moreover, the organic fraction contains silver, but no platinum metals besides gold. This suggests that the gold and silver are very finely dispersed within the organic matrix.

Table 6 Results of extracted metals from the whole rock samples in the three stages.

Samples	Three stages with chemicals and elements values (unit, ppm)							
	I stage (KOH) / OM							
	Au	Ag	As	Fe	Cu	Zn	Pb	Sb
WH2-057	2.28	0.11	2.2	1.8	0.03	0.02	-	-
WH2-073	1.89	0.01	5.3	0.1	0.36	0.36	-	0.05
WH2-077	3.28	0.07	3.3	0.3	0.07	0.02	-	-
Average (unit, ppm)	2.48	0.06	3.6	0.73	0.15	0.13	-	0.025
Samples	II stage (HCl) / Sulphide minerals							
	Au	Ag	As	Fe	Cu	Zn	Pb	Sb
	WH2-057	0.20	0.19	2.9	749	0.05	0.4	0.4

WH2-073	0.44	0.18	7.1	1041	0.55	7.1	5.6	-
WH2-077	0.63	0.15	6.7	639	0.75	0.5	29	-
Average (unit, ppm)	0.42	0.17	5.56	809	0.45	2.6	11.6	-
Samples	III stage (Agua regia) / Residual materials							
	Au	Ag	As	Fe	Cu	Zn	Pb	Sb
WH2-057	-	1.19	84	393	0.4	0.6	0.3	0.33
WH2-073	-	0.89	61.0	1045	2.5	18	2.1	0.06
WH2-077	-	0.78	37.5	1136	2.8	1.2	3.4	0.07
Average (unit, ppm)	-	0.95	60.8	858	1.9	6.6	1.9	0.15

Note: TOC (%) concentration reaches 0.15 % in WH2-057; 0.17% in WH2-073 and 0.25% in WH2-077

ICP-OES measured the gold for gold concentrations accompanied by silver shown in Tables 8 from the two different phases of the soluble organic fractions and arsenic sulphide minerals from three samples.

In the first stage of the sequential fractioning, the total amount of extracted gold was 7.45 ppm (2.48 g/t on average) and silver 0.19 ppm, respectively for both elements. Other elements were in much smaller quantity at this stage, see in Table 8.

During the second sequential stage, the high concentration of hydrogen chloride leached a total amount of gold at 1.27 ppm (0.42 g/t on average) and silver at 0.52 ppm, additional higher amounts of iron at 1041 ppm and lead up to 29 ppm, while arsenic remained in smaller quantity.

During the third sequestration, Aqua regia dissolved the remaining metals, sulfosalt and pyrite. In the dissolved material, arsenic (up to 84 ppm), iron (1136 ppm), copper (2.8 ppm), zinc (18 ppm), antimony (0.3 ppm) remained with an elevated total concentration of silver up to 2.86 ppm, most likely from sulfosalt minerals as tetrahedrite and Cu-As-Zn-Fe-Sb sulfosalts, but the gold is absent.

The gold and silver concentrations in the OM and arsenic sulphide minerals (pyrite and sulfosalts) differed. The three stages of experiments strengthened that most of the gold is associated with the OM (7.45 ppm) compared to the sulphide minerals (1.27 ppm). At the same time, the silver concentration is greater in the sulphide minerals (3.38 ppm) than in the OM (0.19 ppm). The highest gold content has the sample WH2-077. However, the sample WH2-057 shows the highest silver value (Table 8).

5.1.10 LA-ICP-MS

The LA-ICP-MS line spot analyses on the OM grain (Figure 32) show good signals of carbon content with higher signals of U and Th and the presence of signals of Au and

Ag. The signals of radioactive elements with Au increase more in the core of the grain of OM than in the rim.

Line profiles from the host into pyrite crystals show the presence of Au and Ag counts within the pyrite, with more signals in the core than in the rim of pyrite. Arsenic content is higher in the core than in the rim of pyrite crystals (Figure 32).

The LA-ICP-MS analyses of 33 spots with good signals of a total of 45 on the grains of OM, mainly reworked vitrinite shows the presence of Au and Ag, ranging from 1.19 ppm to 5.06 ppm Au; and 1 ppm to 90 ppm Ag.(Figure 32 a, and Table 9, 10 and 11).

The value of Au enriches with increasing the values of radioactive elements (the highest values of 61 ppm U and 9 ppm Th) and arsenic content (the highest value of 2558 ppm). Table 10 shows detectable thirty-three gold signals of the sample WH2-065 with selected the highest values from 5.05 ppm to below detection limit while the remaining samples have low signals.

In the case of pyrobitumen of the sample WH2-065, 50 spots on the grains of veined pyrobitumen were analysed with a searching size of 100 µm in width but mostly was lesser than 50 µm. The very small-sized veined pyrobitumen with tiny forms was the main reason for its inaccessibility, showing low signals of trace elements and gold.

The spot analyses on the OM show other trace elements from its associated mineral elements of Fe (average 26431 ppm), As (average 256.7 ppm), Cu (average 2984 ppm), Pb (average 4535 ppm), and Zn (average 610 ppm), and other many additional elements of Ti (411142 ppm), Mn (average 9206 ppm), Ni (average 1990 ppm), Ga (average 739 ppm), Sr (average 2844 ppm), Y (920 ppm), Nb (average 1034 ppm), Mo (average 663 ppm), Ba (average 11100), and Hf (average 509 ppm).

Concentrations in the OM of many other elements are mostly low signals Bi, W, Ta, Ge and Sb (average between 35 ppm and 231 ppm) and below the detection limit, such as C, S, Se, Pd and Pt.

The LA-ICP-MS spot analyses on crystal grains of pyrites detect (Table 11) much lesser Au content (up to 0.67 ppm) but much higher values of Ag (up to 43 ppm) and As contents (up to 25146 ppm) than in the OM. Nevertheless, gold is present in both euhedral and cement pyrites showing almost similar concentrations below the detection limit to 0.67 ppm, with an average value of 0.32 ppm.

The euhedral pyrite contains higher concentrations of Cu (average 2361 ppm), Zn (average 367 ppm), Pb (average 2025 ppm), and Sb (average 64), while the cement pyrite ranges low concentrations of the elements mentioned above. Nevertheless, other trace

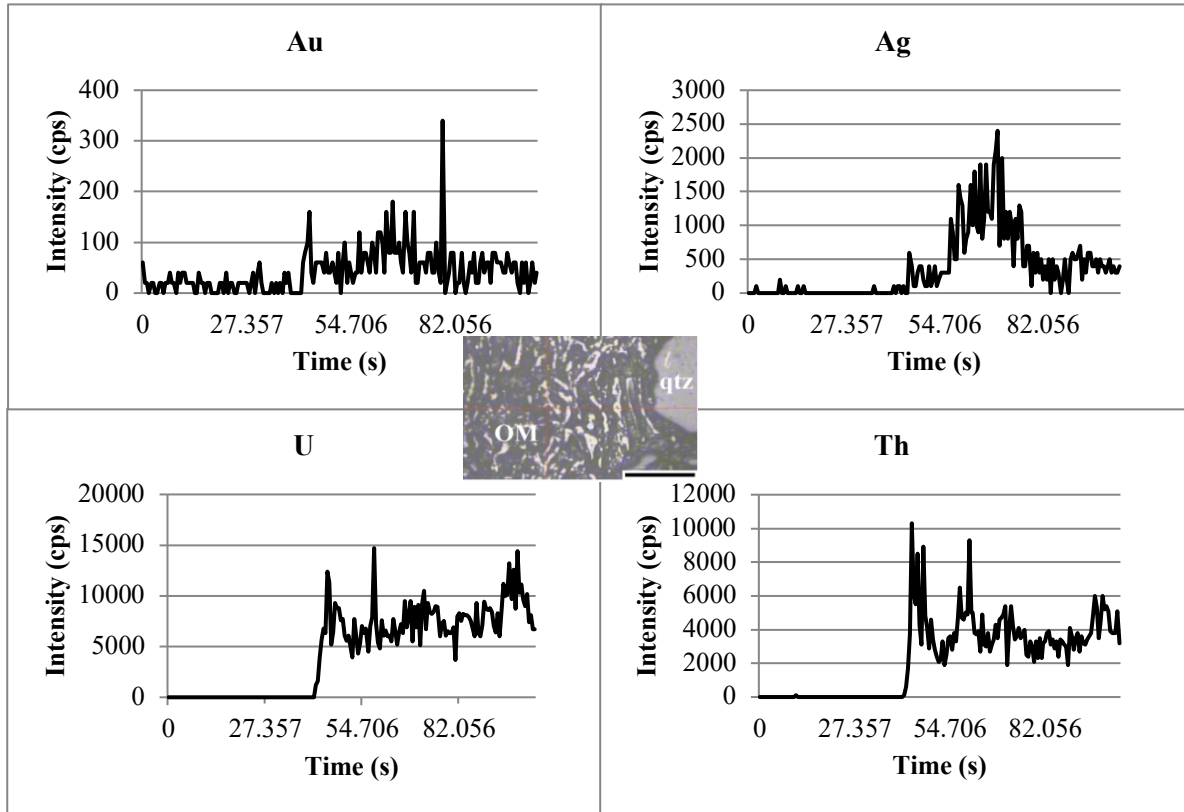


Figure 27 Representative time-resolved LA-ICP-MS depth profiles for Au, Ag, U and Th along a liner track through grains of OM in the sample of WH-2-065. (Scale 100 μm in the photomicrograph).

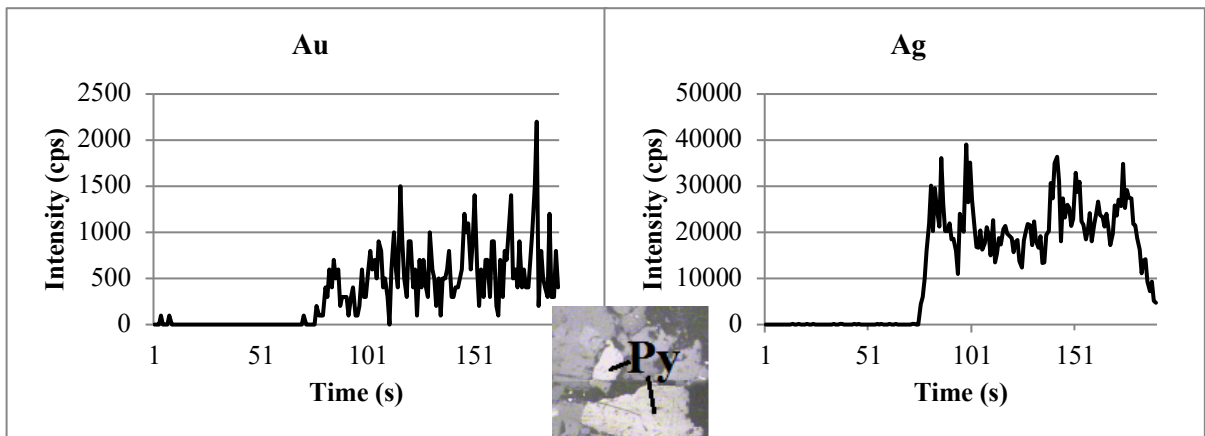


Figure 28 Representative time-resolved LA-ICP-MS depth profiles for Au and Ag along a liner track through pyrite grains of pyrite in the sample of WH-2-072.

elements in the cement pyrite are higher than in the euhedral pyrite, such as Mn (average 58 ppm), Nb (average 3 ppm), Ni (average 136 ppm), Ag (average 36 ppm), Ti (medium

145 ppm), Ba (average 27 ppm), Sr (average 6 ppm) and similar concentrations of As (average up to 23 020 ppm), Mo (average up to 693 ppm) and W (average 0.09 ppm) in both pyrites. The highest Cu and Zn and Pb values in the euhedral can be explained that the pyrite occurring next to Cu-rich sulfosalt minerals in its pores and some minor galena crystal inclusions.

For all two pyrite generations, the concentrations of many other elements are mostly below the detection limit, such as Sc, Cr, Ga, Ge, Zr, Hf, Ta, Bi, Th, and U.

The results of LA-ICP-MS spot analyses correspond with the results of ICP-OES, where the value of Au is more in OM than in pyrite, but the value of silver is more in pyrite than in OM. The results of LA-ICP-MS confirm the results of ICP-OES.

The dataset of LA-ICP-MS shows that gold concentrations are relatively uniform among the samples. Most of the LA-ICP-MS time-resolved depth profiles for Au, Ag, U and Th in OM are wavy, displaying several spikes. The pyrite grains (cement texture) also show many spiky depth-concentration for Au and Ag (Figure 33, and Figure 34), indicating the occurrence of Au primarily as a solid solution in a lattice or as homogeneously distributed nanoparticles (Cook, et al., 2009); (Sung, et al., 2009); (Gao, et al., 2019).

5.2 The results of Bakyrchik

5.2.1 Organic Petrology

The OM occurs in all nine samples. Vitrinite is very seldom and it usually occurs as 5 μm to 20 μm elongated angular grains in the mineral matrix. The other form of vitrinite was in the Bak 1 sample, where a bigger, fractured grain with more than 200 μm length in total can be seen as fractured pieces of 20x50 μm angular particles. The original particle had fractured epigenetically when the crystal growth of the hydrothermal quartz embedded it. The thermal maturity level of samples is in the coalification stage of anthracite, and the liptinite optical feature also conforms. These fractured OM particles were the only place where liptinite is visible with higher reflecting sporinite. Inertinite is not a typical maceral of the samples. Because the fractured vitrinite particles with sporinite are very uncommon in the samples, I have considered it reworked vitrinite which trapped and fracked into angular-shaped macerals in the middle of the hydrothermal fracture zone. They are more or less parallel with the fracture orientation, located in the middle of large voids later filled by spheroidally growing quartz. The growing pattern of quartz crystals is perpendicular to the

orientation of the elongated particles. This reworked vitrinite appears relatively rarely, does it occur in the first and second groups of samples (found only in three samples of Bak 1, Bak 2.1 and Bak 2.5). In the reworked vitrinite, framboidal pyrite is frequent.

Dark brown solid bitumen (B1) occurs as a diffuse bituminous matrix or a continuous pretty thin membrane on the quartz, which is also adhered also to the wall rocks. This solid bitumen type usually occurs on most quartz veins (Figure 35).

The solid bitumen shows discontinuous membrane fillings and veins with a diameter smaller than 0.5 μm , adhered to wall rocks and occurs in the veinlets like patches of diffused bitumen or following the grain boundaries (Figure 35 a and b). Solid bitumen is often associated with sulphide ore minerals in hydrothermal quartz veins and veinlets.

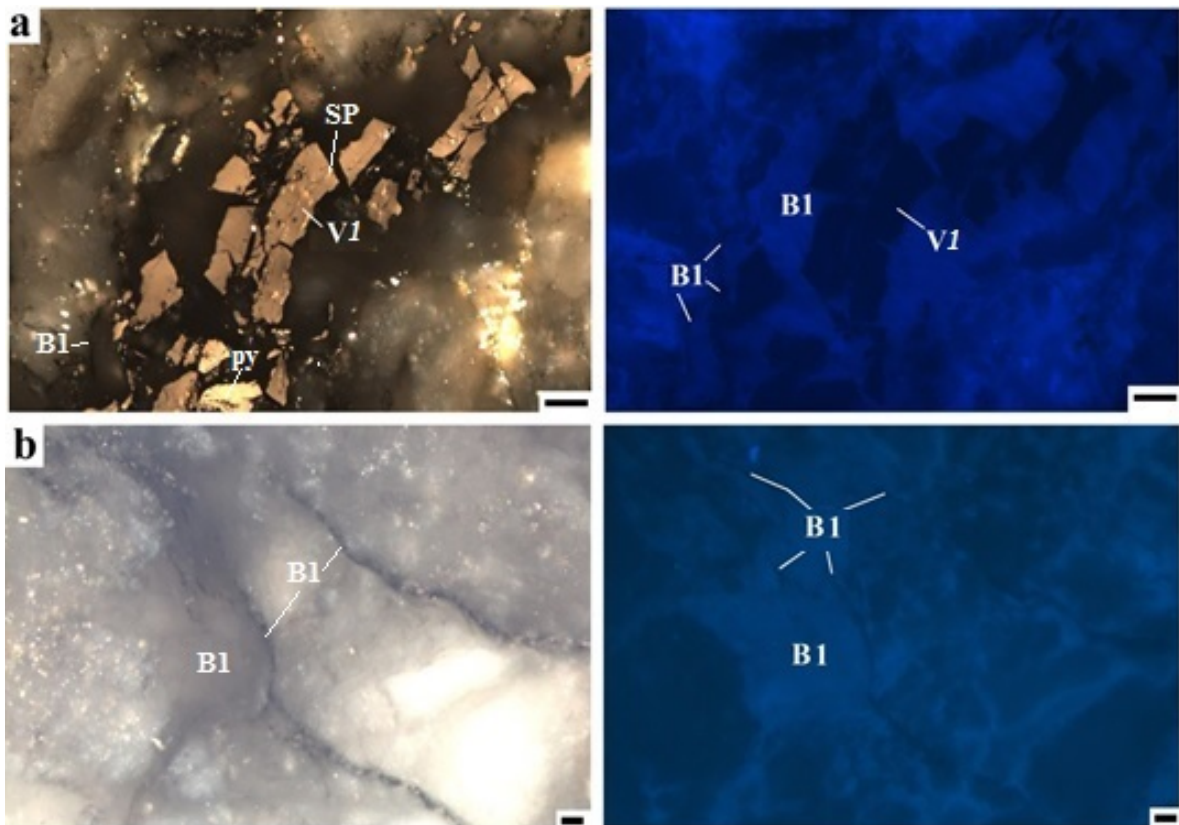


Figure 29 Photomicrographs of fractured reworked, (a) angular vitrinite (V1) particles with sporinite (SP) and dark brown solid bitumen (B1) filling in hydrothermal quartz veins and pyrite py (in oil immersion, normal reflected light and right is ultraviolet excitation) and filling in hydrothermal quartz veins: reworked vitrinite, V1 and pyrite (Bak 1 sample); (b) solid bitumen (B1) void fillings and diffuse appearance (Bak 2 sample).

Scale: 10 μm .

Associations of solid bitumen B1 and pyrobitumen PB with grains of reworked vitrinite, telinite and pyrite growth are shown in Figure 36 a and d. All DOM accompanying solid bitumen have no fluorescence intensity. The filamentous solid bitumen is infilled in very thin fractures and fissures of quartz grains with the rare presence of telinitre and reworked vitrinite. At the same time, pyrobitumen is frequently associated with filamentous solid bitumen and vitrinites. The small vitrinite particles associated with solid butimen occur as angular grains disseminate in the bitumen. In vitrinite, pyrite growths in framboidal and cubic crystal forms occur (Figure 36 d).

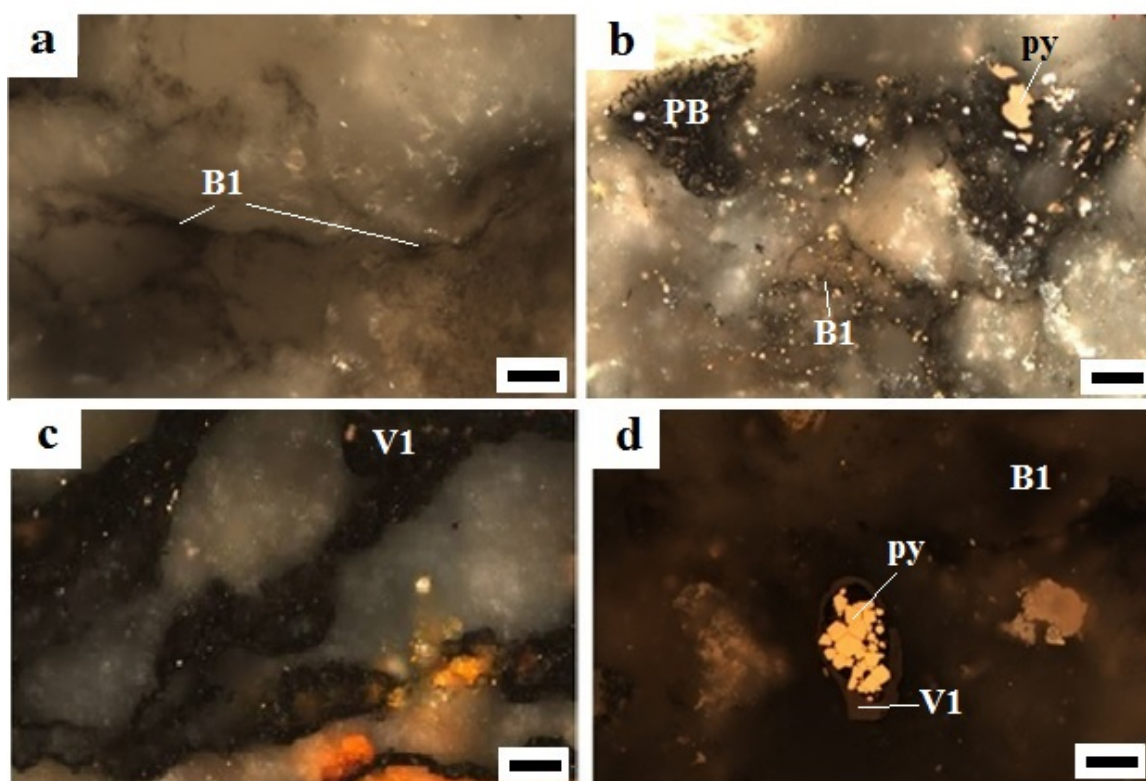


Figure 30 Photomicrographs of solid bitumen normal reflected light in oil immersion filling in hydrothermal quartz veins: a) very tiny filamentous and diffuse solid bitumen (B1) (sample Bak 2); b) filamentous and diffuse solid bitumen with pyrobitumen (sample Bak 1) and the pyrobitumen spongy feature at left indicates that asphaltene type solid bitumen could transform to pyrobitumen; c) vitrinite, telinite sample Bak 5); d) Egg like a humic type of vitrinite with the growth of euhedral pyrite crystals (py) in the middle and diffuse solid bitumen in the surrounding (sample Bak 1). Left: parallel polarised light in oil

immersion. Right: ultra-violet fluorescent excitation, uranium-containing fluid inclusion is visible. Scale: 10 μm .

5.2.2 Ore mineralogy

The ore microscopic observations show that the samples have ore mineral assemblages of arsenian pyrite and arsenopyrite, stibnite (antimonite), and valentinite (Figure 37 a and e; and Figure 38 a and c). Two morphologic varieties of arsenopyrite are recognised in mineralised rocks: acicular-prismatic and tabular forms. The pyrite textures appear in four forms, found under the microscope in several polished samples from the three specimens. The first textural type of pyrite is framboidal aggregate and very rare cubic pyrite; the size is more than 50 μm in the samples, appearing in sericitized carbonaceous siltstones. Another two forms are pentahedral and hexahedral pyrite crystals. Arsenopyrite always occurs in more quantities with pentahedral and hexahedral pyrite in all samples while with antimony ore minerals rarely occur and with small amounts as finely disseminated forms.

The arsenic sulphide ore minerals are closely associated with OM and are frequently presented, and the antimony minerals are rarely associated with OM and are in very small amounts. The arsenic pyrite was found in cubic and hexahedral textures with solid filamentous bitumens. At the same time, arsenopyrite minerals in the samples had a twin-tabular and acicular form with pyrobitumens (see Figure 37 a and b).

The antimony ore minerals are stibnite and valentinite, found in the open space of hydrothermal quartz veins in the form of overgrowths of fibrous textures (shown in Figure 37 c). Antimony ore minerals are radially fibrous crystal aggregates filling voids or massive, fine-grained aggregates. Native gold was not detected in samples under optical microscopy.

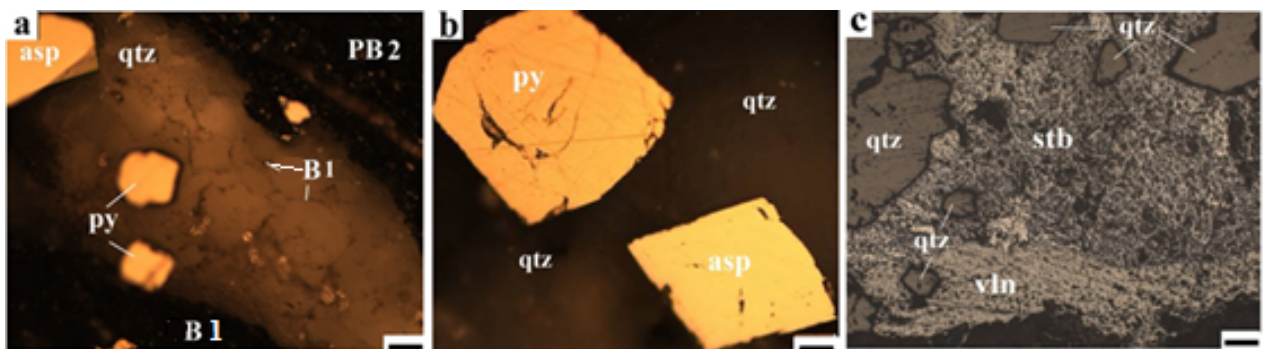


Figure 31 Photomicrographs of ore microscopy: a) cubic pyrite (py), acicular

arsenopyrite (asp) and solid bitumen (B1) occurring within hydrothermal quartz veins (Bak 2.3 sample); b) hexahedral pyrite (py) and tabular arsenopyrite (asp) in quartz veins (qtz) (Bak 2.2 sample); c) stibnite and antimonite into quartz veins (qtz) (Bak 2.4 sample).

Scale: 10 μm .

5.2.3 Mineralogical and chemical composition

XRPD values show muscovite (average 10.5 wt%), albite (average 5 wt%), illite (with low-grade smectite, general average 17 wt%), hydrothermal carbonate minerals (ankerite and siderite, general average 16 wt%), and hydrothermal quartz (average 25.1 wt%) in samples and paragenetically associate with the arsenic sulphide ore minerals, antimony minerals, and amorphous matter (Table 12).

The arsenic sulphide ore minerals were found mostly in the three samples of the second group; they always occur along the veins of hydrothermal quartz. Arsenian pyrite varies between 1.5 wt% and 32.7 wt% (average 7.7 wt%), while arsenopyrite varies between 1.5 wt% and 12.5 wt% (average 4.2 wt%). The antimony minerals have values between 3.9 wt% and 7.7 wt% (average 6.5 wt%), found only in three samples of the third samples group, related to the upper surface zone of mineralisation. Sulphide ore minerals of the whole rock samples consisted of elements As (up to 35%), Sb (up to 137%), Fe (up to 29.8%), Cu (up to 55 ppm), Zn (up to 218) and Pb (up to 1304). Maximum arsenic content is up to 35% in the second sample group, and the lowest value is 346 ppm in the third group of samples. At the same time, the antimony shows the highest value, up to 137%, in the third group of samples (shown in Table 12).

5.2.4 Electron microscopic observation of OM and ore minerals

Microprobe analysis was carried out for reworked vitrinite grains as inclusions of diagenetic pyrite crystals. The vein types of pyrobitumen were not detected in the technique because they have very fine microtextures; other authors also mentioned the detection limit problem (Belin, 1994) and (Cardott, et al., 2007). Pyrite growing over the reworked vitrinite appears in globular framboids, or sometimes polyframboids were found only in the first group of samples. The framboidal pyrite is of sedimentary-digenetic origin with a diameter of 2-50 micron, showing no presence of arsenic (Figure 39). The reworked vitrinite contains more than 90 wt% carbon element and oxygen of 4-6 wt%.

Moreover, the reworked vitrinite has a relatively higher S content, between 0.78 wt% and 1.27 wt% P (0.15-0.19) and Cl (0.09-0.12 wt%). Fe is detected as 0.23 wt%, while Ti varies between 1.19- 2.77 wt% in some samples.

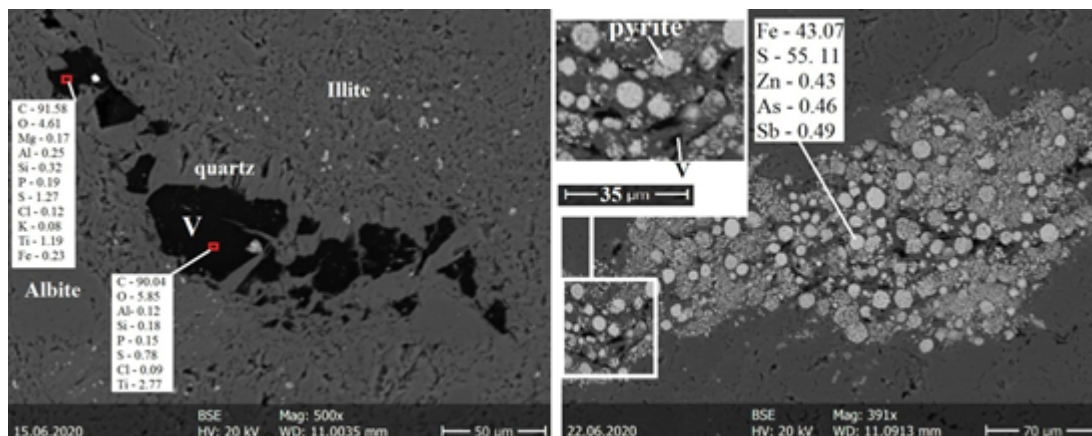


Figure 32 BSE images showing the chemical composition of vitrinite (V) and growths of frambooidal pyrites on the vitrinite (unit wt%).

Si is detected up to 0.32 wt% and Al is up to 0.25 wt%, with minor amounts of K and Mg in the range of 0.08-0.17 wt% present in OM. The minor amounts of Si, Al, K and Mg are most likely present in the reworked vitrinite due to the vicinity of the rock-bearing minerals.

Frambooidal pyrites occur up to 8 µm in reworked vitrinite grains, where they are enriched in Zn up to 0.43 wt%, As to 0.46 wt% and Sb to 0.49 wt% in some samples.

Additionally, using EMPA-EDS, 66 points were analyzed on the surfaces of individual arsenic sulphide crystals in polished sections to detect gold and arsenic elements. The measurement of the analytical points on grains of individual and combination crystal grains are shown in Figure 40 from a to h, and their elemental concentrations on average are indicated in Table 13. The EDS results show varying chemical concentrations within different morphogenetic shapes and sizes. Cubic and hexahedral shapes of pyrite were found in the samples of the second group, and they are of hydrothermal origin with 0.15-0.5 mm in size. Arsenic was found in the cubic pyrite between 0.97-3.68 wt% (average 3.0 wt%) and 2.7-4.86 wt% (average 3.81 wt%) in the hexahedral pyrite. Gold was not detected in the these pyrite grains (Table 13).

Arsenopyrite crystal has twin-tabular and acicular forms in the second group of samples. The average size of the twin-tabular arsenopyrite crystal is 0.2 mm, and the

acicular crystal is between 0.6-1 mm in length and about 75 microns in width. Arsenopyrite of both textures has an apparent arsenic content between 44.41-48.39 w% (average 46.7 wt%) and has no gold inclusions.

Table 7 Elemental concentration (on average wt%) in textures of arsenic sulphide ore minerals of samples Bak 1; Bak 2, and Bol

Shapes of minerals	Elements			Shapes of minerals	Elements		
	S	Fe	As		S	Fe	As
Acicular-prismatic arsenopyrite	22.12	31.29	46.60	Pentahedral pyrite	54.41	42.54	3.06
Tabular arsenopyrite	22.18	30.40	46.85	Hexahedral pyrite	53.20	43.13	3.81
Combination of acicular-prismatic arsenopyrite and pentahedral pyrite	54.11	43.55	2.33	Cubic pyrite	53.21	43.75	3.05

Antimony content is measured at over 80 wt% in valentinite and less than 73 wt % in stibnite; these minerals have no arsenic content, gold and other elemental inclusions.

5.2.5 X-ray maps of OM for carbon and sulphur

EMPA X-ray map shows that sulphur cover reworked vitrinite grains (Figure 41 a and c). The OM has about 90 wt% carbon with 1.27 wt% sulphur. Several light white spots on the reworked vitrinite show growths of individual sulphide crystals of sphalerite and pyrite on the map. The reworked vitrinite includes framboidal pyrite up to 5 µm in size,

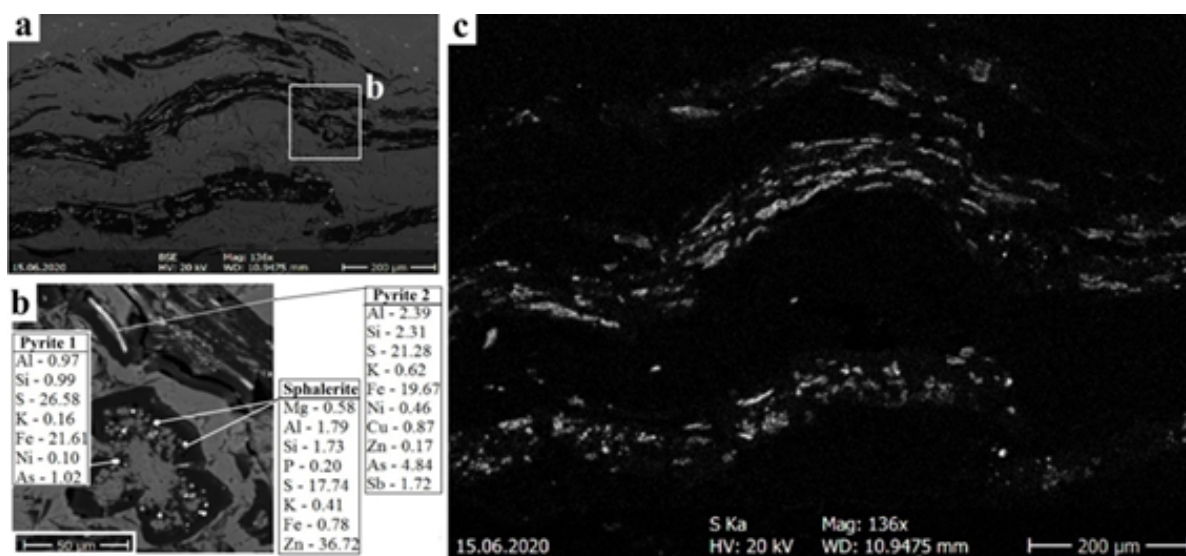


Figure 33 EMPA-EDS X-Ray map for vitrinite: BSE image (a) and EDS

measurements; (b) sulphur mapping image in thin-walled fly ash,
an inertinite particle (c) (unit wt%).

containing relatively lower amounts of arsenic (1.02 wt%), and the absent elements of copper, zinc, and antimony present in the acicular form, and crystal-shaped pyrite with a size of 30 μm . The vitrinite also occurs in intergrowths with tiny globular sphalerite grains, 3-5 μm in size (Figure 41 b), which have similar phosphorus content in the composition but do not contain chlorine.

5.2.6 Thermal maturity and reflectance

The results of micro-Raman spectroscopy for two types of solid bitumen, the vitrinite, and inertinite macerals, additionally, the kerogen was focused on the first-order region, which associated with two bands (D and G) between 1350 – 1600 cm^{-1} , and on the second region being associated with up to three bands (S) between 2600 – 3500 cm^{-1} , following the studies of (Jehlicka, et al., 2003) and (Kouketsu, et al., 2014). The Raman results indicate pyrobitumen with bituminous structure in the samples, which can be correlated with the structural evolution of bitumen from Zbecno (Czech Republic) and Karelia (Russia) in the study of (Jehlicka, et al., 2003). The Raman measurements concentrate on three parameters; the position of peaks, intensity, and full width at half maximum (FWHM), which is based on the Kouketsu's (Kouketsu, et al., 2014) equation, see Equation 1 below:

$$T (\text{°C}) = - 2.15(\text{FWHM}-\text{D1})+478 \quad (1)$$

where T = estimated temperature; FWHM = full width at half maximum; D1 = a peak of Raman spectra.

The equation is used to estimate the thermal maturity of carbonaceous matter, because it is applicable and accurate in 200-400°C (Kouketsu, et al., 2014).. The quantitative Raman measurement shows that multiple spot analyses of different areas in the samples of three types of carbonaceous matter and kerogen provided similar spectra (“n” means the numbers of spectra), showing relatively intensive bands of D (1331-1338 cm^{-1}) and G (1600-1604 cm^{-1}), while D3 (1500 cm^{-1}) and D4 (1180 cm^{-1}) are quite weak bands in the first-order region, and S bands (between 2600-3300 cm^{-1}) have a relatively low

intensity in the second-order region. The three types of carbonaceous matters and kerogen are described separately below (shown in Figure 42 and Table 14):

Kerogen is characterized by a low intensity wide (up to 118.6 cm⁻¹ FWHM) D1 band at around 1332.9 ± 8.7 cm⁻¹ (n = 5), and a relatively high intensity narrow (up to 68.46 cm⁻¹ FWHM) D2 band at 1601.0 ± 11.57 cm⁻¹ (n = 5). In the second-order region, the major peaks occur at wavenumbers of 2867.06 cm⁻¹ (S1), 2914.31 cm⁻¹ (S2) and 3065.69 cm⁻¹ (S3).

Vitrinite (V1) is characterized by a low intensity wide (up to 117.64 cm⁻¹ FWHM) D1 band at around 1331.6 ± 9.6 cm⁻¹ (n = 10) and a relatively high intensity narrow (up to 58.82 cm⁻¹ FWHM) D2 band at 1603.9 ± 6.75 cm⁻¹ (n = 10). In the second-order region, the major peaks occur at wavenumbers of 2655.9 cm⁻¹ (S1), 2913.35 cm⁻¹ (S2), and 3219.87 cm⁻¹ (S3).

The solid bitumen (B1) has a high intensity wide D1 peak (up to 109.92 cm⁻¹ FWHM) at wave-number of 1337.8 ± 22.2 cm⁻¹ (n = 5) and a low intensity, narrow D2 peak (up to 58.81 cm⁻¹ FWHM) at wavenumber of 1601.0 ± 7.7 cm⁻¹ (n = 5) in the first region and the S peaks at wavenumbers of 2607.46 cm⁻¹ (S1), 2922.98 cm⁻¹ (S2) and 3191.1 cm⁻¹ (S3) (n = 5) in the second region.

The pyrobitumen (PB) exhibits a high intensity, relatively wide (up to 93.53 cm⁻¹) D1 peak at around 1338.7 ± 12.54 cm⁻¹ (n = 5), while a low intensity, narrow (up to 49.18 cm⁻¹) D2 peak at around 1602.9 ± 5.8 cm⁻¹ (n = 5) occurs in the first region. In the second region, the pyrobitumen has a weak S1-peak at around 2655.9 cm⁻¹ (S1), and two weak overtones at 2992.41 cm⁻¹ (S2) and 3203.58 cm⁻¹ (S3) are present.

The reflectance of pyrobitumen was determined by laser Raman characteristic peaks (peak height) using Liu's (Liu, et al., 2013) equation, which is equivalent to vitrinite reflectance that can reflect different maturation grades and the surface optical properties of samples (Liu, et al., 2013), see Equation 2 below:

$$\text{RmcRo \%} = 1.1659 \text{ h (Dh/Gh)} + 2.7588 \quad (2)$$

where RmcRo% refers to the Raman reflectance using Raman parameters; h(Dh/Gh) refers to the Raman peak height ratio (Dh refers to the peak height D, Gh refers to the peak height G).

The equation is more applicable for pyrobitumen (highly matured hydrocarbon with mineral inclusion) in an ore deposit (Liu, et al., 2013); (Yuguang, et al., 2017), which

corresponds to our case. The samples' equivalent reflectivity of three pyrobitumen and kerogen were calculated, the maturity parameters indicated in Table 14.

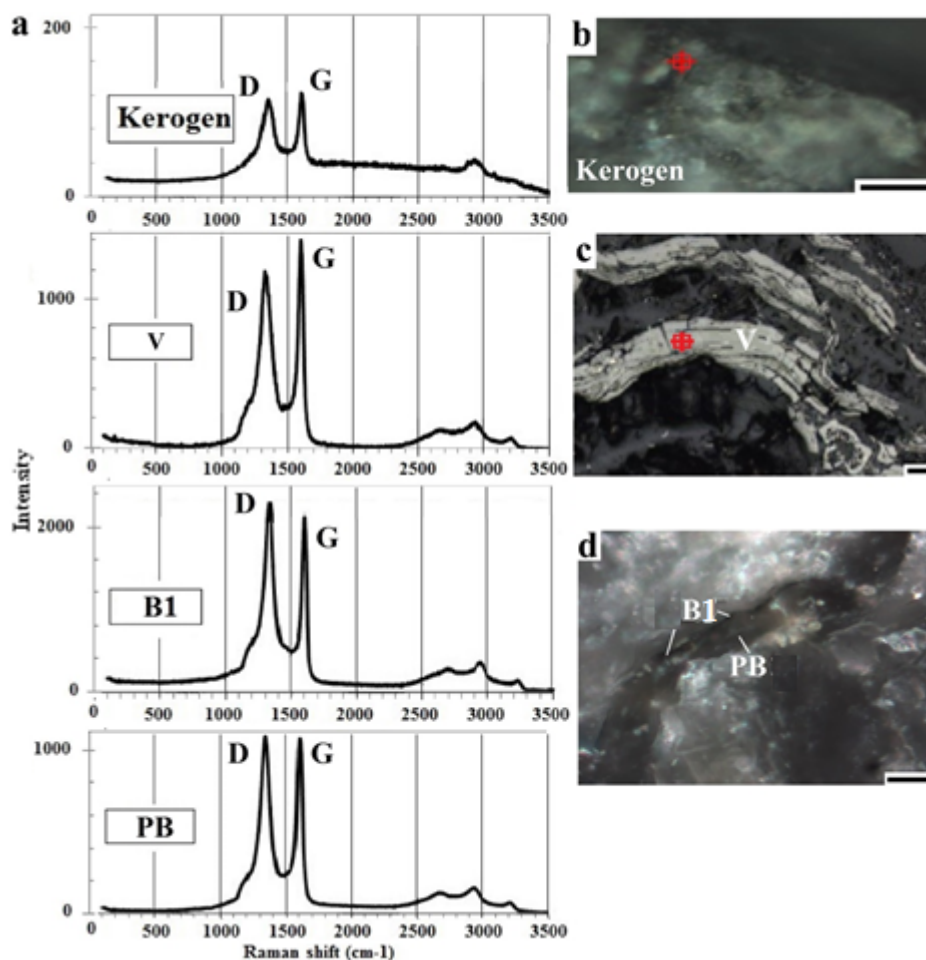


Figure 34 Raman microscopy measurement of reworked vitrinite (V), two types of pyrobitumen (PB) and kerogen with Raman spectra (a) of D and G peaks, and optical photomicrographs under cross-polarized light (b – kerogen, c – vitrinite, and d – B1 and PB). Scale: 10 μm .

Table 8 Relevant parameters of the Raman spectra of selected samples (Bak 1, Bak 2, Bak 2.4, Bak 2.5) for estimated temperatures and estimated organic maturity.

OM	RP	P (cm^{-1})	FWHM (cm^{-1})	PH	G_i/D_i ratio	D_h/G_h ratio	R_{mcR_o} %	$T^\circ\text{C}$ (± 30)
Kr	G	1601.0	56.88	158	1.032	0.968	3.88	231.3
	D	1332.9	114.74	153				
V	G	1603.9	55.92	1420	1.163	0.859	3.76	235.5
	D	1331.6	112.81	1220				
B1	G	1601.0	54.96	1165	0.978	1.021	3.94	254.1

	D	1337.8	104.14	1190				
PB	G	1602.9	49.18	2200	0.956	1.045	3.97	276.9
	D	1338.7	93.53	2300				

Abbreviation: OM is organic matter; Kr is kerogen; VI is vitrinite; PB is pyrobitumen and BI is solid bitumen; RP is Raman peak; P is Position; FWHM is full width at half maximum; PH is Peak height; Gi/Di is intensity ratio; Dh/Gh is peak height ratio; RmcRo% is Raman reflectance calculated using Raman parameters expressed in equivalent to vitrinite reflectance; T is Temperature.

5.2.7 Total organic content (TOC) and organic elemental (H, N, S) analysis

The total organic carbon (TOC %) was measured in carbonate-free samples using an organic elemental analyser after treatment with 10 % hydrochloric acid at room temperature and 60°C for 20-30 minutes in a water bath. The TOC was found in various samples ranging from 0.31 wt% to 0.47 wt% (0.36 wt%) in three groups of samples. The lowest TOC content was found in the sample Bak 2.25, which is 0.31 wt%, and no TOC was found in the Bol and Bak 2.4 samples from the third group, which is related to the antimony sulphide ore zone (near-surface post-ore mineralisation). The average TOC value ranges from 0.33 wt% to 0.38 wt% in three samples (Bak 2.2, Bak 2.3 and Bak 2.1) of the second group related to the arsenic sulphide ore zone (the main ore mineralisation). In contrast, the first group of the three samples (Bak 2, Bak 1 and Bak 2.5), belonging to the zone rich in the carbonaceous matter (pre-ore mineralisation), shows the highest TOC content from 0.32 wt% to 0.47 wt% (see in Table 15).

Table 9 Total organic carbon (TOC %) H, N and S of nine whole-rock samples.

Samples	Bak 2	Bak 1	Bak 2.5	Bak 2.2	Bak 2.3	Bak 2.1	Bol	Bak 2.4	Bak 2.25
TOC	0.34	0.33	0.38	0.47	0.43	0.32	-	-	0.31
H	0.43	0.21	0.32	0.09	0.51	0.19	-	0.10	0.14
N	0.21	0.19	0.22	0.26	0.24	0.10	-	0.15	0.17
S	1.17	1.15	1.23	2.1	1.97	1.14	1.12	1.34	1.24

The organic elemental analyser determined the OM's, H, N, and S content. Hydrogen contents range from 0.09 wt % to 0.43 wt% (average 0.26 wt %), while the nitrogen content varies from 0.15 wt % to 0.26 wt % (average 0.21 wt%) in the samples. Total sulphur content varies from 1.12 wt % to 2.1 wt %, and the average value is 1.61 wt%.

5.2.8 Functional group composition and soluble OM analysis

The composition of OM was determined using FTIR spectra (Figure 43): a broad peak at 3375 cm⁻¹ has stretching vibrations of hydroxyl (O-H) groups (very small

amount), and methylene groups appear like antisymmetric stretching the peak at 2932 cm^{-1} and stretching the peak at 2854 cm^{-1} , respectively. The peaks at 1632 cm^{-1} , 1525 cm^{-1} , 1497 cm^{-1} and 1282 cm^{-1} correspond to characteristic vibrations from aromatic rings, which are characterised by polycyclic aromatic hydrocarbon. The stretching vibration of C-O for carbonyl groups is absent in the samples. The characteristic vibrations of the aromatic rings of the phenolic hydroxyl group at 1632 cm^{-1} , 1523 cm^{-1} , 1499 cm^{-1} and 1282 cm^{-1} , and the similar characteristic peaks of vibrations reflect the studied OM shows stretching vibrations similar to the phenolic hydroxyl group at 2854 cm^{-1} and 2931 cm^{-1} and is practically similar to the broad peak of the phenolic hydroxyl group at 1436 cm^{-1} . However, the carbonyl area of the phenolic hydroxyl group peak at 1733 cm^{-1} , where it is absent in the composition of the studied OM. During a decarboxylation process, the carbonyl group could be missed in the studied OM. Other functional groups of the OM composition and structure correspond to the phenolic hydroxyl group characteristic of the lignin material.

The extractable fraction and the volume of the soluble OM were very small and not fractionated further.

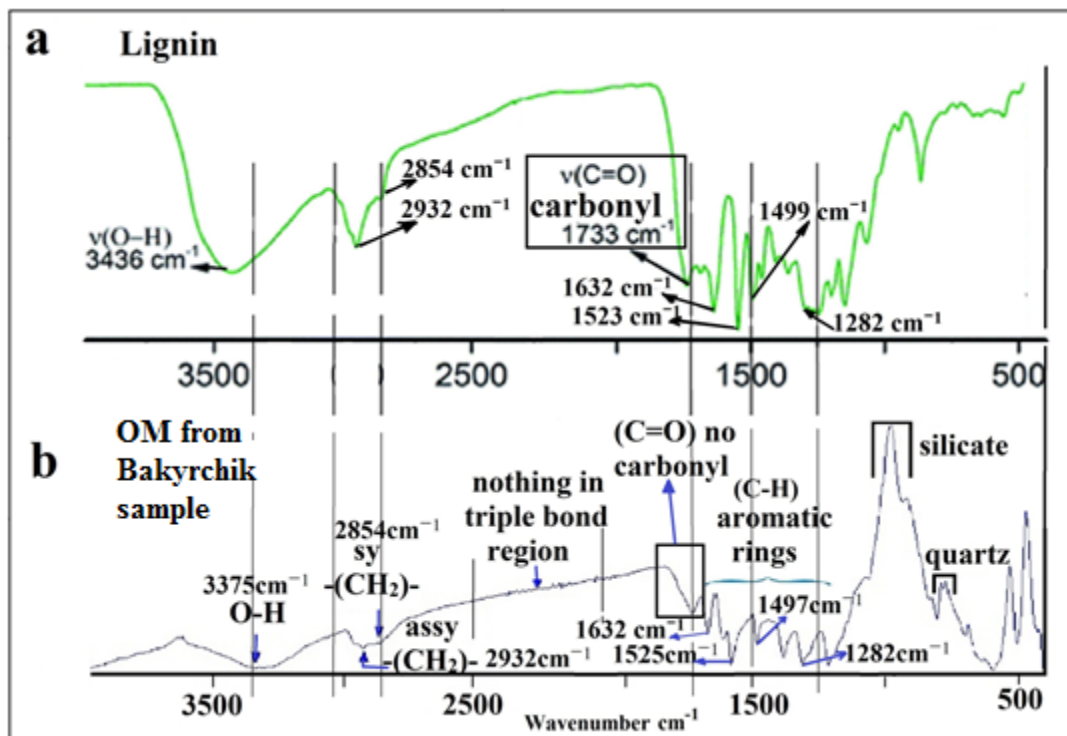


Figure 35. FTIR analysis and comparison of organic fractions: (a) molecular structure of lignin with silica nanocomposites (modified from (Weizhen, et al., 2017)); (b) OM with rock matrices from the rock samples (no carbonyl is indicated in the frame).

5.2.9 Experimental results

The optical and electron microscope techniques did not confirm the presence of native gold grains in the three types of pyrobitumen and even in the arsenic sulphide minerals. Moreover, besides gold, the organic fraction contains other precious metals, too. This confirms that gold and other precious metals are very finely dispersed within the organic matrix.

Gold content accompanied with other metals (Ag, Pt and Pd) extracted by the sequential extraction from two different phases, soluble organic fractions of solid bitumen and arsenic sulphide minerals from nine samples were measured by ICP-OES; see Table 16.

In the first stage of sequential extraction, the solvent of hydroxyl ammonium chloride started to extract a higher amount of As (up to 3608 ppm), Fe (up to 8297 ppm) and S (up to 8450 ppm); most likely, the dissolution of arsenian pyrite was removed with a precious metal content of gold (between 0.01 ppm and 0.13 ppm), Ag (up to 1.4 ppm) and Pt (up to 230 ppb).

The amounts of dissolved precious metals in the nine samples exceeded the first stage in the second stage. This solvent was strong enough to oxidise organic materials removing major amounts of precious metals: gold (7.23 ppm), Ag (3.8 ppm) and Pt (31 ppb) and Pd (26 ppb). Additionally, the presence of other elements in the extracts was found, such as As (up to 138 ppm), Fe (up to 3989 ppm) and S (up to 132 ppm) and at this stage.

In the last third stage, the most powerful aqua regia solvent completely dissolved all remaining precious metals from arsenopyrite and some remains of pyrite, and even non-recoverable metals from the first stage. This stage shows the highest values for As (4050 ppm), Fe (14285 ppm), S (10246 ppm), and the highest grade of Au (10 ppm), Ag (33 ppm) and Pt (263 ppb) were dissolved by the aqua regia solvent, most likely, from the arsenopyrite minerals (see in Table 16).

The XRPD shows that one may affirm that in the first stage, the hydroxyl ammonium chloride had no completely digestive effects on all sulphide-ore minerals, especially arsenopyrite, which were dissolved partly, following base-metal sulphide and

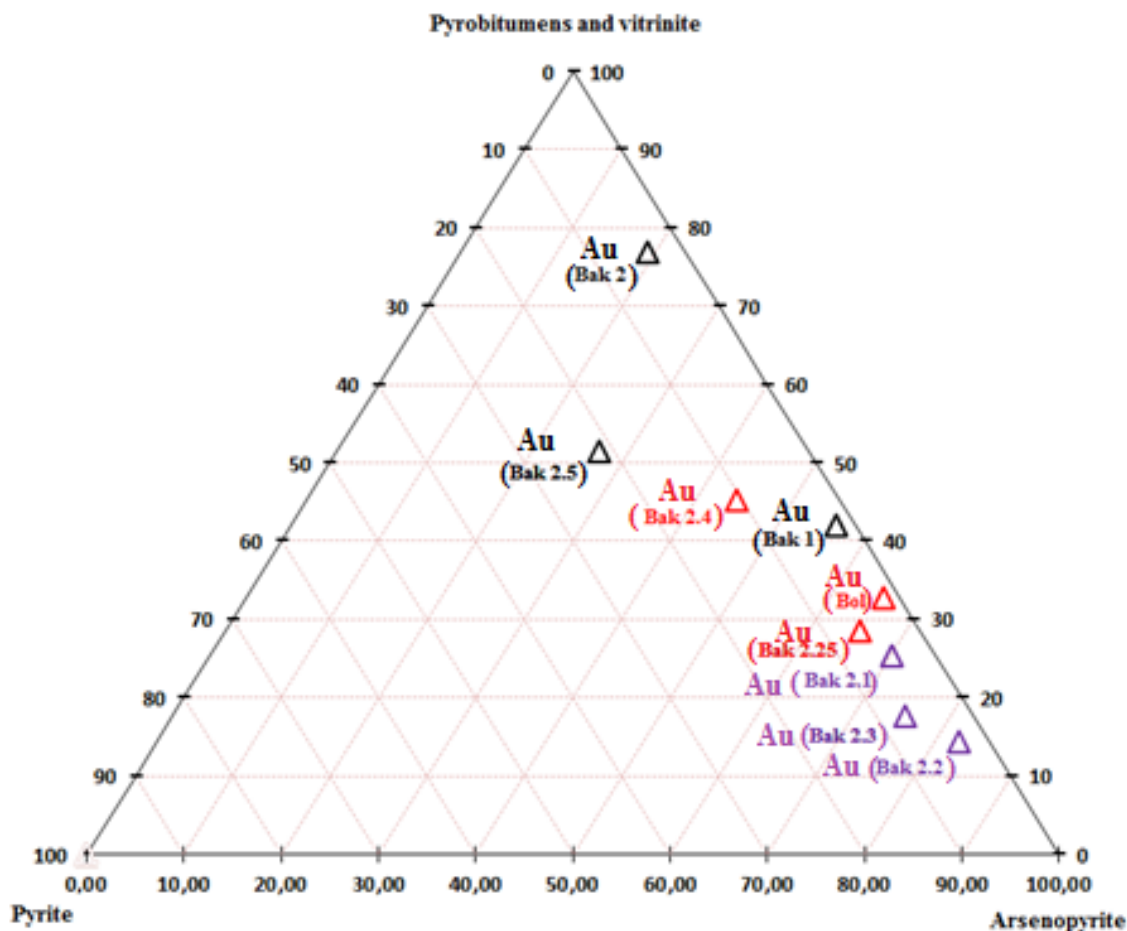


Figure 36 Triangular diagram of the gold in pyrobitumens, vitrinite, Arsenopyrite, and pyrite ratio in three sample groups of a total of nine samples (Denoted by colour: black for group I; violet for group II, red for group III, and samples in the brackets).

antimony-sulphide minerals. Moreover, it was detected that no-dissolving silicate minerals (quartz, mica, feldspar and illite almost in all samples) and oxide minerals (rutile, and etc.) were not dissolved by acids in the two stages of the experiment. Still, all sulphide-ore minerals were dissolved completely in the second stage due to the aqua regia acid. Nevertheless, the XRPD confirms that each chemical element has corresponding phases in the three stages, with decreasing or completely lost phases of amorphous and sulphide mineral matters during acid digestion.

The three groups of the nine samples have gold, Ag, Pt and Pd contents with different values in OM and arsenic sulphide ore minerals. The total gold content is higher in sulphide minerals (11 ppm) than in pyrobitumen (7 ppm) (described below in detail). The total Pt value includes (490 ppb) appearing more in sulphide minerals than in pyrobitumen (31 ppb), while the Pd value found in pyrobitumen alone totals up to 26 ppb.

According to the ratio of gold to pyrobitumen and arsenic sulphide ore minerals, in a triangular diagram (Figure 44), it can be seen that the gold content decreases from arsenopyrite (6 times more) and pyrobitumen (3 times more) to pyrite in the nine samples from three groups (Junussov, et al., 2021). Samples show that the arsenopyrite mineral is more enriched in gold, especially in the samples from the second group, which corresponds to the main ore mineralisation (Junussov, et al., 2018a); (Junussov & Umarbekova, 2018b) and (Junussov, et al., 2018c). Solid bitumen comprises gold from three groups of samples, mainly from samples of the second group. The lowest content of gold is observed in pyrite; gold of pyrite includes mostly in the second group of samples (Junussov, 2018a); (Junussov, 2018c); (Junussov M., 2018d).

Samples of group I:

Bak 2 sample contains a relatively high gold content (2 ppm) in pyrobitumen, and low gold content in arsenopyrite (0.5) and pyrite (0.1 ppm). The ratio of gold in pyrobitumen is relatively higher (77 %).

Bak1 sample contains an average gold content (3 ppm) in pyrobitumen and higher gold content in arsenopyrite (4 ppm), and a low gold content (0.13 ppm) in pyrite. The highest gold ratio in this sample has arsenopyrite (56%).

Bak 2.5 has a higher content of gold (0.21 ppm) in pyrobitumen than in arsenopyrite (0.11 ppm) and pyrite (0.09 ppm). The 52 % gold ratio has the sample of pyrobitumen.

Samples group II:

Bak 2.3 contains an average gold content (0.19 ppm) in pyrobitumen. Arsenopyrite has a high content of gold (0.81 ppm), while pyrite has a low content of gold (0.08 ppm) in this sample. The arsenopyrite has a relatively higher gold ratio (75 %) than others in the sample.

Bak 2.2 has an average gold content (0.22 ppm) in pyrobitumen, high gold content (1.26 ppm) in arsenopyrite and low content of gold in pyrite (0.05 ppm). The arsenopyrite to gold in this sample ratio is 83%.

Bak 2.1 includes an average content of gold value in pyrobitumen (0.76 ppm); in arsenopyrite, it is higher (2.1 ppm), while in pyrite, it is low (0.13 ppm). Arsenopyrite has a 71% gold ratio in the sample.

Samples group III:

The Bol sample is enriched with the gold of pyrobitumen on average (0.2 ppm), arsenopyrite has a higher value (0.4 ppm), and pyrite has a lower content (0.01 ppm). The gold to arsenopyrite in this sample ratio is 65%.

Bak 2.4 varies in different values of gold content in different phases: it has high gold (0.44 ppm) in pyrobitumen and almost similar content of gold (0.43 ppm) in arsenopyrite, while the gold content (0.10 ppm) in pyrite is low. Almost the same ratio of gold (44 - 45%) has both pyrobitumen and arsenopyrite in the sample.

Bak 2.25 sample has an average gold content in pyrobitumen (0.21 ppm); in arsenopyrite, it is high (0.48), while in pyrite, the content of gold is low (0.05 ppm). The sample has a higher gold ratio (65 %) related to arsenopyrite.

According to the ratio of gold to pyrobitumen and arsenic sulphide ore minerals in a triangular diagram, it can be seen that the gold content increases from arsenopyrite (6 times more) and pyrobitumen (3times more) to pyrite in nine samples from three groups. Three samples show that the arsenopyrite mineral is more enriched in gold, especially from the second group of three samples, which corresponding to the main ore mineralisation. Solid bitumen comprises gold from three groups of samples, mainly from samples of the second group. The lowest content of gold is observed in pyrite of three groups; gold of pyrite includes mostly in the second group of samples.

The results of the ratio of gold to the organic phase and ore sulphide phase indicate that the second group of samples from the main ore mineralisation zone is more relevant and promising.

5.2.10 LA-ICP-MS

A total of 50 LA-ICP-MS spot analyses were conducted on the OM and arsenic sulphide minerals. In the case of OM, it was hard to find the relevant grain size (Figure 45) of OM. Most OM is found in inaccessable sizes with tiny veins or small-sized filamentous forms. Nevertheless, most of the spots contained measurable quantities of gold and silver. The dataset shows that gold concentrations are relatively uniform among the samples. Most samples' OM composed of gold distribution patterns are relatively weak smooth with a few spikes, while the arsenic sulphide grains show many spiky depth-concentration for Au and Ag. The OM and arsenic sulphide minerals analyses have been shown in Figure 46 and Figure 47.

As (Cook, et al., 2009); (Sung, et al., 2009) and (Gao, et al., 2019) mentioned that smooth spectra indicate a presence of nano- to submicron-sized inclusions of native gold, while wavy or spiky spectra mean that gold occurs primarily as a solid solution in a lattice of mineral matter or as homogeneously distributed nanoparticles.

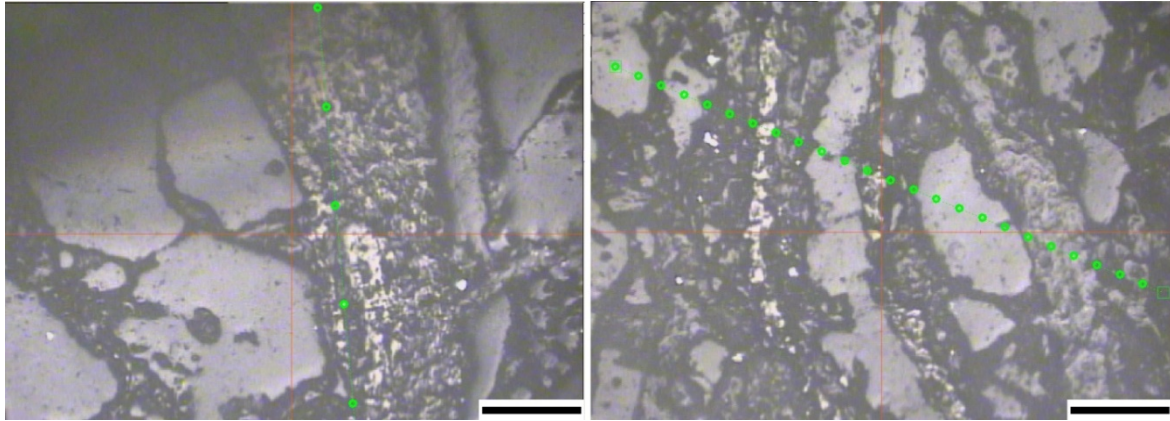


Figure 37 LA-ICP-MS images of spot analyses on grains of OM (light grey).

Scale 100 μm .

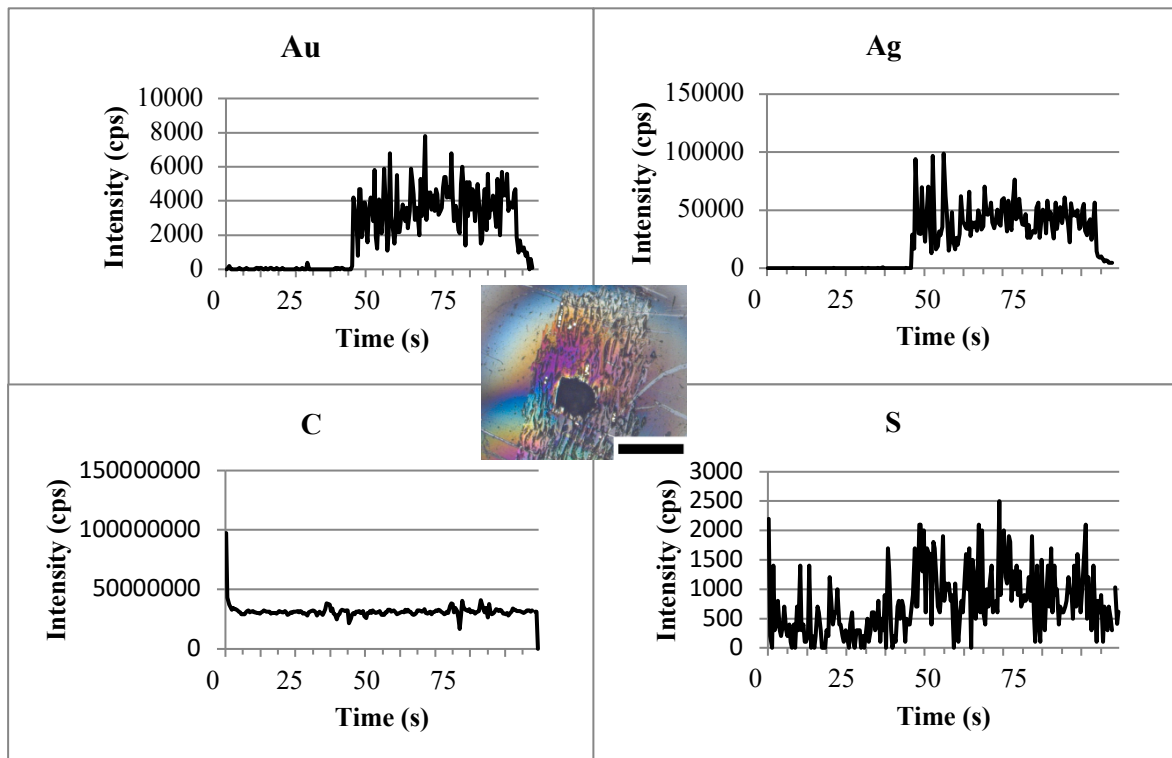


Figure 38 Representative time-resolved LA-ICP-MS depth profiles for Au, Ag, C and S along a linear track through grains of OM in the sample of Bak 2.4.

(Scale is 100 μm in the photomicrograph).

The LA-ICP-MS line spot analyses on the OM grains (Figure 46) show good signals of Au and Ag and good signals of S, but the absence of signals of carbon content.

The LA-ICP-MS spot analyses on the grains of OM show Au and Ag's presence, ranging from 19 ppm (Bak 2.4) to 250 ppm (Bak 2 and Bak 2.5) in the OM, relatively but having no carbon signals.

Line profiles from the host into arsenopyrite crystals show the presence of good signals of Au, Ag, and Pt counts within the arsenopyrite, with more signals in the core of the mineral crystal (Figure 47).

The results of LA-ICP-MS spot analyses confirm the presence of Au, Ag and Pt elements in OM and the crystal mineral with results of ICP-OES.

6. Discussion

6.1 W-Mecsek: geological occurrence and genetic model

6.1.1 Source of OM and Au

The type of the dispersed OM (DOM) according to the vitrinites (with the trace of wood tissues) and the solid bitumen types confirmed by FTIR results indicate the humic acid origin of the terrestrial OM in the fluvial environment. Geochemical results show that the OM has the presence of sulphur-rich polycyclic hetero-aromatic hydrocarbon, the TOC content ranges from 0.5% to 1.1%, and high thermal maturity up to 2.2 (Ro).

Au is occurred with various grades in OM of the Permian-Early Triassic Sandstones in the W-Mecsek Mountains, in the same area of the Permian KSF with high uranium content (Kádas, 1983); (Barabás & Konrád, 2000); and (Barabás, 2010). (Szalay, 1954); and (Barabás, 2010) described that the uranium is sourced from the granite of the Mórágý complex. Gold is most likely sourced also from the granite complex accompanied by uranium. The organic-rich sequences are enriched in gold by surface and groundwater or hydrothermal leaching of the underlying and denudation surface of the granitoid complex.

6.1.2 Generation and maturation of OM

The high-rank maturation of the DOM shows the semi-anthracite to anthracite stage, the presence of highly reflecting homogenous pyrobitumen and the higher reflectivity of sporinite in the reworked vitrinite particles. Telinite is relatively frequent in

the lower zone from 847.6 m while the small size angular vitrodetrinite is abundant in WH2-072, WH2-076 and WH2-077 in the coarser arcosis siltstone part of the samples. In the DOM, a part of solid bitumen is thermally altered. (Jacob, 1989) defined pyrobitumen as a high-temperature product formed from solid bitumen, a highly aromatic and insoluble bituminous substance (Glikson, et al., 2000); (Huc, et al., 2000) with higher than $R_o\% > 2\%$). Usually, it has no fluorescence or is weak (brown, wavelength > 650 nm) (Glikson, et al., 2000) and is generally related to magmatic activity and hydrothermal fluid convection (Simoneit, 1994), (Simoneit, 2000), (Simoneit, 2018). The flow texture migration patterns of dark brown solid bitumen and pyrobitumen and the presence of uranium ore accumulation in the vicinity of the texture of vitrinite and pyrobitumen particles with gold and other sulphide minerals confirm the occurrence of epigenetic hydrothermal conventions. Radiation influence on the vitrinite is obvious when cracking edges show lower reflectance rims and desiccation patterns on the bigger telinite grains. The vitrinite reflectance is higher than the non-altered telinite. The most altered telinite reflectance of $20 \mu\text{m}$ to $50 \mu\text{m}$ particles has the lowest value among the studied samples, with $1.787 R_o\%$ in the WH2-076 sample where the pyrobitumen frequently occurred with dark brown solid bitumen together, which probably penetrated the small vitrinite grains in the siltstone. This sample shows the high greenish fluorescence intensity of the mineral matrix in the vicinity of bitumens, which may also explain the lowering of the reflectivity of vitrinite. Contrary, the highest vitrinite reflectance was measured in WH2-070 with $2.381 R_o\%$ where the vitrinite was a dominant maceral. (Rojkovic, et al., 1992) described the hydrothermal alteration of the DOM, where the Permian OM is affected by radioactive α decay during the U mineralisation. Moreover, very similar alterations of the OM are described in the works of (Eakin & Gize, 1992), (Sýkorová, et al., 2016), and (Machovič, et al., 2021) in uranium deposits where they indicated i.e. increased thermal maturity, aromatisation, and decreased H/C atomic ratio. Hydrothermal deposits of gold and base metals are described by (Parnel, et al., 1993). Nevertheless, we suggest that the DOM thermal alteration result from hydrothermal alteration and radioactive decay in our case. Desiccation patterns of vitrinite grain cracks and the porous texture of telinite with lower reflectivity fields in the particle indicate the effect of α decay; however, radiation-induced haloes in the DOM are seldom. Other evidence of the radioactive alteration is that vitrinite reflectance minimum and maximum values are widely ganging in samples WH2-57 and WH2-72 from 1.600% to 2.897% and from 1.720% to 2.988% vitrinite reflectance, respectively. This can also be connected to the radiation effect of uranium ore minerals. The hydrothermal effect is

confirmed by the (1) presence of pyrobitumen associated with gold in the DOM, (2) enrichments of sulphur and chlorine contents in the DOM (3); and the transformation of the framboidal pyrite crystal growth in the vitrinite to recrystallised cement pyrite with arsenic content (4).

The solid bitumen B1 most likely migrated by hydrothermal fluids from the high-temperature zone to the low-temperatures towards the host rock's larger voids, bringing together metal-organic complexes and gold. Raman thermal maturity measurement shows that the maturity of thin veined homogenous pyrobitumen (PB) is 1.62% (RmcRo), and the estimated migration temperature reaches a relatively higher temperature of $144.5 \pm 30^\circ\text{C}$. In comparison, it is closely associated with non-fluorescing bitumen B1 has a thermal maturity of 1.37% (RmcRo) with an estimated temperature of $129.7 \pm 30^\circ\text{C}$. The PB is migrated through very thin fractures and voids of the dolomite and between quartz grains of the host rock. PB is retained as the tiny thin-filling forms within the dolomite and quartz veins showing no-fluorescence intensity; however, in pore fillings, the homogenous character is obvious. The occurrence of the thin membrane adhering to mineral grains explains that the bitumen was precipitated as the immiscible phase of the hydrothermal fluid, and it flowed along the wall of veins due to its consistency transforming to this type of PB. According to the Raman measurement, the telinite, desmocollinite thermal maturity temperature is between the maximum temperatures of PB and B1. with $137 \pm 30^\circ\text{C}$ and 1.57% (RmcRo). The reworked vitrinite V1 is associated with solid bitumen B1 and a greenish fluorescing mineral matrix, where the estimated temperature is $104 \pm 30^\circ\text{C}$, corresponding to the thermal maturity of 1.0% (RmcRo%). The lowermost vitrinite reflectance value of WH2-076 is the closest to the average Raman corrected values. However, further investigation is necessary to explain the differences between the results of the two methods. In the case of WH2-76, the grain size was the smallest, below $50 \mu\text{m}$ and in the vicinity of grains, solid bitumen in diffuse and veinlet forms may lower the reflectivity to 1.787%.

The vitrinite in the form of big telinite, desmocollinite is relatively frequent in the lower zone with the small size angular vitrinite in the parts of the coarser arkosic siltstone in WH2-057, WH2-072 and WH2-076.

The big vitrinite particles of telinite and desmocollinite V1 often contain framboidal

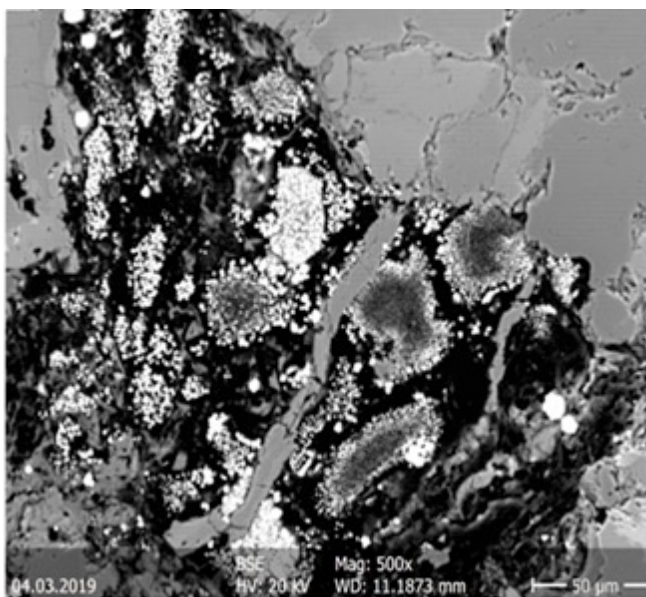


Figure 39 EMPA-BSE images of primary vitrinite

V1 showing framboidal pyrite growths of bacterial colonies comprising bacterial sulfate-reduction in the OM texture. Black – OM, dark grey – quartz, grey – dolomite, white grey – Fe-Mg carbonate, imaged from the sample WH2-073.

(Nayak, et al., 2008).

The vitrinite particles comprise carbon content of 86 wt%, total sulphur up to 5-6 wt% preserving as a sulphur-rich OM. The thiophenic compounds are thermally stable up to 250°C in hydrothermal fluids (Giordano, 2000). Our FTIR results confirm this. In our soluble OM samples, we observed a minor quantity of aliphatic hydrocarbons and a higher concentration of aromatics; moreover, the Raman indicates the absence of aliphatic hydrocarbon chains due to the absence of D4- and D5-bands (Ferralis, et al., 2016), which correlate well with the thermal maturity of samples. The detected chlorine in the primary autochthonous vitrinite indicates the presence of Cl-rich groundwater during early diagenesis (Caswell, et al., 1984a) and (Caswell, et al., 1984b). We compared the maturity of our studied samples with the Late Permian uranium ore deposit and the closest measured Early-Jurassic hard coals, which are 20 km distance to the East. Thermal maturity and rank of the Early Jurassic hard coals range from high volatile bituminous to middle volatile bituminous rank in the E-Mecsek Coal Basin, where the vitrinite reflectance is the highest

and polyframboidal early diagenetic pyrite. These pyrites are microbial in origin, Figure 48 showing that pyrite crystals grow from the edge to the core place of the pyritisation area. The origin of such framboidal pyrite in the OM has been described by Hámor (1994) as a result of early diagenesis of coalified plant tissues. (Berner, 1969) and (Raiswell, 1982:) have pointed out that pyrite is formed by the decomposing of the most readily metabolised, DOM through bacterial sulfate reduction. Pyrite formation occurs under various sedimentary microenvironments conditions (Hámor, 1994);

in the Pécsbánya mine in Pécs-Szabolcs area where the samples from 600 m to 800 m depth interval ranging from 1.36 % to 1.57 % (Laczó, 1983); (Pápay, 2018). In the E-Mecsek, the highest burial and heat flux was at the end of the Late Cretaceous with more than 100°C according to apatite and lower than 200°C for zircon fission-track data the Lower Jurassic tuff samples within the coal measures (Dunkl, 1992). The fission-track data and the Raman measurements with the estimated temperature ranges confirm that the temperature ranged between 100°C to 200°C maximum during the burial.

6.1.3 Migration and entrapment of OM and Au

Analytical results obtained by LA-ICP-MS for OM with high-grade gold and uranium concentrations explain that the metals are intimately associated with DOM, vitrinite and solid bitumen, implying that the DOM has played a role in the transport and trapping of the metals. Moreover, the results of LA-ICP-MS correlate well the total digestion of gold and silver followed by ICP-OES. A network of veins and veinlets filled with vitrinite and solid bitumen, and the occurrence of OM inclusions in detrital and authigenic quartz grains. It provides compelling evidence that the vitrinite and solid bitumen derived from a mobile (liquid hydrocarbon) precursor circulated of uranium, Au, Ag, Th, Ba, Cu, and Pb, are enriched relative to their concentrations in the organic-rich sediments. This is particularly the case for U and Au. The time-resolved LA-ICP-MS line scans show wavy peaks of gold and uranium concentrations. This suggests strongly that the metals are mainly present as a structurally bond or metal-organic complex.

The needle-like or veined uranium-titanium ore minerals within the OM and in the dolomite veins occur like subhedral uranium-phosphate ore minerals in fractured autochthonous vitrinite particle V1 matrix and between quartz grains. This suggests that uranium is paragenetically associated with solid bitumen. Moreover, rare earth element enriches within the V1 as a phosphate phase, finely dispersed monazite with high uranium content. The uranium ore mineralisation was investigated by (Barabás & Konrád, 2000); they indicated that the uranium mineralisation in the form of nasturan or pitchblende U_3O_8 forms up to 200°C hydrothermal temperatures, after leaching out and migrating with the subsurface waters from the uranium-bearing granite (Barabás & Konrád, 2000); (Barabás, 2013); (Barabás, 1988); and (Buda, 1990) evaluated that, on average, the uranium concentration of the supposed source-rock granite varies from 7 to 10 g/t and total REE from 52 ppm to 290 ppm.

The surface waters of the fluvial system and the redox conditions of the basement and subsurface groundwater flow changes with high plant remains accumulation were in favour of the precipitation of uranium and mainly associated with Cu, V, and Cr. The uranium is precipitated from waters percolating laterally and downwards (see Figure 49) The best conditions were present in abandoned channels, oxbows, ox-bow lakes, and swamps. In these parts, grey sediments enriched in the OM were deposited. In the central part of the basin, red sandstones were developed under oxidizing conditions. The commercial-grade uranium ore was formed between these zones in the green sandstone sequence. In some parts, the uranium was dissolved due to oxidation processes (Barabás, 1979). The dissolved uranium adsorbed on the surface or in the vicinity of the decomposing OM forming metal-organic colloids (Szalay, 1954). Hydrodynamics caused the uranium to entrap in reducing sediments; the uranium would be precipitated and gradually enriched, resulting in the formation of commercial concentrations of uranium (Barabás & Konrád, 2000). (Santbrd, 1994) and (Raffensperger & Garven, 1995) studies have supported that DOM's strong reductant and may protect the ore from oxidation and destruction. (Santbrd, 1994) and others assume that uranium concentrates in the vicinity of DOM accumulations by gravity-driven groundwater flow. Others (Raffensperger & Garven, 1995) describe large-scale thermal convection cells or thermal convection-initiated systems by releasing the accumulated heat through the fracture zones of radioactive granites (Fehn, et al., 1978).

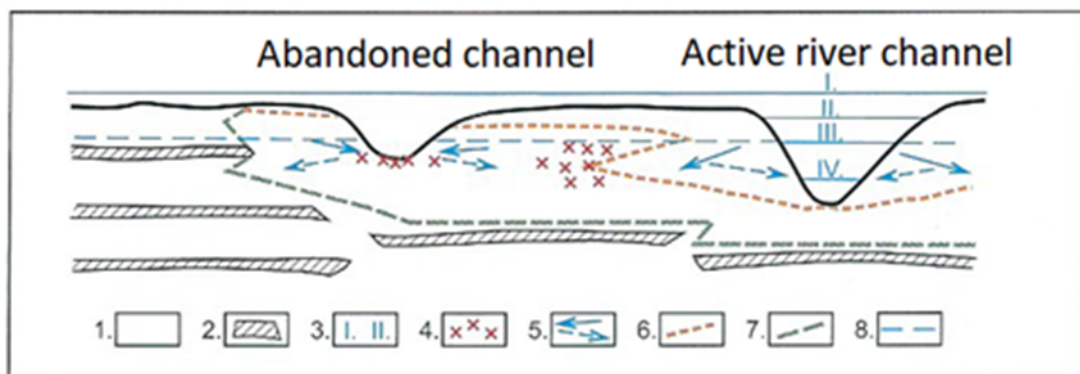


Figure 40 Primary syngenetic model of the accumulation of uranium ore deposit in W-Mecsek. (modified after (Barabás, 2013), and (Virág & Vincze, 1967)) Legend: 1) Fluvial floodplain sediment; 2) Peat-forming sediments; 3) Different groundwater tables; 4) Ore accumulation lenses; 5) Sub-surface water flow; 6) Oxydated and intermediate rock types; 7) Intermediate and reductive rocks border; 8) Mean groundwater level.

The electron microscopy results revealed that the fracture-filling needle-like uranium ore minerals in the dolomite veins were enriched in titanium. Other subhedral forms of the ore minerals are rich in phosphor and titanium and contain zinc in small quantities. The high concentration of the phosphor and titanium may explain that uranium ore minerals mobilised with elevated mineral matter-containing solutions and later precipitated together in the accumulation zone. The uranium accumulation of the Late Permian KSF is closely connected on the one hand to the primary weathering processes of the denudation surface of the Late Carboniferous magmatic rocks as a primary source of ore formation (Virágh & Vincze, 1967). The other origin is the epigenetic dissolution from the granitoid complex underlying the host rock (Barabás & Konrád, 2000). The uranium migrates in the surface and subsurface waters easily. The dissolved uranium precipitates when transported to a reductive environment or highly adsorbing materials like DOM, clay minerals, and iron oxides. The accumulation is usually the most intensive in the intermediate transition zone of the oxidising and reducing environment.

From the palaeogeography point of view, the semi-arid climate is favourable because the vegetation is not sparse; the environment is highly oxidative, while in the geomorphological depression zones in the watercourses and accumulation zones of valleys, the lush vegetation with elevated OM creates reductive conditions, which can adsorb the uranium.

In W-Mecsek, the sandstone type of uranium accumulation occurs where flat slopes ($< 5^\circ$) of alluvial rocks across fine-grained sandstone, clay, and siltstone lenses build up the sedimentary sequences, and the source of uranium derives from the vicinity of uranium-containing rocks. This type of Penn-accordance ore formation shows the impregnation of the rock matrix parallel to the bedding. It is associated with the OM's local accumulation anomalies in the fluvial sedimentation.

The W-Mecsek Late Paleozoic-Triassic sequence represents a per anticline structure where the strike is WSW-ENE, plunging 10° to 15° to eastwards. This explains why we can find the older Permian rocks in the south-western part of the anticline, and the younger sediments occur eastwards on the surface. The present inclination of beds on the wings of the anticline can reach up to 30° (Barabás, 2013).

The Mecsekalja tectonic zone delineates the W-Mecsek Permian sequences to the south due to left strike block siftings. These complicated tectonic movements explain that W-Mecsek Permian rocks were found 20 km distance eastwards from the uranium deposit in the Máriakéménd-Bári line in boreholes (Barabás, 2013).

The anticline structure turns to syncline towards Pécs, where Late Triassic alluvial sediments occur at the surface in the eastern part of the city. Here the Triassic - Jurassic sedimentation is more than 1000 m thick; boreholes have never penetrated the Permian uranium ore deposit but probably underlie the younger sequences (Barabás, 2013).

6.1.4 Geological model and genetic linkage of OM and Au

The results of sequential gold extraction of the OM indicate that the gold concentration increases with the higher OM carbon content in the presence of carbonate minerals. (Földessy, 1997) has confirmed that the gold is preferentially concentrated in organic-rich layers. The organic-rich sequences are enriched in gold by surface and groundwater or hydrothermal leaching of the underlying and denudation surface of the granitoid complex. The OM of the samples is enriched in gold, most likely as (Giordano, 1994) and (Wood, 1996) have revealed that OM can bind metals to aromatic acids; form colloidal phases absorbing metals from water solutions (Seredin & Finkelman, 2008). (Seredin, 2007) and (Seredin & Finkelman, 2008) have explained that the concentration of ionic gold in coal materials decreases with decreasing the absorption capacity of OM in groundwater solutions with increasing rank of coal, so the metal-organic complexes formation is expected to form during early diagenesis. According to this, the W-Mecsek gold accumulation suggests the finely dispersed gold mineralisation in the OM during bituminisation at above 144°C and in-depth between 830 m and 900 m. The gold mineralisation occurred most likely during the infiltration circulation of sulphur-rich groundwater, enriched in gold and silver and heated both by the radioactive decay of the uranium ores and increasing geothermal gradient related to the burial. The gold migrated with liquid bitumen in the ore-forming solutions in the sulphur-rich groundwater fluids and precipitated within dolomite minerals and intergranular quartz (Figure 50 b and c). The gold is bonded to the organic matrix with sulphur-rich heterocyclic aromatic hydrocarbon of the coaly type carbonaceous matter, probably as thiosulfate complexes, according to (Baruah, et al., 1998) (Figure 50 e-1).

Some findings of gold as a trace element in arsenic sulphide minerals (pyrite), closely associated with the gold-rich OM, show that the OM may favour the gold enrichment in the pyrite minerals, as (Nayak, et al., 2008) explained that pyrites have adsorbed gold during their precipitation as framboids bands and subsequent recrystallisation/ growth, where the gold has been captured from the OM and adsorbed into the structure of iron disulphides. (Vincze, 1987) indicated that a significant part of pyrite is

of biogenic origin in the zone with increasing OM, which has a framboidal form, due to the activity of desulphurising bacteria. (Yue, et al., 2020) explained that the framboidal pyrite had been transformed to cement-like pyrite under the addition of thermal fluids with abundant sulphur and iron; and to euhedral pyrite after evolving with the addition of low-temperature thermal fluids to the limited pore space during (late) diagenesis in the grey sandstone, what I could also confirm. The occurrence of arsenic Cu-rich sulfosalts (As 22%, Sb 1% and Cu 37.5%) crystal growths into pore space of the euhedral pyrites has been explained in the study by (Sawlowicz, 1993) that the trace element enrichments in the pores of the euhedral pyrites as a result of diagenetic recrystallisation during the transformation of framboids to euhedral pyrite (shown above in Figure 50 d), where silver and copper contents increase with decreasing gold. As (Földessy, 1997) indicated that the presence of OM and its enrichment of gold in the ore formation shows a high uranium value, but a high value of Cu indicates low grades of Au and U with high in Ag (up to 600 g/t, generally 50-150 g/t) (see in Figure 50 e-2).

Formation of gold within OM and arsenic sulphide ore minerals show in Figure 50 by the schematic model: where gold within OM and arsenic sulphide ore minerals in a reducing zone (three pyrite types and sulfosalt minerals) associated with uranium ore mineralisation indicating (a) migration of liquid bitumen (brown color) within grains of vitrinites (black color) by Au and U-rich (with other As, Sb, Cu, Fe, Mg and rare earth element) hydrothermal solution or groundwater (blue) compounds of dominated sulfate state under carbonate phase through pore spaces of quartz (grey) and potassium-feldspar grains (violet) with becoming dolomite veins; (b) precipitation of uranium ore minerals (dark grey) within primary autochthonous vitrinite (black) filling in veins of dolomite minerals (white color); (c) occurrence of solid bitumen and primary vitrinite compounds of colloidal gold deposited between quartz minerals grains after solidification processes; (d) growths of framboidal pyrites (yellow globular forms) on the grains of primary vitrinite evolving from the pyrite to euhedral pyrite and to cement pyrites during hydrothermal recrystallization, the euhedral pyrite between pores of potassium-feldspar grains (relatively rare quartz) inter-growing of finely dispersed sulfosalt minerals (orange color) into porous center of the pyrite; and (e) inclusions of noble metals as ionic and solid state in lattice structures of OM (as metal-organic compounds) (1), and arsenic-rich pyrite (as a very finely dispersed or invisible gold).

6.2 Bakyrchik: geological occurrence and genetic model

6.2.1 Source of OM and Au

The bulk ratios of OM's stable carbon isotope ratio. The second data indicates its biogenetic nature and organic source (Zairi, et al., 1987). Geochemical results, such as the presence of polycyclic (hetero) aromatic hydrocarbon and humic acid, indicate a terrestrial carbon source of lignin (TOC, 0.3-0.5%) in the lacustrine environment, which has allochthonous nature due to gravity flows (Azerbaev & Zhautikov, 2013). The sample's composition and source of kerogen (hardly distinguishable from pyrobitumen) partially confirm the terrestrial organic source, mainly from vascular plants, yielding an aromatic hydrocarbon (most likely the original coal source). The temperature of transformation of heating kerogen into liquid petroleum may occur at $231.3 \pm 30^\circ\text{C}$, which corresponds to its thermal maturity of Raman reflectance 3.88 % (RmcRo%) based on Raman results.

Gold is of a mantle source and occurs in ultramafic rocks from the mantle of the oceanic basement (Rafaylovich, 2009), which mainly occurred 300 Ma ago. The formation of gold is described by five geological ages: 574, 380, 300, 250 and 210 Ma, due to the isotopic analysis of Pb ($\text{Pb}/\text{U} > 50$) in gold-bearing sulphide ores (Lubecky, et al., 2008); (Umarbekova & Dyusembaeva, 2019). The first gold occurrence (574 Ma) is related to riftogenic stage of the Late Cambrian and Early Ordovician ($\text{€}_3\text{-O}_1$). The second mineralisation (380 Ma) is associated with the oceanic stage of the Early Devonian and Middle Devonian (D_{1-2}) with regression of the palaeo-ocean and formation of the volcanic island-arc stage in Late Devonian and Early Carboniferous ($\text{D}_{3\text{fm}}\text{-C}_{1\text{v}}$) above the subduction zone associated with basalt-andesitic complexes. The age of 300 Ma is related to an early collision with the intrusion of the Kunush gold-bearing intrusive complex at the Late Carboniferous and Late Permian age ($\text{C}_3\text{-P}_1$); it is a great granitic batholith and the source of the main gold generation. The final stage of gold occurrence ended between 250 and 210 Ma, the Middle Triassic and Late Triassic age (T_{2-3}), characterised by the regeneration of gold (Lubecky, et al., 2008).

6.2.2 Generation and maturation of OM and Au

Vitrinite at the anthracite stage shows that migration at $235.5 \pm 30^\circ\text{C}$ confirmed with thermal maturity of Raman reflectance 3.76% (RmcRo). This bituminous matter and, partially, vitrinite is most likely migrated by a hydrothermal system as angular-shaped forms from the high-temperature zone to the low-temperature zone through large voids in

the host rock. The large void filling of reworked vitrinite displays a medium to coarse-grain mosaic textures of particle assemblages in samples of Bak 1, Bak 2.1 and Bak 2.5.

The vitrinite coexisted within bacterial origin framboidal and needle-shaped diagenetic pyrite. The coexistence of framboidal sphalerite in the vitrinite grains is attributed to a diagenetic, epigenetic origin. The framboidal and needle-shaped textures of sulphide crystals have been observed growing from metal-enriched H₂S-bearing hydrothermal fluids, according to the concept of (Scott, et al., 2009) in a gold sulphide deposit. The needle-shaped pyrite and framboidal pyrite and sphalerite of vitrinite include minor elements As, Sb, Zn Cu and Ni (from pyrite) and P (from sphalerite), while the reworked vitrinite enriched in S, Cl and P.

Vitrinite and other vitrinite particles contain 90 wt% carbon and 2 wt% organic sulphur and other elements (P and Cl) preserved as sulphur-rich vitrinite. (Dai, et al., 2015) indicated that organic sulphur is generated from hydrothermal solutions during the coalification, ranging from about 0.1% to 4-12% levels (Dai, et al., 2020). Organic sulphur is a thiophenic sulphur compound, more abundant in bituminous coal and anthracite than in low-rank coals (Chou , 2012). The content of thiophenic sulphur increases with maturation (Ho, et al., 1974) in bitumen with a high content of aromatic hydrocarbons, resins and asphaltenes (Tissot & Welte, 1984), thermostable up to 250°C in hydrothermal fluids (Giordano, 2000). (Hwang, et al., 1998) indicated that the formation of sulphur-rich pyrobitumen results from the subsequent thermal change in asphaltic-rich bitumen in the presence of sulphur species. Moreover, (Powell, 1984) confirmed that the interaction of bitumen with the thermochemical reduction of sulfate should be responsible for the formation of some sulphur-rich bitumens.

Chlorine is present in OM, as (Caswell, et al., 1984a) and (Caswell, et al., 1984b) described that chlorine is more likely taken from Cl-rich groundwater during diagenesis. (Chou, et al., 1992) found that, under reducing conditions, chlorine, in the form of HCl, is released at temperatures between 250°C and 600°C, with a maximum release at 445°C. (Finkelman , 1980) and (Black, 1981) believed that phosphorus in most OMs is likely to be present in phosphates, where phosphorus is organic rather than a mineral fraction.

Dark solid bitumen (B1) migrates at a temperature of 254°C, and its thermal maturity is 3.94% (R_{mcRo}). It migrates through narrow fractures and voids within hydrothermal quartz in the host rock. It is retained as tiny narrow-filling forms within the hydrothermal quartz, showing a weak fluorescence intensity. The occurrence of a thin membrane adhered to the wall rocks may explain that the bitumen precipitated as an

immiscible phase with the hydrothermal fluid and slowly flowed along the wall of veins due to its consistent transformation into this type of pyrobitumen.

Pyrobitumen (PB) migrated at a relatively higher temperature of $276.9 \pm 30^\circ\text{C}$, with thermal maturity 3.97% (RmcRo), and it migrated within the hydrothermal fluid to the low-temperature zone through narrow fissures; it is entrapped in the relatively narrow voids of the hydrothermal quartz.

The two sizes of veins of solid bitumens in quartz may explain that they were displaced and trapped within different temperatures and became different chemical compositions during the distillation process, as cooling the hydrothermal fluid can cause differentiation in the chemical composition of the bitumen. The final freezing point of the mixture and the molecule size, which can migrate through the neck diameter, controls this process.

Solid bitumen and vitrinite are polymerising to increase aromatic compounds losing aliphatic hydrocarbon during the migration within the hot hydrothermal fluid. This aromatic hydrocarbon-enriched bitumen is trapped by decreasing the fluid temperature in quartz in the lower temperature zone as a filler in voids of the quartz matrix. Thus, the heavy component of the bitumen is trapped within hydrothermal quartz, pyrolysed and converted to solid bitumen as a result of thermally altered primary bitumen, which was driven off the soluble hydrocarbon products and volatile organic components of N, H, CH₄ CO₂ (Zairi, et al., 1987), retained in the insoluble carbon-rich residues. The stable carbon isotope ratio of the solid bitumen and vitrinite ranges from $\delta^{13}\text{C}$ -22 ‰ to = -26,8 ‰, respectively, which confirms that it has a terrigenous origin (Zairi, et al., 1987).

6.2.3 Migration and entrapment of OM and Au

Rafailovich (2009) has considered the transportation and precipitation of gold in the Bakyrchik deposit through three processes (1) In the sedimentary-diagenetic process, gold was transported by a bisulfite gold and deposited in the shallow zone and underwater deltas, rich in OM and hydrogen sulphide, framboidal pyrite precipitated on rhythmically layered gold-bearing carbonaceous sediments. (2) In the tectonic-metasomatic process, gold was transported in a mineralised solution as a chloric complex of gold and precipitated in carbonaceous-terrigenous sediments, while framboidal pyrite recrystallised into gold-bearing pyrite of cubic and pentagon-dodecahedral forms with inclusions of arsenic. (3) In the intrusive-thermal-metasomatic process, syngenetic gold was remobilised

along the Qyzyl shear zone in the areas of intrusions and dikes of the Kunush granitic complex. Then gold reached the final precipitations with pyrobitumen.

6.2.4 Geological model and genetic linkage of OM and Au

The gold mineralisation of the deposit occurs in the Qyzyl shear zone (Lubecky, et al., 2008). (Zhu, et al., 2011) considered that the gold mineralisation in most shear zones results from post-peak metamorphism and is associated with a multi-stage alteration event.

Current and previous analytical and experimental data may explain the role of pyrobitumen in the Bakyrchik gold deposit by separating the three geological processes of gold mineralisation, which, most likely, correspond to regional maturations of the three pyrobitumen types:

1) Syngenetic gold accumulates in the sedimentary-diagenetic process with an increasing precursor asphaltic-rich hydrocarbon at low temperature in a slightly alkaline environment with the penetration of hydrogen sulphide-rich hydrothermal fluids into clay or silty lacustrine sediments of the Middle-Late Carboniferous formation. The bisulfite gold is transported by hydrothermal fluid. The fluid mobilises asphaltic-rich bituminous materials through large voids of mineral grains of the host rock in the high-temperature zone. (Simoneit, 2018) mentioned that a hydrothermal ore fluid could rapidly generate bituminous material from immature OM to fully matured products in host rocks. Ore fluid partly destroys the OM with increased aromatic hydrocarbon content (polycyclic compound) and loss of aliphatic carbon content. The thermogenic products are rapidly removed from the hot zone through voids (Simoneit, 1994). The low-temperature hydrothermal water may contribute to the thermochemical origin of framboidal pyrites in asphaltic-rich carbonaceous materials. The palaeotemperature was up to $235\pm 30^{\circ}\text{C}$, shown by the thermal maturation of vitrinite (V1).

2) The tectonic-metasomatic process results from the Qyzyl deep fault zone of 2 km length in the diagonal direction, the controlling structure of gold mineralisation in the carbonaceous-siltstone sequence. Gold is transported in a chloric state phase into the hydrothermal fluid with the presence of liquid bituminous material. The first arsenian pyrite with invisible gold content develops with the recrystallisation of framboidal pyrite (Rafaylovich, 2009). The bituminous material is removed from the high-temperature alteration of texture, filling very thin voids of mineral grains of the host rock at a temperature of $254\pm 30^{\circ}\text{C}$, forming very thin veined solid pyrobitumen (PB). The bitumen

in thin veins may be explained because bitumen is transported as an immiscible phase with the ore-forming fluid.

3) In the intrusive-thermal-metasomatic process, we are concerned with intrusions and dikes from the Kunush granitic complex at a depth of 4 km (Lubecky, et al., 2008) along the Qyzyl shear zone, and the main gold mineralisation belongs to sulphide ore zones. Gold mineralisation of the deposit occurs in sulphide ore zones with the presence of carbonaceous matter. The Qyzyl fault zone was where gold and pyrobitumen were concentrated in arsenic-sulphide minerals accompanied by ore-forming hydrothermal fluid upwards through the fault (see Figure 51).

Studies of fluid-inclusions of quartz from the ore zone showed that the main gold mineralisation zone takes place at 340°C and a pressure of 110-130 MPa with the formation of invisible gold-bearing arsenic sulphide minerals and by a decreasing in temperature to 200°C in gold mineralisation with the appearance of antimony minerals (Novojilov & Gavrilov, 1999). Pyrite and arsenopyrite predominate in the ore zone, while chalcopyrite and galena formed less frequently (Umarbekova, et al., 2017a) in relatively deep ones (Levitan, 2008). Pyrite occurs in invisible gold-containing cubic pyrite and gold-containing pentagon-dodecahedral forms in the circumstances of high temperature (Rafaylovich, et al., 2011). In the upper zone, arsenian pyrite predominates the arsenopyrite in the ratio of 3.5:1, while in the middle and lower zones, more arsenopyrite occurs with a ratio of 1:3 (Rafaylovich, et al., 2011). High Au concentration positively correlates with As-rich compositions in pyrite and arsenopyrite minerals (Rafaylovich et al., 2011). The content of As element is 0.005-0.6%, and the As in pyrite ranges from 1 to 1.5% (Rafaylovich, et al., 2011). Stibnite and valentinite are associated with native antimony (Levitan, 2008). The antimony content increases towards the near-surface area, and decreases in the deep zone (between 0.2% - 0.3%) (Volkov & Sidorov, 2017). The isotopic composition of the antimony sulphur shows relative values within the $\delta^{34}\text{S}$ of the interval from -3.8‰ to 2.5‰ (Kovalev, et al., 2014).

The sulphide ore minerals have a magmatic source: the S isotope analysis in sulphide ore minerals shows that $\delta^{34}\text{S}$ belongs to the felsic magmatic origin; the S becomes heavier with the increase in its depth from -4 to -6‰ in the depth of 0.5 km to 0.0‰ in the depth of 1.5 km (Rafaylovich, et al., 2011).

(Simon, et al., 1994) explained that Au and As are closely related in arsenian pyrite and arsenopyrite with a linear relationship: $\text{CAu} = 0.02 \text{ CAs} + 4 \times 10^{-5}$ (CAu and CAs represent the mole percentage of Au and As concentration, respectively). As-bearing pyrite

shows that a solid solution of gold has two coordination species: Au^0 and Au^+ (Simon, et al., 1994). Au^+ can occur in more than one form, including Au^+ in vacancies in an unknown Au-As-S complex (Simon, et al., 1994). Gold occurs in arsenic sulphide minerals as a solid solution and nano-inclusions in over-saturated conditions (Reich, et al., 2005). Solid solution gold (Au^+) enters As-bearing pyrite and arsenopyrite by replacing Fe^{2+} (Tarnocai, et al., 1997) extracts of a solid solution of Au^+ from the hydrothermal fluid by absorption (Zhu, et al., 2011).

In the hydrothermal vein system, bitumen can be enriched with the same metals that form ore minerals in the system (Parnell, 1988). The homogenisation temperature of gold mineralisation is 270°C on average (from 200°C to 340°C) (Novojilov & Gavrilov, 1999), which corresponds to the thermal maturation of narrow veined pyrobitumen (PB). The carbonaceous materials are formed everywhere in the ore zones and have maximum in the central part of the main ore zone (Rafaylovich, et al., 2011). As (Saxby, 1976) revealed, OM and metals dissolved in a hydrothermal fluid can be concentrated and precipitated by a reaction with suitable organic ligands as chemisorption into organic materials forming metal-organic compounds. Metal-complexing functional groups form in heterocyclic hydrocarbons containing nitrogen and sulphur (Saxby, 1976), concentrating mostly in the asphaltene fraction of bitumen (Giordano, 2000).

Gold was detected from the soluble part (in the hydrogen peroxide) of polycyclic aromatic fractions in pyrobitumen as a metal-organic compound and in arsenic sulphides (dissolved by the hydro ammonium chloride and aqua regia) as inclusions of “invisible gold”. The sequential extraction experiment shows no correlation between gold and organic carbon (C_{org}), while the arsenic content correlates positively with gold. In this case, there are two most likely reasons why it happens during the migration. First, the precursor of liquid bitumen undergoes the three different regional thermal influences. Gold of the functional groups in bitumen is partly removed due to the thermally stable and preserved gold content in different thermal zones. Secondly, the bitumen of gold complexes in the fluid migrates in a different direction through various voids lingering there due to molecular sizes of bitumen with different gold contents. Maybe this is one of the reasons why gold is partially removed from non-thermostable functional groups of bitumen in the hydrothermal system. Then the removed gold precipitates most likely in the structure of arsenic sulphide minerals.

Other authors indicate this, too; (Saxby, 1976) revealed that reducing of soluble Au^{1+} or Au^{3+} complexes to Au^0 by carbonaceous materials may account for some types of gold mineralisation.

(Jiuling L., et al., 1997) explained that organic compounds of gold have a strong ability to migrate with As and S upward together with metal-organic compounds. OM containing gold in hydrothermal ore fluid is thermally decomposed, removing gold from its organic ligand. Gold, together with the arsenic element, enters into the lattice of arsenopyrite and arsenian pyrite (Jiuling L., et al., 1997). Gold can form many compounds with organic ligands, especially those metal-organic compounds and atom cluster compounds containing S, P and Cl (Jiuling L., et al., 1997).

This explains that the precursor of liquid bitumen in the hydrothermal ore fluid mobilises gold as metal-organic compounds and, as a part of the organic fraction of gold, undergoes thermal decomposition, releasing dissolved gold and the rest of the preserved organic fraction that forms gold. When removed from OM, gold is chemically bound in arsenopyrite and arsenian pyrite structures, forming invisible gold. The remaining gold in organic functional groups forms gold-containing solid pyrobitumen as metal-organic compounds.

Formation of gold within OM and arsenic sulphide ore minerals shows in Figure 51 by the schematic model: where gold within OM and arsenic sulphide ore minerals in six active zones of the Bakyrchik gold deposit indicating a) penetration of the hot hydrothermal ore fluid (blue) into liquid bituminous materials (in coke zone, grey) through fissures and fractures in the host rock (white); b) migration of gold, bitumen (orange) and sulphide ore components (yellow) into hydrothermal fluid; c) entrapment of gold, bitumen and ore elements undergoing thermal and chemical influences for gold precipitation (in OM and ore minerals), and bitumen maturation (origin of V) vitrinite (black) and its thermochemical reduction for framboidal pyrite, and two veined solid bitumen and pyrobitumens (PB, PB1) with increasing thermal maturation and arsenic sulphide minerals occurrence (arsenian pyrite and arsenopyrite); d) gold inclusions in polycyclic aromatic hydrocarbons of pyrobitumens (orange) and vitrinite (black) as metal-organic compound (noble metals) and “invisible gold” in the arsenic structure lattice of arsenian pyrite and arsenopyrite (yellow).

6.3 Summary: Similarity and differences between W-Mecsek and Bakyrchik

The OM associated with gold mineralisation in both deposits is more likely related to the results of the global tectonic Variscan orogenic gold formation within organic-rich sedimentary basins in Central Europe (W-Mecsek) and Central Asia (Kazakhstan). More details of OM association with Au are shown in Table 17

OM is closely associated with ore mineralisation in both deposits of W-Mecsek and Bakyrchik. In a supergene environment of W-Mecsek and the hypogene environment of Bakyrchik, the OM's complexing, adsorption, and uptake of gold might be important processes that control the enrichment of the gold in the host rocks during sedimentation and diagenesis. Also, humic acids may be important transport agents in supergene/hypogene gold ore mineralisation. OM is unlikely to have played an important role in gold transportation in hydrothermal processes. However, organic acids produced by thermal maturation and decomposition of OM and colloidal, or molecular dissolution of hydrocarbon in fluid, might be significant for gold leaching and migration. The high-grade maturation of OM in the ores of both deposits relative to the thermally altered OM due to hot fluids. Finely disseminated OM of different thermally matured wood tissues and graphite particles in the upper area at the low-temperature zone and associated with gold enrichment shows that gold in OM occurs as detrital gold mineralisation. While the samples of Bakyrchik have plenty of hydrothermal quartz closely associated with veins and veinlets of OM enriched in the gold show that gold occurred as hydrothermal gold mineralisation. This evidence shows that OM in hot fluid solutions might have promoted Au migration. During the precipitation of gold, the light hydrocarbons that pre-existed in the anticline (W-Mecsek) and shear zone (Bakyrchik) might have contributed to the thermal reduction of sulfate and thus the pyritisation and gold precipitation.

Both deposits have extremely low extractable bitumen yield. Total organic carbon varies from 0.3 to 0.5 wt%, and the reflectance ranges from 3.7 to 3.9 % and sulphur content from 0.8 to 1.27 wt%. The sequentially extracted gold content from the organic matter of Western Mecsek reaches an average of 0.82 ppm gold. In comparison, the organic matter of Bakyrchik reaches an average of up to 0.80 ppm gold accompanied by an average of 0.96 ppm Ag, 10.3 ppb Pt and 13 ppb Pd (Junussov, 2018c); (Junussov, 2020a) and (Junussov, 2020b), see in Table 5-1.

Table 10 Similarity and differences between studied mineral deposits.

Geological settings	W-Mecsek	Bakyrchik
Similarity		
Au source	Magmatic intrusion	Magmatic intrusion

OM origin/source	Humic acid/terrestrial	Humic acid/terrestrial
OM composition	Heteroaromatic hydrocarbon	Heteroaromatic hydrocarbon
OM characteristics	Vitrinite / bitumen	Vitrinite / bitumen
OM texture	Dispersed, veins	Dispersed, veins
Kerogen type	III type	III type
OM rank grade	Anthracite stage	Anthracite stage
<i>Differences</i>		
TOC	1 %	0.5 %
Thermal maturation	2.2 %	3.76 %
Au grade in OM	Average 0.82 ppm	Average 0.80 ppm
Other noble metals in OM	Ag	Pt and Pd
OM association in ores	Uranium ore minerals	Sulphide ore minerals
Host rocks	Sandstone	Siltstone
Au mineralisation	Detrital	Hydrothermal

6.4 Further investigation works

Future research should include further investigation of these topics and continued experimental study of gold extraction from OM and gold measurement in graphite particles, metal-organic complexing and chelation, and rates of oxidative degradation of OM and metal release from adsorption sites.

7. Conclusions

According to the research data of the studies W-Mecsek uranium ore deposit and Bakyrchik gold-sulphide deposit, I report for the first time the forms and types of OM in both deposits and propose the primary genetic roles of OM in gold mineralisation and gold-bearing arsenic-rich pyrite formation of the following observational evidence: (1) The OM is terrigenous high plant origin at both locations, shows the carboxylic acid organic structure and sulphur-rich aromatic hydrocarbon composition; (2) The hypo-autochthonous dispersed OM dominantly occurs as vitrinite at both locations and in a smaller quantity liptinite and inertinite occur in the Mecsek samples. At both sites secondary macerals of homogeneous cement of pyrobitumen and brownish, non-fluorescing solid bitumen precipitated in the fractures and fine veins of the host rock; (3) Occurrence and local enrichments of gold in the OM were confirmed by sequential extraction method with ICP-OES and LA ICP-MS. Au in the OM is enriched in reducing zones in solid bitumen types and arsenian pyrite; (4) Hydrocarbon fluid migration processes played an important role in the sulphide and gold transportation because both the physically destructed vitrinite of Mecsek and secondary macerals of solid bitumen and pyrobitumen of the studied sites, gold was detectable in the OM. This study analytically confirms the occurrence and enrichment of gold in the pyrobitumen heteroaromatic fraction in the form of the metal-organic complex, which is entrapped in the micrometre size or smaller diameter veins and

voids of the host rock pores; (5) The OM had a crucial role in the entrapment, transportation, and preservation of the gold. The thermally stable organic fraction of solid bitumen like asphaltenes preserved a part of the gold. In contrast, the thermally unstable compounds of the organic fraction compounds may liberate some gold during cracking in the metagenesis. With the release of thermally unstable light molecule weighted migration products during the thermally driven decomposition and cracking of carboxyl and carbonyl group-containing compounds, the gold could be enriched in sulphide minerals with the recrystallisation of pyrite cement and euhedral crystals where gold enrichment is also confirmed. Reflected light and electron microscopic methods showed that the euhedral pyrite is enriched in silver in the presence of sulfosalts in its porous centre, which shows that in case the precipitating fluid became depleted in gold, silver was replaced within the sulphide mineral; (6) In the case of W-Mecsek, the dissolved uranium was transported as metal-organic complex during hydrothermal processes, and some places precipitated as needle-like uranium oxide in dolomite veins and at the same time formed dispersed subhedral uranium phosphate minerals in the clay matrix. The metal-organic-complex migration is confirmed by reflected light observation where the vicinity of the bitumen veins and vitrinite particles show medium greenish fluorescence of the mineral matrix at UV excitation; (7) In the case of Bakyrchik, the reductive OM agent is liberated gold above 270°C during the arsenic sulphide ore formation into arsenic lattice structure sulphide ore minerals with an arsenic lattice structure in the fracture zone; (8) Gold is preserved as a lattice gold or structurally bonded metal in the aromatic hydrocarbon fractions of the OM and arsenian pyrite of the deposits of W-Mecsek and Bakyrchik.

8. References

- Almássy, G., & Szalay, S. 1956: Analytical studies on vanadium and molybdenum content of Hungarian coals. *Mag. Tud. Akad. Kern. Tud. Oszt. Közl.*, 8, 39-45; *Fuel Abstr.*, 23, 2972.
- American Society for Testing and Materials (ASTM), 2014. D7708-11 Standard Test Method for Microscopical Determination of the Reflectance of Vitrinite Dispersed in Sedimentary Rocks. sec. 5, v. 05.06. In: *Annual Book of ASTM Standards: Petroleum Products, Lubricants, and Fossil Fuels; Gaseous Fuels; Coal and Coke*. ASTM International, West Conshohocken, PA, 10.
- Andreas, G., Andreas, I., & Victoria, K. 2003: Study of Low-Rank Greek Coals Using FT-IR Spectroscopy. *Energy sources*, 25, 995-1005.
- Arehart, G. B., Foland, K. A., Naeser, C. W., and Kestler, S. E. 1993. $^{40}\text{Ar}/^{39}\text{Ar}$, K/Ar, and fission track geochronology of sediment-hosted disseminated gold deposits at Post/Betze, Carlin Trend, northeastern Nevada. *Economic Geology*, 88: 622-646.
- Azerbaev, N.A., & Zhautikov, T.M. 2013: Lithology of carbonaceous-terrigenous complexes in the Bakyrchik strata. *VII Russian Lithological Congress 28-31 October 2013*. Novosibirsk. (in Russian)
- Árkai, P. 1991: Chlorite crystallinity: an empirical approach and correlation with illite crystallinity, coal rank and mineral facies as exemplified by Paleozoic and Mesozoic rocks of northeast Hungary. *J. Metamorph. Geol.*, 9: 723-734.
- Balachandran, M. 2014: Role of Infrared Spectroscopy in Coal Analysis—An Investigation. *American Journal of Analytical Chemistry*, 5, 367-372.
- Balla, Z. 1984: Kinematic analysis, the Carpathian loop and the Pannonian basin. *Geophys Transact* 30(4): 313–353
- Balogh, K., Kovách, Á. 1973: Determination of the age of the Battonya quartz-porphyrries by the Rb/Sr method.) *ATOMKI Közl* 15:243–249 In Hungarian with English abstract) basal point.) MÁFI, Budapest (in Hungarian).
- Barabás, A. 1979: Geological conditions of the Permian and tasks of surface geological investigations at the Mecsek ore deposit). *Föld Közl* 109(3–4):357–365 (in Hungarian with English abstract).
- Barabás, A. 1988: A Mórággyi-hegység DK-i előterének földtani felépítése és a harmadidőszaki képződmények értékelése uránprognosztikai szempontból (in Hungarian, translated title: Geological setting of the SE foreland of the Mórággy

- Range and evaluation of the Neogene sequences in terms of uranium prospects). — Kézirat (manuscript), Mecsekérc Adattára, Pécs, J–1319.
- Barabás A. & Konrád Gy. (eds.) 2000: Zárójelentés a magyarországi uránérc-kutatásról és a nyu-gat-mecseki uránérc-bányászatról. Kézirat, MECSEKÉRC Zrt. Földtani Adattár. (Final report of the uranium exploration of Hungary and W-Mecsek uranium ore mining. Manuscript in Hungarian)
- Barabás A, Barabás-Stuhl A. 2005: Geology of the Early Triassic Jakabhegy Sandstone Formation, Hungary, SE Transdanubia. *Acta Geol Hung* 48:1–47.
- Barabás, A., 2010. A délkeletdunántúli hidrogenetikus uránérctelepek földtani környezete és összehasonlító értékelésük. PTE, Manuscript, PhD thesis, 170.
- Barabás, A. 2013: Hasadó anyagok. (Pál-Molnár E. and Bíró L. eds.) In: Szilárd ásványi anyagok Magyarországon. (Fission mineral resources. Solid mineral resources of Hungary; in Hungarian), Geolitera publisher, SzTE TTIK Földrajzi és Földtani Tanszékcsoport, Szeged, 89-121.
- Barabás-Stuhl, Á. 1981: Microflora of the Permian and Early Triassic sediments of the Mecsek Mountains (South Hungary). *Acta Geol Hung* 24(1):49–97.
- Barker, C.E., & Pawlewicz, M.J. 1994: Calculation of vitrinite reflectance from thermal histories and peak temperatures. Book: In *Vitrinite Reflectance as a Maturity Parameter*; Mukhopadhyay, P. et al.; ACS Symposium Series; American Chemical Society: Washington, D.C, 1994.
- Baruah, M. K., Kotoky, P., & Borah, G. C. 1998: “Gold in High Sulphur Indian Coals,” *Fuel* 77 (15), 1867–1868.
- Baskakova, M.P. 1970: OM in gold-ore quartz veins in the Kyzyl-Kum sands. *Dokl Akad Nauk Uzb SSR* 27(12): 30-32 (in Russian)
- Beckett, P.H. 1989: The use of extractants in studies on trace metals in soils sewage sludges and sludge-treated soils. *Adv Soil Sci* 9: 143-176
- Belin, S. 1994: Backscattered electron imaging applied to source rock sedimentology: a comparison with conventional methods in organic petrology. *Bulletin Des Centres De Recherches Exploration-Production v. 18 Special Publication*: 165–187
- Benkő, I. & Szadeczky-Kardoss, G. 1957: Spectrographic determination of trace elements in coal ash. *Magy. Kern. Foly.*, 63, 78-84
- Berner, R. A. 1969: Migration of iron and sulphur within anaerobic sediments during early diagenesis. - *Am. J. Sci.*, 267, 19—42.

- Black, P.M. 1981: Taranaki coalfields: coal quality. *NZ Energy Res. Dev. Comm.* Publ. No. P5: 25
- Blakley, I, Cox, J. 2004: Competent Person's Report on the Kyzyl Project, Kazakhstan, for Polymetal International Plc, RPA UK Ltd. (2014), 302
- Bowell, R.J, Baumann, M., Gingrich, M., Tretbarb, D, Perkins, W.F., Fisher, P.C. 1999: The occurrence of gold at the Getchell mine, Nevada. *Journal of Geochemical Exploration*. Volume 67, Issues 1–3, 127-143.
- Bürg, G.H. 1930: Die Sichtbarmachung des feinverteilten Goldes in goldhöffigen Erzen und ihre wirtschaftliche Bedeutung. *Metall u Erz* 27: 333-338
- Bielowicz, B., Misiak, J. 2017. The forms of occurrence and geochemistry of sulphides in hard coal deposits of the Libiąż Beds in the Late Silesian Coal Basin, Southern Poland. *Geol. Geophys. Environ.* 43, 109–125
- Boucot, A.J., Xu, C., Scotese, C.R. & Morley, R.J. 2013: Phanerozoic Paleoclimate: An atlas of lithologic indicators of climate. *SEPM Concepts in Sedimentology and Paleontology* No. 11.
- Boyle, R.W. 1979: The geochemistry of gold and its deposits. *Geological Survey of Canada Bulletin*: 280-584
- Buda, Gy. 1981: Genesis of the Hungarian granitoid rocks. *Acta Geol Hung* 24(2–4):309–318
- Buda, Gy. 1990: REE in Hungarian and West-Carpathian Variscan granitoids. — The 15th General Meeting of the International Mineralogical Association, 1990, Beijing, China, Abstracts 2, pp. 982–984.
- Buda, Gy 1995: Correlation of Middle European Variscan granitoids. *Habil Thesis Eotvos Univ, Budapest* (in Hungarian) Burnet G., 1986: Newer technologies for resource recovery from coal combustion solid wastes. *Energy* 11, 1363–1375.
- Buda, Gy. 1996: Correlation of Variscan granitoids occurring in Central Europe. *A Min Petr Szeged Sup* 37: pp. 24.
- Buda, Gy., and Dobosi, G. 2004: Lamprophyre-derived high-K mafic enclaves in variscan granitoid from the Mecsek Mts. (South Hungary) — *Neues Jahrbuch für Mineralogie, Abhandlungen* 180 (2), pp. 115–147.
- Buslov, M.M., Saphonova, I.Y., Watanabe, T., 2001: Evolution of the Paleo-Asian Ocean (Altai–Sayan region, Central Asia) and collision of possible Gondwana-derived terranes with the southern marginal part of the Siberian continent. *Geosci. J.* 5, 203–224.

- Buslov, M.M., Watanabe, T., Smirnova, L.V., Fujiwara, I., Iwata, K., de Grave, J., Semakov, N.N., Travin, A.V., Kir'yanova, A.P., Kokh, D.A., 2003: Role of strike-slip faulting in Late Paleozoic–Early Mesozoic tectonics and geodynamics of the Altai-Sayan and East Kazakhstan regions. *Russ. Geol. Geophys.* 44, 47–72.
- Buslov, M.M., Watanabe, T., Fujiwara, Y., Iwata, K., Smirnova, L.V., Safonova, I.Y., Semakov, N., Kiryanova, A.P., 2004. Late Paleozoic faults of the Altai region, Central Asia: tectonic pattern and model of formation. *J. Asian Earth Sci.* 23, 655–671.
- Butler, O. T., Cook, J. M., Harrington, C. F., Hill, S. J., Rieuwerts, J. S., and Miles, D. L. 2007. Atomic spectrometry update. Environmental analysis. *Journal of Analytical Atomic Spectrometry* 22:187–221.
- Cabri, L.J., Chryssoulis, S.L., de Villiers, J.P.R., Laflamme, J.H.G., Bruseck, P.R. 1989: The nature of “invisible” gold in arsenopyrite. *Can Mineral* 27: 252-362
- Caswell, S.A., Holmes, I.F., Spears, D.A. 1984a: Total chlorine in coal seam profiles from the South Stafford-shire (Cannock) coalfield. *Fuel* 63 782-787
- Caswell, S.A., Holmes, I.F., Spears, D.A. 1984b: Water-soluble chlorine and associated major cations from the coal and mudrocks of the Cannock and North Staffordshire coalfields. *Fuel* 63: 774-781
- Cardott, B.J., Ruble, T.E., Suneson, N.H. 2007: Nature of migrabiturnen and their relation to regional thermal maturity Ouachita Mountains Oklahoma. *Energy Sources*. Vol.15: 239-267. DOI: 10.1080/00908319308909026
- Chen, S., Wu, D., Liu, G., Sun, R., 2017: Raman spectral characteristics of magmaticcontact metamorphic coals from Huainan coalfield, China. *Spectrochim. Acta A Mol. Biomol. Spectrosc.* 171, 31–39.
- Chou, C.L., Hackley K.C, Donnals, G.L., Cao, J., Ruch, R.R. 1992: Evolution of hydrogen chloride during temperature-programmed pyrolysis of Illinois coal. *Geol Soc Am Prog Abstr* 24: 202
- Chou, C.L. 2012: Sulphur in coals: a review of geochemistry and origins. *Int J Coal Geol* 100: 1–13
- Cook, N.J., Chryssoulis, S.L. 1990: Concentrations of "invisible gold" in common sulphides. *Canad Mineral* Vol28: 1-16
- Cook, N.J., Ciobanu, C.L., Mao, J. W. 2009: Textural control on gold distribution in As-free pyrite from the Dongping, Huangtuliang and Hougou gold deposits, North China craton (Hebei Province, China). *Chem. Geol.*, 264, 101–121.

- Cox, J.J., Krutzelmann, H., Smith, D.J.F., Raynor, J.P. 2010: Kyzyl Gold Project – Bakyrchik Deposit, Eastern Kazakhstan Preliminary Feasibility Study NI 43-101 Technical Report for Ivanhoe Mines Ltd, Scott Wilson Ltd. (2010), p. 249.
- Crocket, J.H. 1991: Distribution of gold in the Earth's crust in Foster RP eds Gold metallogeny and exploration. London New York NY Chapman and Hall: 1–36.
- Csontos, L., Nagymarosy, A., Horváth, F., Kovac', M. 1992: Tertiary evolution of the Intra-Carpathian area: a model. *Tectonophysics* 208:221–241.
- Csontos, L., Vörös, A. 2004: Mesozoic plate tectonic reconstruction of the Carpathian region. *Palaeo.* 210:1–56.
- Dai Sh, Seredin, V.V., Ward, C.R., Hower J.C., Xing, Y., Zhang, W., Song, W., Wang, P. 2015: Enrichment of U-Se-Mo-Re-V in coals preserved within marine carbonate successions: geochemical and mineralogical data from the Late Permian Guiding Coalfield Guizhou China. *Miner Deposita* 50: 159–186
- Dai Sh., James, C., Hower, R., Finkelman, T., Graham, D., Colin, R., Warde, G., Qiang, W., Lei, Zh. 2020: Organic associations of non-mineral elements in coal: A review. *J Coal Geol* 218: 103347
- Daukeev, S.Z., Uzhkenov, B.S., Bespaev, Kh.A., Miroshnichenko, L.A., Mazurov, A.K., Sayduakasov, M.A. (Eds.), 2004: Atlas of Mineral Deposit Models. Printing House “Center for Geoinformation of the MF RK”, Almaty.
- Daukeev, S.Z., Kim, B.C., Li, T., Petrov, O.V., Tomurtogoo, O., 2008: Atlas of Geological Maps of Central Asia and Adjacent Areas. Geological Publishing House, Beijing.
- Davidson, C.M., Ferreira, P.S., Ure, A.M. 1999: Some sources of variability in the application of the three-stage sequential extraction procedure recommended by BCR to industrially-contaminated soil. *Fresenius' J Anal Chem* 363: 446–451
- Deol, S., Deb, M., Large, R.R., Gilbert, S., 2012: LA-ICPMS and EPMA studies of pyrite, arsenopyrite and loellingite from the Bhukia–Jagpura gold prospect, southern Rajasthan, India: implications for ore genesis and gold remobilization. *Chemical Geology* 326–327, 72–87.
- Diehl, S.F, Goldhaber, MB, Koenig, A.E, Lowers, H.A, Ruppert, L.F. 2012: Distribution of arsenic, selenium, and other trace elements in the high pyrite Appalachian coals: evidence for multiple episodes of pyrite formation. *Int J Coal Geol.* 94:238–249.
- Dold, B., Fontboté, L. 2001: Element cycling and secondary mineralogy in porphyry copper tailings as a function of climate primary mineralogy and mineral processing. *Geochemistry Exploration* volume 74: 3-55

- Dunkl, I. 1992: A Kelet-Mecsek hôtörténete, kiemelkedése a fission track adatok tükrében - előzetes tanulmány. - Fission track evidences on the thermal history and uplift of the Eastern Mecsek Mountains (Hungary) - Preliminary results. *Ált. Földt. Szemle*, 26, 163-168
- Dyachkov, B.A., Mizernaya, M.A., Maiorova, N., Chernenko, Z., Maiorov, V., Kuzmina, O. 2011: Geotectonic Position and Metallogeny of the Greater Altai Geological Structures in the System of the Central Asian Mobile Belt Book: New Frontiers in Tectonic Research - General Problems Sedimentary Basins and Island Arcs DOI: 105772/21607
- Dyachkov, B., Mizernaya, M., Kuzmina, O., Zimanovskaya, N., Oitseva, T. 2017 Tectonics and Metallogeny of East Kazakhstan. Intechopen DOI: 105772/intechopen72745
- Eakin & Gize, 1992: Reflected-light microscopy. *Mineralogical Magazine*, March 1992, Vol. 56, pp. 85-99.
- Emese, T., Ervin, H., Felix, S., Tivadar T. 2022: Lithology-Controlled Hydrodynamic Behaviour of a Fractured Sandstone–Claystone Body in a Radioactive Waste Repository Site, SW Hungary. *Appl. Sci.*, 12(5), 2528;
- Emsbo, P., Koenig, A. 2007: Transport of Au in petroleum: Evidence from the northern Carlin Trend Nevada [abs]: Digging Deeper Biennial SGA Meeting 9th Dublin Society for Geology Applied to Mineral Deposits Proceedings: 695–698.
- Érdi-Krausz Gábor & Harsányi Lajos. 1997: Nemzeti kincs a NyugatMecsek mélyében. *FÖLDTANI KUTATÁS* 1997. XXXIV. Évfolyam 3. Szám.
- Fazekas, Via. 1987: A mecseki perm és alsótriász korú törmelékes formációk ásványos összetétele. *Földtani Közlöny, Butt, of the Hungarian Geol. Soc.* (1987). 117. 11 — 30
- Fehn, U., Cathles, L.M., & Holland H.D. 1978: Hydrothermal convection and uranium deposits in abnormally radioactive plutons. *Econ. Geol.*, 73: 1556-1566.
- Ferralis, N., Matys, E.D., Knoll, A.H., Hallmann, C., Summons, R.E., 2016: Rapid, direct and non-destructive assessment of fossil OM via micro-Raman spectroscopy. *Carbon* 108, 440–449
- Finkelman, R.B. 1980: Modes of occurrence of trace elements in coal. US Geol Surv Open-File Rep No OFR-81-99: 301 also PhD Thesis University of Maryland 1980

- Finkelman, R.B., Brown, Jr. R.D. 1991: Coal as host and as an indicator of mineral resources. In: Peters, D.C. (Ed.), *Geology in Coal Resource Utilization*. Fairfax, Techbooks, Virginia, pp. 471–481.
- Fleet, M.E, Chryssoulis, S.L., MacLean, P.J., Davidson, R., Weisener, C.G. 1993: Arsenian pyrite from gold deposits; Au and As distribution investigated by SIMS and EMP and color staining and surface oxidation by XPS and LIMS. *Can Mineral* 31: 1–17
- Fodor, L., Jelen, B., Márton, E., Skaberne, D., Vrabec, M. 1998: Miocene–Pliocene tectonic evolution of the Slovenian Periadriatic Line and surrounding area - implication for Alpine-Carpathian extrusion models. *Tectonics* 17:690–709.
- Franus, W., Wiatros-Motyka, M.M., Wdowin, M. 2015: Coal fly ash as a resource for rare earth elements. *Environ. Sci. Pollut. Res.* 22, 9464–9474.
- Fuchs, S., Anthony, E., Williams-Jones, S., Jackson, E. 2016: Metal distribution in pyrobitumen of the Carbon Leader Reef Witwatersrand Supergroup South Africa: Evidence for liquid hydrocarbon ore fluids *Chem Geol*: 2-25 DOI: 101016/jchemgeo201602001
- Fuxin, Z., Jianqin, M., Yanjing, C. 2001: Geochemical study of gold and arsenic mineralisation of the Carlin-Type gold deposits Qinling region China *Chin J Geochem* Vol 20 No 4: 1-10
- Földessy, J. 1997: Exploration potential of the W-Mecsek area. Report of the Rotaqua Kft. *Kővágószőlős*. pp.11
- Földessy, J. 1998: Geological Report: Diagnostic sampling of the formations of the W-Mecsek mountains. Budapest. pp.8
- Gatellier, J., & Disnar, J. 1989: OM and gold-ore association in a hydrothermal deposit. France *J Appl Geochem* Vol 4: 143-149
- Gao, Fuping., Du, Yangsong., Pang, Zhenshan., Du, Yilun., Xin, Fengpei., Xie, Jinsong. 2019: LA-ICP-MS Trace-Element Analysis of Pyrite from the Huanxiangwa Gold Deposit, Xiong’ershan District, China: Implications for Ore Genesis. 2019. *Minerals/* 03 Vol. 9; Iss. 3. DOI: 10.3390/min9030157
- Giordano, T.H. 1994: Metal transport in ore fluids by organic ligand complexation in Pitman ED and Lewan MD eds *Organic acids in geological processes*: New York Springer-Verlag: 319-354
- Giordano, T.H., Kharaka, Y.K. 1994: Organic ligand distribution and speciation in sedimentary basin brines diagenetic fluids and related ore solutions in Parnell J (ed)

- 1994 Geofluids: Origin Migration and Evolution of Fluids in Sedimentary Basins
175 Geological Society Special Publication No 78: 175-202
- Giordano, T.H. 2000: OM as a transport agent in ore-forming systems in (ed) Giordano TH
Kettler RM Wood SA Ore Genesis and Exploration: The Roles of OM Reviews in
Econ Geol Vol 9: 133-155
- Glikson, M., Golding, S.D., Boreham, C.J., Saxby, J.D. 2000: Mineralisation in eastern
Australia coals: a function of oil generation and primary migration In Glikson M and
Mastalerz M (eds) OM and Mineralisation 2000 Kluwer Academic Publishers: 314-
326
- Glorie, S., Grave, J.D., Delvaus, D., Buslov, M.M., Zhimulev, F.I., Vanhaecke, F., Elburg,
M.A., Van den haute, P., 2012: Tectonic history of the Irtysh shear zone (NE
Kazakhstan): new constraints from zircon U/Pb dating, apatite fission track dating
and paleostress analysis. *J. Asian Earth Sci.* 45, 138–149.
- Goldfarb, R.J., Taylor, R.D., Collins, G.S, Goryachev, N.A., Orlandini, O.F. 2014:
Phanerozoic continental growth and gold metallogeny of Asia Gondwana Res 25:
48–102
- Goldschmidt, V. M., & Peters., C. 1933: Über die Anreicherung Seltener Elemente in
Steinkohlen. *Nachr. Ges. Wiss. Gottingen. Math.-Phys. Kl., Fach. IV, No. 4*, 371–
387.
- Haas, J., F. Góczán, A. Oravecz-Scheffer, Á. Barabás-Stuhl, Gy. Majoros, A. Bérczi-Makk
1986: Permian Triassic boundary in Hungary. – *Mem. Soc. Geol. It.*, 34, pp. 221–
241.
- Haas, J. & Hámor G. 1998: Magyarország területe szerkezetfejlődésének összefoglalása,
in: Borezi I. és Jámor Á. (szerk.) (1998): Magyarország geológiai képződményeinek
régeltana, MOL Rt.-MÁFI kiadvány, Budapest, pp. 45-55. (Hungarian)
- Haas, J., Budai T., Csontos L., Fodor L., Konrád Gy. 2010: Pre-Cenozoic geological map
of Hungary, 1:500 000. Geol Inst Hung, Budapest
- Haas, J., 2012: *Geology of Hungary*. Springer. ISBN 978-3-642-21910-8 (eBook). DOI
10.1007/978-3-642-21910-8.
- Hallbauer, D.K. 1986: The mineralogy and geochemistry of Witwatersrand pyrite, gold,
uranium and carbonaceous matter, 731-752. In: Anhaeusser, C.R. & Maske, S., Eds.,
Mineral Deposits of Southern Africa, I. Geol. Soc. S. Afr., 1020 pp.
- Hámor, T., 1994: The occurrence and morphology of sedimentary pyrite. *Acta Geologica
Hungarica*, Vol. 37/2-2, pp. 153-181.

- Harangi, S.Z., Árváné-Sós, E. 1993: A Mecsek hegység alsókréta vulkáni kőzetei I. Ásvány- és kőzettan (in Hungarian with English abstract: Early Cretaceous volcanic rocks of the Mecsek Mountains (South Hungary) I. Mineralogy and petrography). — *Földtani Közlöny* 123 (2), pp. 129–165.
- Harrison, C.H. 1991: Electron microprobe analysis of coal macerals. *Org. Geochem.* Vol. 17, No. 4, pp. 439-449.
- Henderson, K.M., Williams-Jones, A.E., and Clark, J.R., 2019: Metal transport by liquid hydrocarbons: Evidence from metalliferous shale and pyrobitumen, Yukon; in *Targeted Geoscience Initiative: 2018 report of activities*, (ed.) N. Rogers; Geological Survey of Canada, Open File 8549, p. 179–187.
- Henrique-Pinto, R., Barnes, S., Savard, D.D., Mehdi, S. 2015: Quantification of metals and semimetals in carbon-rich rocks: a new sequential protocol including extraction from humic substances. *Geostandards and geoanalytical research*, pp. 1-22.
- Hinrichs, R., Brown, M.T., Vasconcellos, M.A.Z., Abrashev, M.V., Kalkreuth, W. 2014: Simple procedure for an estimation of the coal rank using micro-Raman spectroscopy. *Int. J. Coal Geol.* 136, 52–58.
- Hofstra, A. H. 1995: Timing and duration of Carlin-type gold deposits in Nevada and Utah—Relation to back-arc extension and magmatism. *Geological Society of America Abstracts with Programs.* 27(6): A-329.
- Huc, A., Nederlof, P., Debarre, R., Carpentier, B., Boussafir, M., Laggoun-Défarge, F., Lenail-Chouteau, Ar, Bordas-Le, Floch, N 2000: Pyrobitumen occurrence and formation in a Cambro–Ordovician sandstone reservoir Fahud Salt Basin North Oman. *Chem Geol/Elsevier* 168: 99-112 ff101016/S0009-2541(00)00190-X hal-00115104
- Hunt, J. M.: 1978: Characterization of bitumens and coals. *Bulletin of the American Association Petroleum Geologists* 62: 301-303
- Hwang, R.J., Terrman, S.C., Carlson, R.M.: 1998: Geochemical comparison of reservoir solid bitumens with diverse origins *Org Geochem* Vol 29 No 1-3: 505 517
- IAEA Report 2014: Uranium 2014 – Resources, Production and Demand. Chapter 3, National Reports – Hungary. A Joint Report by the OECD Nuclear Energy Agency and the International Atomic Energy Agency. pp. 244-250.
- Idiz, E.F., Carlisle, D. & Kaplan, I.R. 1986: Interaction between OM and trace elements in a uranium rich bog, Kern County, California, U.S.A. *Appl. Geochem.*, 1,573-590

- Ilchik, R. P., & Barton, M. D. 1997: An amagmatic origin of Carlin-type gold deposits. *Economic Geology*, 92(3): 269-288.
- Jacob, H. 1989: Classification structure genesis and practical importance of natural solid bitumen (“migrabitumen”). *Int. J. Coal Geol.* 11: 65–79
- Jantsky, B. 1979: A mecseki gránitosodott kristályos alaphegység földtana (Géologie du socle cristallin granité de la montagne Mecsek). — A Magyar Állami Földtani Intézet Évkönyve 60, 385 p.
- Jehlicka, J., Urban, O., Pokorný, J. 2003: Raman spectroscopy of carbon and solid bitumens in sedimentary and metamorphic rocks. *Spectrochimica Acta Part A* 59: 2341-2352
- Jiuling, L., Feng, Q., Quingsheng, X. 1997: The role of organic and carbonaceous matter in the formation of Carlin-type disseminated gold deposits. *Proceedings of the 30th International Geological Congress Vol 9: 337-354* Pei Rongfu (Ed) VSP. Netherlands, 1997. ISBN 90-6764-264-9.
- Junussov M., 2018a. Geological and mineralogical characteristics of gold and polymetallic minerals of the mining Maykain “B” deposit (North-east Kazakhstan), ISZA 2018. Hungary, 6-7. April 2018 (publication in local conference proceedings). p. 2.
- Junussov M., 2018c. Characteristics, distribution and morphogenesis of gold-bearing sulphide minerals in the gold black shale deposit of Bakyrchik. *Proceedings SGEM 2018. Bulgaria, 30 June-9 July 2018.* (publication in international conference) p. 1111-1118.
- Junussov M., 2018d. Looking for “Invisible gold” and its concentrations in arsenic-containing sulphide minerals of Bakyrchik gold deposit, *MicroCad 2018. Hungary, 5-6 September 2018.* (publication in local conference) p.8.
- Junussov M., Mádai F., Bánhidi O. 2018a. Sequential extraction of carbonaceous siltstone rock for multielement analysis by ICP OES. *Journal of Contemp.Trends.Geosci.*, 7(2), 2018, pp. 145-152. DOI: 10.2478/ctg-2018-0010 (Poland, Publisher - Sciendo).
- Junussov M., Umarbekova Z., 2018b. Mineralogical and morphological studies of gold-bearing arsenopyrite and pyrite minerals of Bakyrchik and Bolshevik gold black shale deposits (Eastern Kazakhstan). *Journal of Contemp.Trends.Geosci.*,7(2), pp. 153-165. DOI: 10.2478/ctg-2018-0011 (Poland, Publisher - Sciendo).
- Junussov M., Mádai F., Kristály F., 2018c. A two-step sequential extraction for analysing hardly accessible precious metals in sulphide ore-bearing sedimentary rocks. *Journal*

- of geological resources and engineering, Vol.7 №1 2019 (Ser.№ 27) pp. 32-38. doi:10.17265/2328-2193/2019.01.004 (USA, Publisher – David publishing).
- Junussov M., 2020a. Chemical demineralisation and physical isolation of kerogens from ores for a further analysis of metal-organic complex. Proceeding Satpayev's readings. Online. 12 April 2020 (publication in domestic conference) p. 5.
- Junussov M., 2020b. Geochemical and infrared analysis of metal-organic compound sedimentary rocks using Western Mecsek and Bakyrchik metalliferous black shale deposit. Online. 12 April 2020 (publication in domestic conference). p. 5.
- Junussov M., Mádai F., Kristály F., Tóth T., Fintor K., Muránszky G., Preko Á., Hámor-Vidó M. 2021. Preliminary analysis on roles of metal-organic compounds in formation of “invisible” gold. Journal of Acta Geochemica (Q3). doi.org/10.1007/s11631-021-00494-y (Springer - 2021). p. 1050-1072.
- Kádas, M. 1983: Analysis on trace elements in coals of Mecsek. Geological research. (A mecseki feketekőszén nyomelemvizsgálatának legújabb eredményei. Földtani Kutatás, in Hungarian) 26, 81-82.
- Kam-Hung, Wong., Mei-Fu Zhou, Wei Terry Chen., Hugh O'Brien., Yann Lahaye, Sik-Lap Jacky Chan. 2017: Constraints of fluid inclusions and in-situ S-Pb isotopic compositions on the origin of the North Kostobe sediment-hosted gold deposit, eastern Kazakhstan. Ore Geology Reviews 81 (2017) 256–269.
- Kassai, M. 1980: A Dél-Dunántúl perm végi ősföldrajzi rekonstrukciók a és a környező országokkal kapcsolatos néhány rétegtani összehasonlítás — Földt. Közi. 110. pp. 342—359.
- Kexin, Wang., Degao, Zhai., Jiajun, Liu., Han, Wu. 2021: LA-ICP-MS trace element analysis of pyrite from the Dafang gold deposit, south China: Implications for ore genesis. Ore Geology Reviews. 2021. DOI: <https://doi.org/10.1016/j.oregeorev.2021.104507>, Article 104507
- Kiss, J. 1958: La genèse de chrome uranifère et son rôle paragéniétique dans l'ensemble permien du Mecsek. (Deux, Conf. Int. des Nations Unies).
- Kiss, J. 1960: Az urán-krom-vanádium eloszlása és az epigén kromcsülám szerepe a mecseki permii összletben. X oldt. Közi. 90/1.
- Klötzli, U.S., Buda, G., Koller, F. 1999: Geochronological evidence for the derivation of the Mecsek Mountains, South Hungary from Variscan Central Europe. Beih Z Eur J Mineral 11: 126.

- Klötzli, U.S., Buda, Gy., Skiold, T. 2004: Zircon typology, and whole rock Sm-Nd isotope systematics of the Mecsek Mountains granitoids in the Tisia Terrane (Hungary). *Miner Petrol* 81:113–134
- Kouketsu, Y., Mizukami, T., Mori, H., Endo, S., Aoya, M., Hara, H., Nakamura, D., Wallis, S. 2014: A new approach to develop the Raman carbonaceous material geothermometer for low-grade metamorphism using peak width. *Island Arc* 23: 33–50
- Konrád, G. & Sebe, K. 2010: New Details of Young Tectonic Phenomena in the Western Mecsek Mts and Their Surroundings. *Bull. Hung. Geol. Soc.*, 140, 135–162.
- Konrád, G.Y., Földing, G., Barabás, A., Unyi, P. 2012: Geology, experimental in situ leaching and site remediation of the Dinnyeberki uranium ore deposit. *Földtani Közlöny* 142(4):357–374 (in Hungarian with English abstract).
- Kovalev, K.R., Kalinin, Y.A., Naumov, E.A., Pirajno, F., Borisenko, A.S., 2009: A mineralogical study of the Suzdal sediment hosted gold deposit, Eastern Kazakhstan: implications for ore genesis. *Ore Geol. Rev.* 35, 186–205.
- Kovalev, K.R., Kalinin, Y.A., Naumov, E.A., Kolesnikova, M.K., Korolyuk, V.N., 2011: Goldbearing arsenopyrite in eastern Kazakhstan gold-sulphide deposits. *Russ. Geol. Geophys.* 52, 178–192.
- Kovalev, K.R., Kalinin, Y.A., Naumov, E.A., Myagkaya, M.K., 2014: Relationship of antimony with gold mineralisation in the ore districts of Eastern Kazakhstan. *Russ. Geol. Geophys.* 55, 1170–1182.
- Kovács, S., Szederkényi, T., Haas, J., Hámor, G., Nagymarosy, A., 2000: Tectonostratigraphic terranes in the pre-Neogene basement of the Hungarian part of the Pannonian area. *Acta Geologica* 43, 225–328.
- Király, G. (szerk.) 2009: Új magyar fűvészkönyv. Magyarország hajtásos növényei. Határozókulcsok. – Aggteleki Nemzeti Park Igazgatóság, Jósvafi. 616 pp.
- Kuzmina, O.N. 2011: Geology, mineralogy and formations of gold-sulphide ores in East Kazakhstan (Zhaymen ore field) Dissertation work. Novosibirsk. pp. 240. (in Russian).
- Lakatos, J., Brown, S. D., & Snape, C., E. 1997: “Unexpectedly High Uptake of Palladium by Bituminous Coals,” in *Proceedings of ICCS’97 (DGMK, Essen, 1997)*, Vol. 1, pp. 247–250.
- Laczó, I. 1983: Máza-Dél-Váralja-Dél-i terület liász összletének vitrinitreflexió (Ro) értékei és azok földtani értékelése - *Földt. Kut.* 26. 2-3., pp. 57-61.

- Langmuir, D. 1979. Techniques of estimating thermodynamic properties for some aqueous complexes of geochemical interests. In: JENNE, E.A. (ed.) *Chemical Modeling in Aqueous Systems*. American Chemical Society Symposium Series, 93, 353-387.
- Large R.R., Maslennikov V.V.. 2020. Invisible gold paragenesis and geochemistry in pyrite from orogenic and sediment-hosted gold deposits *Minerals*, 10 (2020), p. 339
- Levitan G 2008: *Gold deposits of the CIS USA*: Xlibris Corporation.
- Lelkes-Felva'ri Gy, Mazzoli C, Visona' D (1989) Contrasting mineral assemblages in polymetamorphic rocks from South Transdanubia, Hungary. *Eur Journal Miner* 1:143–146
- Lelkes-Felvári, Gy., Frank, W. 2006: Geochronology of the metamorphic basement, Transdanubian part of Tisia Mega-unit. *Acta Geol Hung* 49(3):189–206
- Li, D., He, D., Ma, D., Tang, Y., Kong, Y., Tang, J., 2015: Carboniferous–Permian tectonic framework and its later modifications to the area from eastern Kazakhstan to southern Altai: insights from the Zaysan–Jimunai Basin evolution. *J. Asian Earth Sci.* 113, 16–35.
- Li K., Rimmer S.M., Presswood S.M., Liua Q. 2019a: Raman spectroscopy of intruded coals from the Illinois Basin: Correlation with rank and estimated alteration temperature. *Int. J. Coal Geol.* 219 (2020) 103369.
- Li K., Rimmer, S.M., Liu Q., Zhang Y., 2019b: Micro-Raman spectroscopy of microscopically distinguishable components of naturally graphitized coals from Hunan, China. *Energy Fuel* 33, 1037–1048.
- Lin Q, Fu J-M, Liu D-H, Sheng G-Y, and Lu J-L. 1993. Genetic relationship between the oil gas evolution and some gold deposits. *Geochimica*, 22(3): 62-71. (In Chinese).
- Liang L Jian-Ming Zh 2016 An optimized sequential extraction scheme for molybdenum association in environmental samples *Acta Geochim* 35(2): 111–119 DOI 101007/s11631-016-0096-4
- Liu, D-S, and Geng, W-H. 1985. On the mineral association and mineralisation conditions of the Carlin-type gold deposits in China. *Geochimica*, No.3, 277-282. (In Chinese)
- Liu D.H. Xiao X.M. Tian H., Min Y.Sh. Zhou Q. Cheng, P. Shen J.G. 2013: Sample maturation calculated using Raman spectroscopic parameters for solid organics: Methodology and geological applications. *Chinese Science Bulletin* Vol.58 No.11: 1285-1298.

- Liu, J-Z, Fu, J-M, and Lu, J-L. 1994. Experimental research on the role of organic matter information of sedimentary-reworked gold ore deposits. *Science in China (Series B)*, 37(7): 859-859.
- Liu, X-F, Su, W-C, and Zhu, L-M. 1999. An approach on mechanism of juvenile fluid mineralisation for Carlin-type gold deposits in Yunnan-Guizhou-Guangxi. *Geology and Prospecting*, 35(1): 14-19. (In Chinese).
- Lubecky, V.N., Bespaev, H.A., Libeckay, L.D. 2008: The deep model of fold deposits of Bakyrchik and Vasyilkovskoe IGS named KI Satpaev No1: 25-36 (in Russian)
- Lyons, J.J., Coe, R.S., Zhao, X., Renne, P.R., Kazansky, A.Y., Izokh, A.E., Kungurtsev, L.V., Mitrokhin, D.V., 2002: Paleomagnetism of the early Triassic Semeitau igneous series, eastern Kazakhstan. *J. Geophys. Res.* 107 (B7), 2139. <http://dx.doi.org/10.1029/2001JB000521>.
- Malec, J., Veselovsky, F., Bohmova, V., Prouza, V., 2012: Jacutingaite, palladian gold and Pd-selenide in the copper ore from Carboniferous sediments by Kostalov near Semily (Krkonoše Piedmont Basin, Czech Republic). *Geosci. Res. Rep.* 2011, 189–192 (in Czech).
- Machovič, V., Havelcová M., Sýkorová I., Borecká L., Lapčák L., Mizera J., Kříbek B., Krist P. (2021). Raman mapping of coal halos induced by uranium mineral radiation. *Spectrochimica Acta Part A: Molecular and Biomolecular Spectroscopy* 246. 118996
- Marchenko, L.G. 2010: Micro and nano-mineralogy of gold in a black shale formation Almaty ISBN 978-601-278-228-8: 2-138 (In Russian)
- Marchenko, L.G., & Komashko, L.V. 2011: The role of nanostructured particles and carbon films in accumulation of precious metals on deposits “black shale” type *Izvestiya NAN RK Sergeologicheskaya №5*: 6-85 (In Russian)
- Maros, Gy., Koroknai, B., Palotás, K., Misitz, B., Fűri, J., Borsody, J., Kovács-Pálffy P., Kónya, P., Viczián, I, Kad, B., Pécskay, Z. 2010: Brittle fault Zones in the Mórány Granite: New structural and K-Ar data. *Ann Rep Hung Geol Inst* 2009:91–112.
- Malchenko, A. 2017: MKRU. [online]. Available at: <https://mk-kz.kz/articles/2017/10/05/v-vostochnom-kazahstane-raspolozhen-odin-iz-mirovykh-larcov-s-zolotom.html>
- Maslennikov, V.V., Rogacheva, T.A., Abaza, V.I., 1997: Report on reserve calculation on the Bakyrchik deposit as on 01.01.1997. Unpubl. Prof. Report, Semipalatinsk. (in Russian).

- Meitov, E.S., Rodionov V.D. 1993: Nonconventional sources of rare metals. *Razv. Okhr.Nedr* 5, 19–21 (in Russian).
- Migdisov, A.A., Guo, X., Xu, H., Williams-Jones, A.E, Sun, C.J., Vasyukova, O., Sugiyama, I., Fuchs, S., Pearce, K., Roback, R. 2017: Hydrocarbons as ore fluids. *Geochem Persp Let* 5: 47-52 DOI: 107185/geochemlet1745
- Milner, C.W., Rogers, M.A., Evans, C.R. 1977: Petroleum transformations in reservoirs *J Geochem Explor* 7: 101-153
- Miloš, R. 2017: History of Uranium Mining in Central Europe. Book: Uranium - Safety, Resources, Separation and Thermodynamic Calculation. 2018. DOI: 10.5772/intechopen.71962.
- Mizernaya, M.A. 2001: Location of shungite in black shale formation of West Qalba Herald VKGTU No1: 32-40 (in Russian)
- Mukherjee, S., & Borthakur, P.C. 2003: Effect of leaching high sulphur subbituminous coal by potassium hydroxide and acid on removal of mineral matter and sulphur. *Fuel* 82 783–788.
- Narseev, V.A., Gostev, Yu.V., Zaharov A.V. 2001: Bakyrchik (geologiya geohimiya orudinenie) Moskva: 174
- Naumov, E., Borisenko, A., Kovalev, K., Kalinin, Y., Seltmann, R., 2012: Gold Deposits of Ob-Zaisan Fold Zone (Western Siberia and Eastern Kazakhstan): Types and Ages of Mineralisation Correlation with Magmatic Complexes [abs.], 34th International Geological Congress, Brisbane, Australia Abstract.
- Nayak, B., Chakravarty, S., and Bhattacharyya, K.K. 2008: Invisible gold in the high-sulphur Tertiary coals of Northeast India. *Current science*, Vol. 95, No. 9,
- Noddack, I. 1936: “Uber die Allgegenwart der Chemischen Elemente,” *Angew. Chemie* 49 (47), 809–816.
- Novojilov, Yu. I. Gavrilov, A. M. 1999: Gold-sulphide deposits in carbonaceous-terrigenous formations Moscow: CNIGRI.
- Nuclear Power. 2022:[Online]. Available at: <https://world-nuclear.org/information-library/country-profiles/countries-g-n/hungary.aspx>
- Ódor, L. 1967: Report on the geochemical investigation of the Eocene brown-coal sequence of the Baiinka II area. *Magy. All. Foldt. Intez. EviJel*, 315-343
- Ódor, L. 1969: The Be content of Transdanubian Eocene coals. *Magy. All. Foldt. Intez. EviJel.*, 123-131.

- Osovetzky, B. 2017: Natural nanogold ISSN 2366-1593 (electronic) Springer Mineralogy ISBN 978-3-319-59158-2: 91-97
- Osseo-Asare, K. A., Afenya, P. M., & Abotsi, G. M. K. 1984: Carbonaceous matter in gold ores: isolation, characterization and adsorption behaviour in aurocyanide solutions. In Unknown Host Publication Title pp. 125-144.
- Parnell, J. 1988: Metal enrichments in solid bitumens: A review. *Mineral Deposita* 23: 191-199
- Parnell, J, & McCready, A. 2000: Paragenesis of gold- and hydrocarbon-bearing fluids in gold deposits Book: Kluwer Academic Publishers M Glikson and M Mastalerz (eds) OM and Mineralisation: 38-52
- Parnell, J, Kucha, H, and Landais, P. 1993: Bitumens in ore deposits. Special publication no. 9 of the Society for Geology Applied to Mineral Deposits, no. 9. ISBN 978-3-642-85808-6.
- Parnell, J. 2019: Variscan cycling of gold into a global coal reservoir. *Ore Geol. Rev.* 114 103158: 1-7
- Philips, G. N., and Powell, R. 1993. Link between gold provinces. *Economic Geology*, 88: 1084-1098.
- Polymetal ltd. 2022 [Online]. Available at: <https://www.polymetalinternational.com/en/investors-and-media/news/press-releases/01-03-2021/>
- Powell, T.G. (1984) Some aspects of the hydrocarbon geochemistry of a Middle Devonian barrie-reef complex Western Canada In: *Petroleum Geochemistry and Source Rock Potential of Carbonate Rocks* ed J G Palacas American Association Petroleum Geologists Studies in Geology 18: 45-62
- Pápay, L. 2018: Coal Mining and Risks Linked to Their Underground Mining Operations in the Mecsek Mountains (SE Transdanubia, Hungary). *Historia Scientiarum – Hungarian Technical Society of Transylvania* 16, 27-34.
- Presnell, R. 1993. The association of gold and hydrocarbons in sediment-hosted disseminated gold deposits. *AAPG Bulletin*, 77(8): 1459.
- Hanping Z, Jialan L, Jiamo F, Chigang R, Degang Z. 1999: Crude oil as carrier of gold: petrological and geochemical evidence from Lannigou gold deposit in southwestern Guizhou China Science in China Series D: Earth Sciences volume 42: 216–224
- Iwata, K., Obut, O.T., Buslov, M.M., 1997: Devonian and Early carboniferous radiolarian from the chara ophiolite belt, East Kazakhstan. *Micropaleontologist* 10, 27–32.

- Ondrejka, M., Li, XH., Vojtko, R., Putiš, M., Uher, P., Sobocký, T. 2018: Permian A-type rhyolites of the Muraň Nappe, Inner Western Carpathians, Slovakia: in situ zircon U–Pb SIMS ages and tectonic setting. *Geol Carpath* 69(2):187–198. <https://doi.org/10.1515/geoca-2018-0011>
- Quirico, E., Raynal, P.I., Bourot-Denise M. 2003: *Meteorit. Planet. Sci.* 38. 795.
- Quirico, E., Rouzaud, J.-N., Bonal L., Montagnac G., 2005: Maturation grade of coals as revealed by Raman spectroscopy: progress and problems. *Spectrochim. Acta Part A Mol. Biomol. Spectrosc.* 61, 2368–2377.
- Fülöp, J. 1994: Magyarország geológiája, Paleozoikum II (Geology of Hungary, Paleozoic II). Akadémiai Kiadó, Budapest (in Hungarian)
- Radtke, A.S., Scheiner, B.J. 1970: Studies of hydrothermal gold deposition 1 Carlin Gold Deposit Nevada: the role of carbonaceous materials in gold deposition. *Econ Geol* 65: 87-102
- Raiswell, R. 1982: Pyrite texture, isotopic composition and the availability of iron. - *Am. J. Sci.*, 282, pp. 1244-1263.
- Rafaylovich, M.S. 2009: The large gold-sulphide deposit of Bakyrchik in Kazakhstan: geological structure prospecting model. *Geology and Mineral Resources* 4: 31–38
- Rafaylovich, M.S., Myzernaya, M.A., D'yachkov, B.A. 2011) The gold deposits in the black shale formations: condition of origin similarity *Almaty*: 55-76
- Raffensperger, J.P., & Garven, G., 1995: The formation of unconformity-type uranium ore deposits. 2 Coupled hydrochemical modeling. *Am. J. Sci.*, 295: 639-696.
- Razvozhzaeva, E.A., Prokof'ev, V.Y., Spiridonov, A.M., Martikhaev, D.K., Prokopchuk, S.I. 2002: Precious metals and carbonaceous substances in ores of the Sukhoi Log deposit eastern Siberia Russia: *Geol Ore Depos* 44: 103–111
- Reich, M., Kesler, S.E., Utsunomiya, S. 2005: Solubility of gold in arsenian pyrite. *Geochimica et Cosmochimica Acta* 69: 2781-2796
- René, M. 2014: Rare-earth, yttrium and zirconium mobility associated with the uranium mineralisation at Okrouhlá Radouň, Bohemian Massif, Czech Republic. *Eur J Mineral* 27:57–70. <https://doi.org/10.1127/ejm/2015/0027-2422>.
- Rogers, M.A., McAlary, J.D., Bailey, N.J. 1974: Significance of reservoir bitumens to thermal-maturation studies West Canada Basin. *Bulletin of the American Association Petroleum Geologists* 58: 1806-1824

- Rojkovic, I., Francu, J., & Caslabsky, J. 1992: Association of organic matter with uranium mineralisation in the Permian sandstones of the Western Carpathians. *Geologica Carpathica*, 43, 1, Bratislava, pp. 27-34.
- Romberger, S.B. 1988: Geochemistry of gold in hydrothermal deposits. US Geological Survey Bulletin 1857-A A9–A25
- Ronald, W.T., Wilkins, Neil Sherwood., Zhongsheng, Li 2018: RaMM (Raman maturity method) study of samples used in an interlaboratory exercise on a standard test method for determination of vitrinite reflectance on dispersed organic matter in rocks. *Marine and Petroleum Geology* 91 (2018) 236–250.
- Ross, R.L., Stuart, W.B., Valeriy, V.M. 2011: Carbonaceous Sedimentary Source-Rock Model for Carlin-Type and Orogenic Gold Deposits. *Econ Geol* v 106: 331–358
- Rubin, J.N., Henry, C.D., Price, J.G. 1993: The mobility of zirconium and other “immobile” elements during hydrothermal alteration. *Chem Geol* 110:29–47. [https://doi.org/10.1016/0009-2541\(93\)90246-f](https://doi.org/10.1016/0009-2541(93)90246-f).
- Safonova, I.Y., Simonov, V.A., Kurganskaya, E.V., Obut, O.T., Romer, R.L., Selmann, R., 2012: Late Paleozoic oceanic basalts hosted by the char suture shear zone, East Kazakhstan: geological position, geochemistry, petrogenesis and tectonic setting. *J. Asian Earth Sci.*49, 20–39.
- Santbrd, R.F. 1994: A quantitative model of ground-water flow during formation of tabular sandstone uranium deposits. *Econ.Geol.*, 89: 341-360.
- Sawlowicz, Z. 1993: Pyrite framboids and their development: a new conceptual mechanism. *Geol. Rundsch.* 82, 148–156.
- Saxby, J.D. 1976: The significance of OM in ore genesis. Jn: Wolf KH (ed) *Strata-Bound and Stratiform Ore Deposits*, 2nd Ed. Elsevier, Amsterdam pp 111–134
- Shcherba, G.N. Global mobilism (main provisions). *Geodynamics and Minerageny of Kazakhstan*. 2000; RIVOVAKRK(1):40-45
- Scott, R.J., Meffre, J., Woodhead, S.E., Gilbert, R.F., Berry, P.E. 2009: Development of framboidal pyrite during diagenesis low-grade regional metamorphism and hydrothermal alteration. *Econ Geol* 104(8): 1143-1168 [doi:102113/gsecongeo10481143](https://doi.org/10.1016/j.econgeo.2009.04.001)
- Selmecziné, Antal Pirooska, & Vincze, János. 1986: Cím: A szénült és ásványosodott növényi maradványok szerepe a mecseki uránércesedésben Forrás: *Földtani közlöny* 116. köt. 2. sz. 11-136.

- Seredin, V. V. 2007: Distribution and Formation Conditions of Noble Metal Mineralisation in Coal-Bearing Basins. 2007. ISSN 1075-7015, *Geology of Ore Deposits*, 2007, Vol. 49, No. 1, pp. 1–30.
- Seredin, V.V. & Finkelman R.B. 2008: Metalliferous coals: A review of the main genetic and geochemical types. *Int. J. Coal Geol.* 76, 253–289
- Schmid SM, Bernoulli D, Fügenschuh B, Matenco L, Schuster R, Schefer S, Tischler M, Ustaszewski K. 2008: The Alpine-Carpathian-Dinaridic orogenic system: correlation and evolution of tectonic units. *Swiss J Geosci* 101:139–183.
- Schmidt, J.S., Araujo, C.V., Souza, I.V.A.F., Chagas, R.B.A. 2015: Hydrous pyrolysis maturation of vitrinite-like and humic vitrinite macerals: Implications for thermal maturity analysis: *Int. J. Coal Geol.*, v. 144–145, p. 5–14, doi:10.1016/j.coal.2015.03.016
- Swaine, D.J., 1990. *Trace Elements in Coal*. Butterworths, London. 278 p.
- Sillitoe, R. H., and Bonham, H. F. 1990: Sediment-hosted gold deposits—Distal products of magmatic-hydrothermal systems. *Geology*, 18: 157-161.
- Simon, G, Kesler, S.E., Chryssoulis, S. 1999: Geochemistry and textures of gold-bearing arsenian pyrite Twin Creeks Nevada: implications for deposition of gold in Carlin-type deposits. *Econ Geol* 94: 405-422
- Simoneit, B.R.T. 1994: Lipid/bitumen maturation by hydrothermal activity in sediments of Middle Valley Leg 139 In: Mottl M David E Fisher A Slack J (eds) *Proceedings of the ocean drilling program scientific results vol 139 Ocean Drilling Program College Station: 447–465*
- Simoneit, B.R.T. 2000: Alteration and migration processes of OM in hydrothermal systems and implications for metallogenesis In: Glikson M Mastalerz M (eds) *OM and mineralisation: thermal alteration hydrocarbon generation and role in metallogenesis Kluwer Academic Publishers Dordrecht: 13–37*
- Simoneit, B.R.T. 2018: *Hydrothermal Petroleum* In Wilkes H (ed) *Hydrocarbons Oils and Lipids: Diversity Origin Chemistry and Fate Handbook of Hydrocarbon and Lipid Microbiology Springer International Publishing AG part of Springer Nature* https://doi.org/10.1007/978-3-319-54529-5_16-2
- Soloviev, Serguei G., Sergey, G. Kryazhev, Svetlana, S. Dvurechenskaya, Sergey I. Trushin., Spirakis, C.S. 2020: The large Bakyrchik orogenic gold deposit, eastern Kazakhstan: Geology, mineralisation, fluid inclusion, and stable isotope

characteristics. *Ore Geol. Rev.* Volume 127. pp. 28.
doi.org/10.1016/j.oregeorev.2020.103863.

- Stasiuk, L.D. 1997: The origin of pyrobitumens in Late Devonian Laduc Formation gas reservoir Alberta Canada: an optical and EDS study of oil to gas transformation. *Mar Pet Geol* 14: 915–929
- Steadman, J.A., Large, R.R., Olin, P.H., Danyushevsky, L.V., Meffre, S., Huston, D., Fabris, A., Lisitsin, V., Wells, T. 2021: Pyrite trace element behavior in magmatic-hydrothermal environments: An LA-ICPMS imaging study. *Ore Geol. Rev.*, 128 (2021), Article 103878.
- Sung, Y.H., Brugger, J., Ciobanu, L., Pring, A., Skinner, W., Nugus, M. 2009: Invisible gold in arsenian pyrite and arsenopyrite from a multistage Archaean gold deposit: Sunrise Dam, Eastern Goldfields Province, Western Australia. *Miner. Depos.*, 44, 765–791.
- Svingor, É., & Kovách, Á. 1981: Rb–Sr isotopic studies on granodioritic rocks from the Mecsek Mountains, Hungary. *Acta Geol Hung* 24(2–4):295–307.
- Sýkorová, I., Kribek, B., Havelcová, M., Machovič, V., Spaldónov, A., Lapcák, L., Knesl, I., Blázek, J. 2016: Radiation- and self-ignition induced alterations of Permian uraniferous coal from the abandoned Novátor mine waste dump (Czech Republic). *International Journal of Coal Geology*. DOI: 10.1016/j.coal.2016.08.002
- Tosdal, R. M., Clin, J. S., Hofstra, A. H., Peters, S. G., Wooden, J. L., and Young-Mitchell, M. N. 1998: Mixed sources of Pb in sedimentary-rock-hosted Au deposits, Northern Nevada. In *Contributions to the gold metallogeny of Northern Nevada*. Edited by Tosdal, R. M. U.S.G.S. Open-File Report, 98-338. U.S. Geological Survey, Menlo Park, CA. 223-233.
- Yang, K-Y & Dong, Z-S. 1994. Carlin-type gold deposits in Yunnan, Guizhou, Guangxi and northwestern Sichuan Provinces. In: *Advances of gold deposit researches in China*. Edited by Gold resource section of Chinese Academy of Sciences. Volume 1(2), Dizhen Publish House. 284-347. (In Chinese).
- Szalay, S. 1954: Enrichment of uranium in some brown coals in Hungary. *Acta Geol. Acad. Sei. Hung.*, 2, 299-311; *CA*, 48, 12629.
- Szalay, S. & Almassy, G. 1956: Analytical investigations on the uranium content of Hungarian coals. *Mag. Tud. Akad. Kern. Tud. Oszt. Kozl*, 8, 33-38; *CA*, 52, 7657

- Szalay, A. 1969: Accumulation of uranium and other trace metals in coal and organic shales and the role of humic acids in these geochemical enrichments. *Ark. Mineral. Geol*, 5(3), pp. 23-36.
- Szádeczky-Kardoss, E. 1959: A kárpáti közbenső tömeg magmás mechanizmusáról (in Hungarian, translated title: On the magmat-ic mechanism of the Carpathian inner mass). — Conference on Geochemistry of the Department of Technical Sciences of the Hungarian Academy of Sciences, 5–10. October, 1959, Budapest, Volume 21.
- Szederkényi, T. 1962: Földtani jelentés a Ny-Mecseki (Gyűrűfü) kvarcporfir földtani, közettani és radiológiai vizsgálatának eredményeiről. Report, Mecsekérc Ltd. (former Mecsek Ore Mining Company).
- Szederkényi, T, Árkai P, Lelkes-Felvári Gy. 1991: Crystalline basement of the Great Hungarian Plain and South Transdanubia, Hungary. In: Karamata S (ed) Geodynamic evolution of the Pannonian Basin. *Serb Acad Sci Arts Acad Conf* 62: 261–272.
- Szederkényi, T. 1997: A Tiszai egység (Tisia összetett terrénum) magyarországi része'nek metamorf ké'pződme'nyei e's korrela'cio'juk (Metamorphic formations of the Hungarian part of the Tisza Unit [Tisia Composite Terrane] and their correlation). In: Haas J (ed) Fülöp József emlékkönyv. Akad Kiadó', Budapest, pp 133–147. (in Hungarian)
- Szederkényi, T., Haas, J., Nagymarosy, A., & Hámor, G. 2012: Geology and History of Evolution of the Tisza Mega-Unit. pp. 103-149 Book: *Geology of Hungary*. Editors Roland Oberhänsli, Maarten de Wit, Francois M. Roure.
- Szemerédi, M, Varga, A, Lukács, R, Pál-Molnár E. 2016: Petrography of the Gyűrűfü Rhyolite Formation, Western Mecsek Mts, Hungary. *Földtani Közlöny* 146(4):335–354 (in Hungarian with English abstract).
- Szemerédi, M, Varga, A, Lukács, R, Pál-Molnár, E. 2017: Petrography of the Gyűrűfü Rhyolite Formation, northern foreland of the Villány Mts, Hungary. *Földtani Közlöny* 147(4):357–382. <https://doi.org/10.23928/foldt.kozl.2017.147.4.357>(in Hungarian with English abstract).
- Szemerédi, Máté., Andrea, Varga., János, Szepesi., Elemér Pál-Molnár, & Réka Lukács
VIEW MORE 2020: Lavas or ignimbrites? Permian felsic volcanic rocks of the Tisza Mega-unit (SE Hungary) revisited: A petrographic study. *AkJournals*. Volume 63: Issue.1 <https://doi.org/10.1556/24.2020.00003>

- Szilágyi, M. 1971: The role of organic material in the distribution of Mo, V and Cr in coalfields. *Econ. Geol.*, 66, 1075-1078.
- Taylor, G.H., Teichmüller, M., Davis, A.C.F.K., Diessel, C.F.K., Littke, R. and Robert, P. 1998: *Organic Petrology: A New Handbook Incorporating Some Revised Parts of Stach's Textbook of Coal Petrology*. Borntraeger, Berlin-Stuttgart, 704.
- Tarnocai, C.A., Hattori, K., & Cabri, L.J. 1997: "Invisible" gold in sulphides from Campbell mine Red lake greenstone belt Ontario: evidence for mineralisation during the peak of metamorphism. *Canad Mineral* 35: 805-815
- Tissot, B.P., & Welte, D.H. 1984: *Petroleum formation and occurrence* 2nd ed; Springer-Verlag: Berlin: 699
- Trubnikov, L.M. 1976: Geological map: M-44-G (Oskemen) of the geological map of Kazakh SSR scale: 1:500000 Regional-geological organization of East Kazakhstan (in Russian)
- Tseng, B.H., Kuang, M.B., Hsieh, C., Wert, C.A., & Dyrkacz, G.R. 1986: Organic sulphur in coal macerals. *FUEL*, Vol 65. 385-389.
- Umarbekova, Z.T., Dyusembaeva, K.Sh., Kubashev, K.T. 2017a: The Bakyrchik deposit and views on the formation of the mineral deposits in black shale beds. ISSN 2224-5278 Vol 2 No 422: 23-30 (in Russian)
- Umarbekova, Z. T., Seltmann, R., Dyussebayeva, K.Sh., Kokkuzova, M. 2017: The gold ore deposit Bakyrchik and views on the formation of the mineral deposits in black shale strata SGEM Albania Bulgaria ISSN 1314-2704 Vol 17 No 11: 1111-1118
- Umarbekova, Z.T., & Dyusembaeva, K.Sh. 2019: The characteristics and formation of black shale-hosted Bakyrchik-type gold mineralisation. *Appl Earth Sci* 128/2: 61-62 DOI: 101080/2572683820191607183
- Usmanova, N.F., Bragina, V.I., Zhizhaeva, A.M., Merkulova, E.N., Bondarenkoa, G.N. 2017: Comparative analysis of sequential leaching procedures for dissociation of rare earth elements in gold-bearing material. ISSN 1062-7391 *J Min Sci* 2017 Vol 53 No 6: 1124–1132
- Varshal, G. M., T. K., Velyukhanova, D. N., Chkhetiya, 2000: "Sorption on Humic Acids as a Basis for the Mechanism of Primary Accumulation of Gold and Platinum Group Elements in Black Shales," *Litol. Polezn. Iskop.* 35 (6), 605–612 (2000) [*Lithol. Miner. Resour.* 35 (6), 538–545.

- Varga, E., Bella, M. & Benocs, S.K. 1972: Comparative survey of the trends of trace elements concentration in Hungarian coal fields. Puhl. Hung. Min. Res. Inst., No. 15, 221-236
- Vikent'ev, I.V., Moloshag, V.P., Yudovskaya, M.A. 2006: Speciation of noble metals and conditions of their concentration in massive sulphide ores of the Urals. *Geol Ore Deposits* 48 (2): 77–107
- Virágh, K. & Vincze, J. 1967: A mecseki uránérclelőhely képződésének sajátosságai. (Specialty of uranium deposit formation in the W-Mecsek; in Hungarian). *Földtani Közlöny*, 97/1, 39-59.
- Vincze, K. 1987: A mecseki felsőperm uránércesedésének vizsgálata modellkísérletekkel. *Földt. Közlöny, Bull. of the Hungarian Geol. Soc.* 117. 347—373
- Vincze, J., Sólymos, G, Ditrői Puskás Z, Kósa, L. 2011: Uranium-ore micro-veins in granite from the western part of the Mecsek Mts (Hungary). *Földtani Közlöny* 141(4):325–339 (in Hungarian with English abstract).
- Vladimirov, A.G., Kruk, N.N., Khromykh, S.V., Polyansky, O.P., Chervov, V.V., Vladimirov, V.G., Travin, A.V., Babin, G.A., Kuibida, M.L., Khomyakov, V.D., 2008: Permian magmatism and lithospheric deformation in the Altai caused by crustal and mantle thermal processes. *Russ. Geol. Geophys.* 49, 468–479.
- Volkov, A.V, Sidorov, A.S. 2017: Invisible Gold *Vestnik Rossiiskoi Akademii Nauk* Vol 87 No 1: 40–49
- Windley, B.F., Alexeiev, D., Xiao, W., Kroner, A., Badarch, G., 2007: Tectonic models for accretion of the Central Asian orogenic belt. *J. Geol. Soc. Lond.* 164, 31–47.
- Waples, D.W. 2002: The kinetics of in-reservoir oil destruction and gas formation: constraints from experimental and empirical data and from thermodynamics. *Org Geochem* 31: 553–575
- Ward, C.R., & Gurba, L.W. 1998: Occurrence and distribution of organic sulphur in macerals of Australian coals using electron microprobe techniques. *Org. Geochem.* Vol. 28, No. 11, pp. 635-647
- Weizhen, T., Haiming, L., Jinghui, Zh., Yanzhu, G. 2017: Preparation characterization and the adsorption characteristics of lignin/silica nanocomposites from cellulosic ethanol residue *RSC Adv* 2017/7: 41176-41181
- Wood SA 1996 The role of humic substances in the transport and fixation of metals of economic interest (Au Pt Pd U V): *Ore Geol. Rev.* 11: 1-33

- Wood, S.A. 1996: The role of humic substances in the transport and fixation of metals of economic interest (Au Pt Pd U V): *Ore Geol Rev* 11: 1-33
- Wong, K., Zhou, M, Terry, W., O'Brien, H., Lahaye, Y., Jacky, S. 2017: Constraints of fluid inclusions and in-situ S-Pb isotopic compositions on the origin of the North Kostobe sediment-hosted gold deposit Eastern Kazakhstan. *Ore Geol Rev* 81: 256–269
- Wu, X., & Delbove, F. 1989: Hydrothermal synthesis of gold-bearing arsenopyrite. *Econ Geol* 84: 2029–2032
- Wu, Zh., Xiaoming, S., Huifang, X., Hiromi, K., Yan, W., Chi, W, Yingzhi, D., Xiguang, D., Miao, Y. 2016: Occurrences and distribution of “invisible” precious metals in sulphide deposits from the Edmond hydrothermal field Central Indian Ridge *Ore Geol Rev* 79: 105–132
- Yue, L., Jiaoa, Y., Wua, L., Ronga, H., Fayekc, M., Xie,H. 2020: Evolution and origins of pyrite in sandstone-type uranium deposits, northern Ordos Basin, north-central China, based on micromorphological and compositional analysis. *Ore Geol. Rev.* 118 (2020) 103334
- Yuguang, H, Yaqi, L, Sheng, H, Yukun, L.Zh.F., Yingrui, S. 2017: Distribution and Thermal Maturity of Devonian Carbonate Reservoir Solid Bitumen in Desheng Area of Guizhong Depression South China *Hindawi Geofluids Volume 2017 Article ID 4580416*: 1-15
- Zairi, N.M., Gluhov, A.P., Vasuta, Ya.V. 1987: Isotopic-geochemical model of gold deposits. *Soviet Geology No 6*: 101-108
- Zhautikov, T.M., & Maulenov, A.M. 1985: Types of stratiform gold of Kazakhstan mineralisation *Izv Akad Nauk Kazakh SSR Ser Geol No 5*: 81–87 (in Russian)
- Zheng, Y., Zhang, L., Chen, Y.J., Hollings, P., Chen, H.Y. 2013: Metamorphosed Pb–Zn–(Ag) ores of the Keketale VMS deposit, Xinjiang: evidence from ore textures, fluid inclusions, geochronology and pyrite compositions. *Ore Geology Reviews* 54, 167–180.
- Zhu, L.-M, Liu, X-F, Jin, J-F, & He, M-Y. 1998: The study of the time-space distribution and source of ore-forming fluid for the fine-disseminated gold deposits in the Yunnan-Guizhou-Gangxi area. *Scientia Geologica Sinica*, 33(4): 463-473. (In Chinese).
- Zhu, Y., Fang, A., Juanjuan, T. 2011: Geochemistry of hydrothermal gold deposits: A review *Geosci Front* 2(3): 367-374

9. Appendices

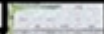
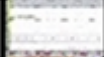









Era	System	Million	Lithostratigraphy	Lithology	Thickness (m)	Description
Mesozoic	Triassic	245	Patacs Siltstone Form.		100	Red and green marine siltstone and claystone
			Jakabhegy Sandstone Formation		250	Red continental (alluvial+delta), marine (beach and shallow water) sandstone, conglomerate
			Kővágószőlős Sandstone Formation		1200	Red alluvial sandstone, conglomerate (Cserkút and Tótvár)
						Uranium ore
						Grey alluvial sandstone with coal impregnations (Kővágótöttös)
						Alluvial sandstone (Bakonya)
					1000	Red limnic claystone with albite, siltstone, fine grain sandstone with dolomite concretion and coal impregnations
					1000	Reddish brown alluvial turbidite facies sandstone and conglomerate
					100	Brownish purple rhyolite
					300	Red alluvial sandstone and conglomerate with siltstone interlayer
	300	Mórággy Granite			Crystalline basement: granite, metamorphic rocks	

Figure 7 Stratigraphic column of the W-Mecsek uranium ore deposit (modified after (Barabás, 2013)). (red arrow shows uranium ore zone; blue frame indicates grey sandstone, where has been sampled) (compiled by CoreDRAW Graphics Suite X6).

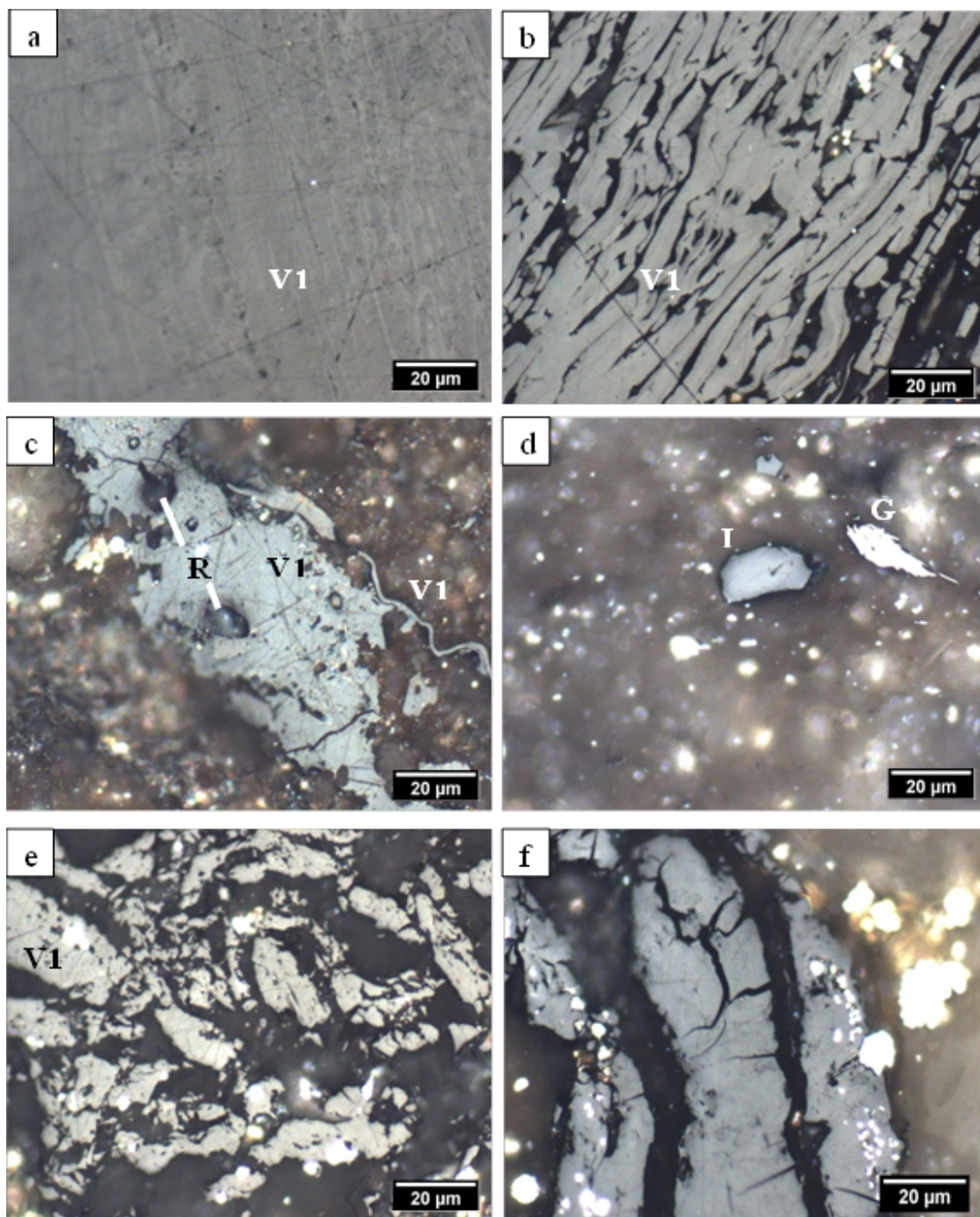


Figure 24 Photomicrographs in reflected normal light with oil immersion: Vitrinite, tellinite particles with wood tissue texture, b) vitrinite with pyrite crystal grains, c) pyrobitumen (PB) with uranium radiation (R) weathering; -dehydration crackings and haloes-and pyrite framboids at left to the OM up and to the right vitrinite particles (a-b-c – WH2-073 sample); d) Inertinite (I) in the middle and graphite (G) to the right (WH2-076 sample); e) Reworked fractured vitrinite in the quartz matrix due to hydrothermal crystal grow (WH2-070 sample); f) Dehydrated vitrinite particles with cracks due to radioactive decay (WH2-065 sample).

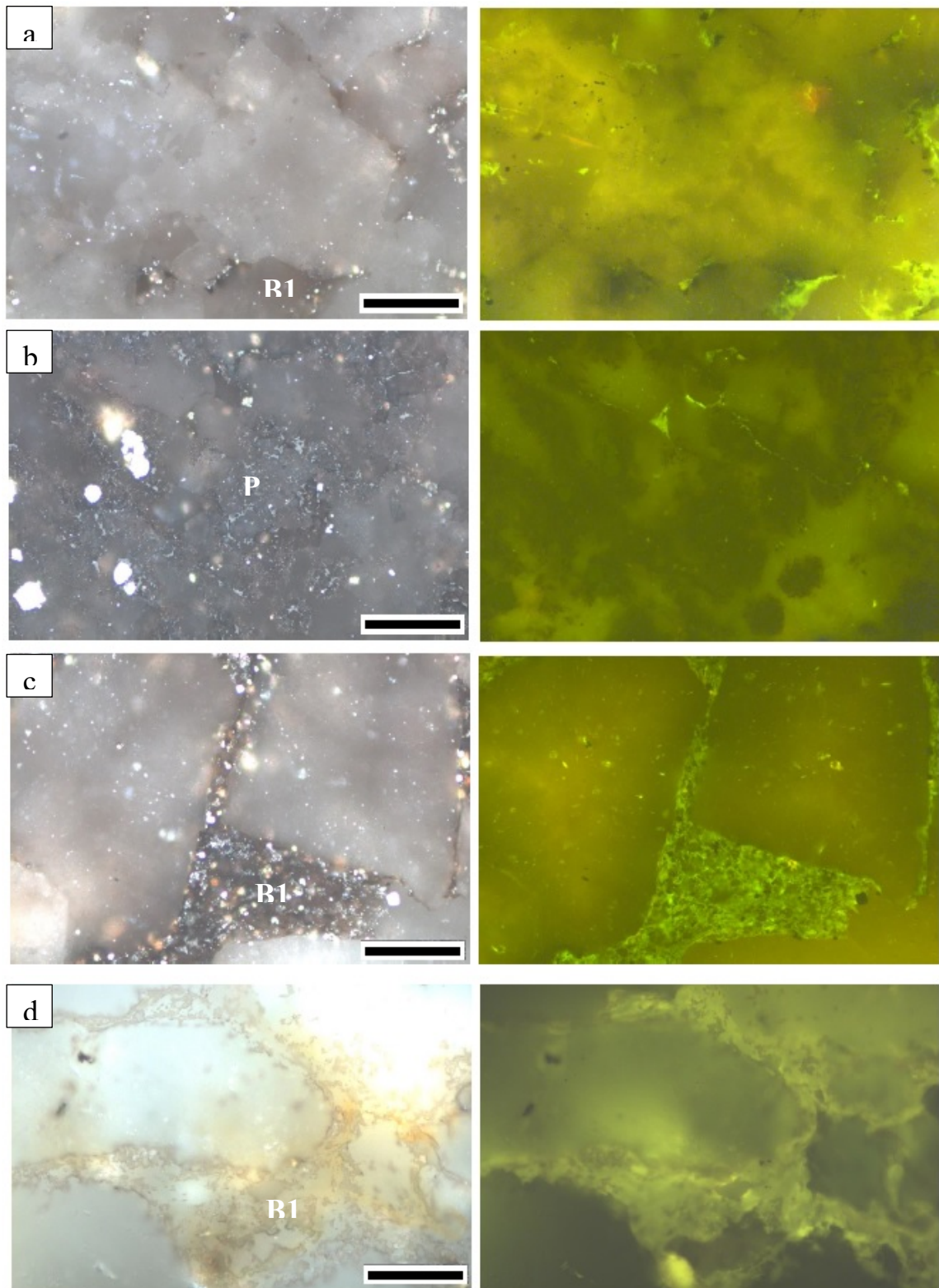


Figure 41 Photomicrographs in reflected normal light and fluorescence UV light excitation with oil immersion: a and b) Homogeneous grey solid bitumen and brownish bitumen, the green FL may reflect some U concentration in the fluidum (WH2-077 sample); c and d) brownish bitumen, the green FL may reflect some U concentration in the fluidum (WH2-077 and WH2-009 samples). Scale – 50 μm

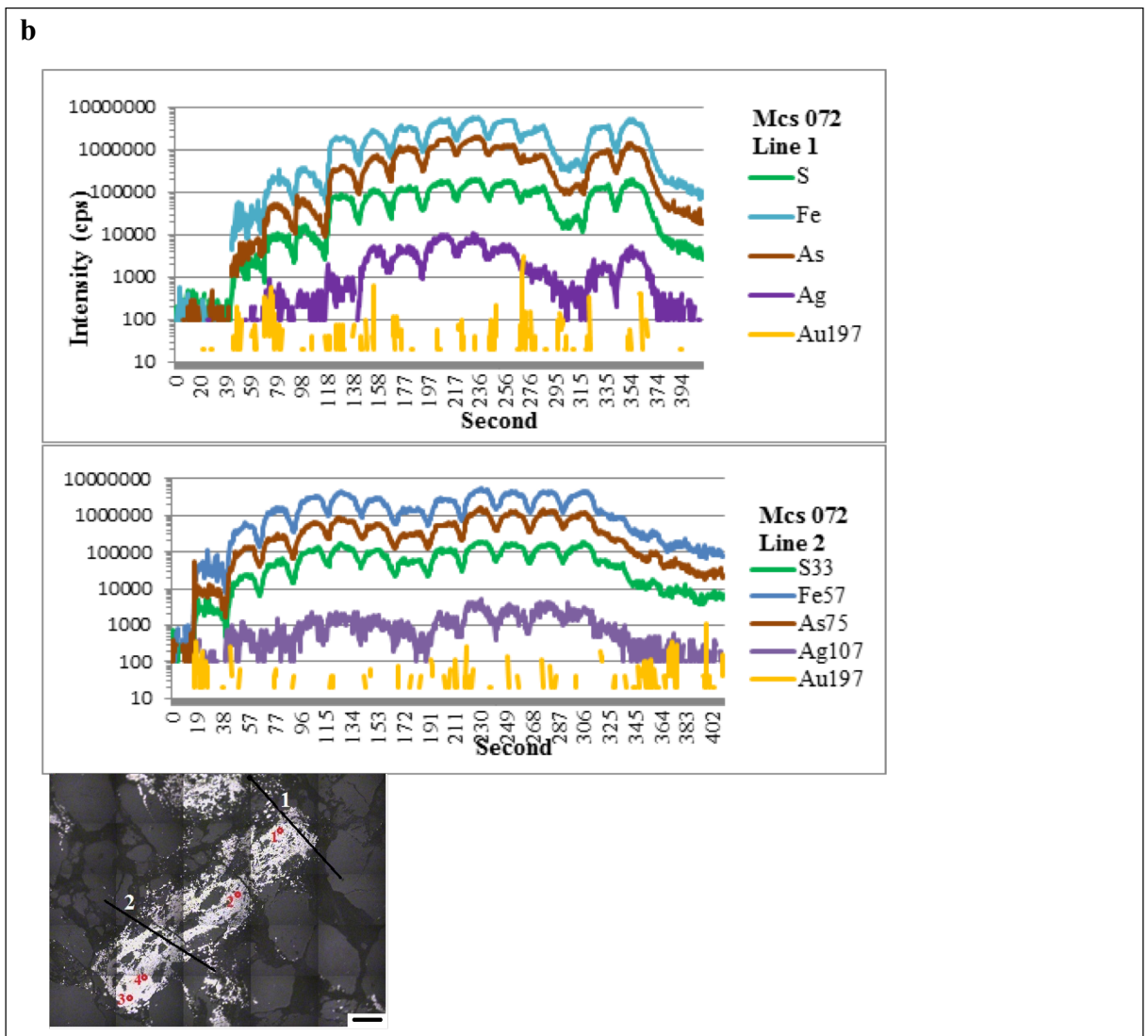
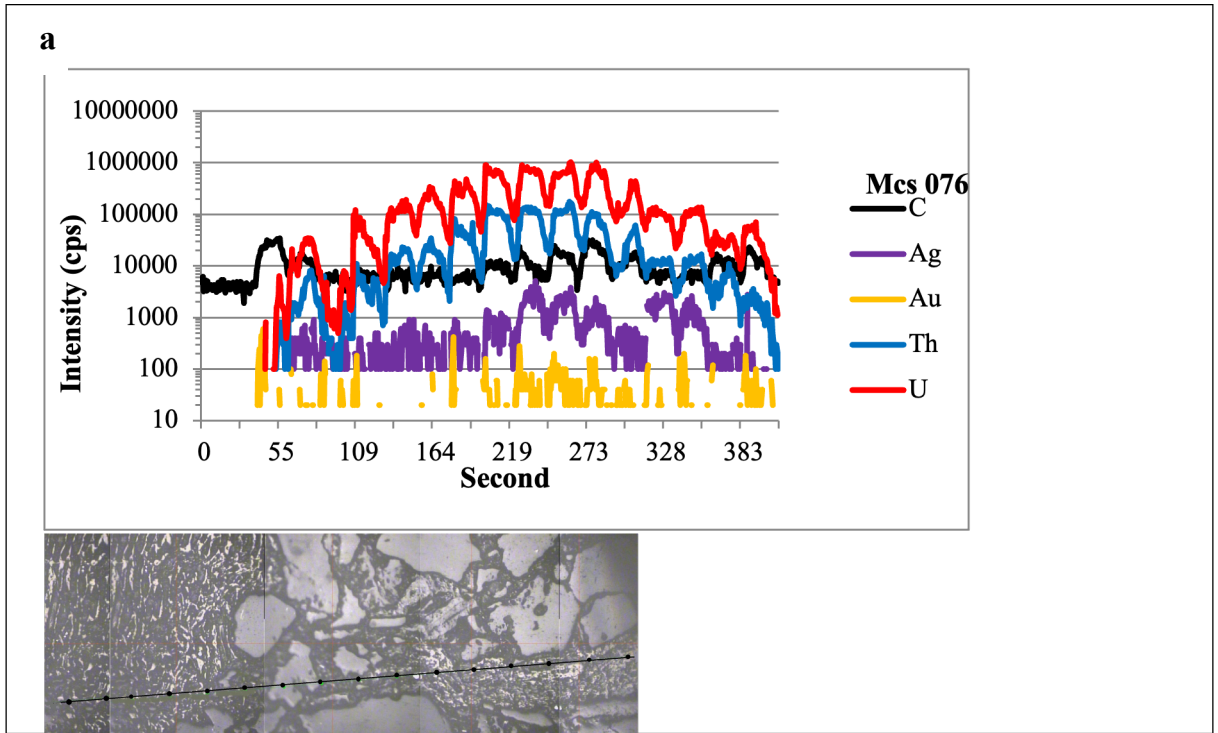


Figure 42 LA-ICP-MS data: a) LA-ICP-MS representative time-resolved depth profiles for Au, Au, U and Th along a linear track through grains of OM in the sample of WH2-076 measuring the line of 16 spots showing LA-ICP-MS image with a laser line burnt across; b) Representative time-resolved LA-ICP-MS depth profiles for Au, Ag, As, Fe and S along two cross-line tracks through the grain of pyrite in the sample of WH2-072 measuring the line 1 of 13 spots and the line 2 of 15 spots showing LA-ICP-MS image with a laser line burnt across. Images scale 100 μm .

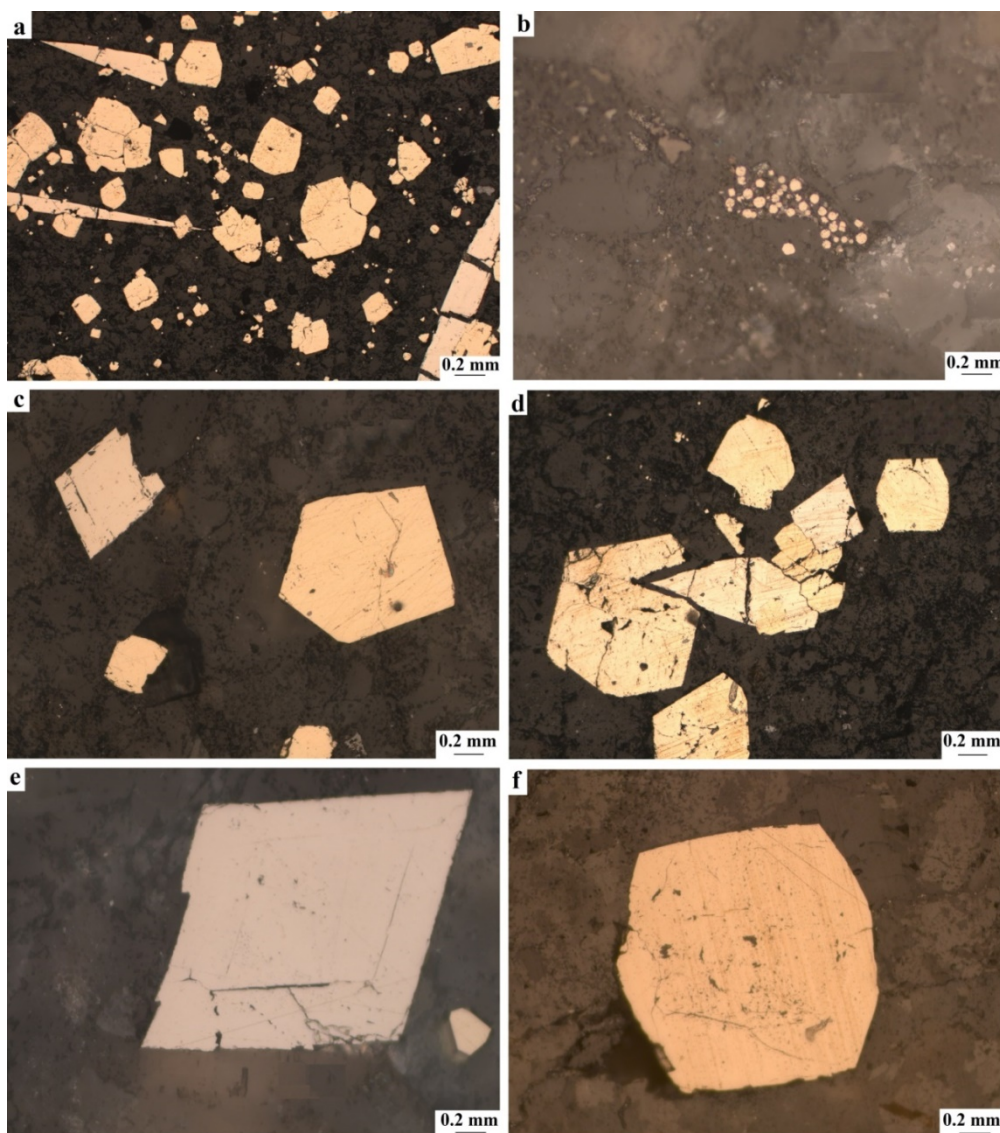


Figure 43 Reflected light micrographs. Bakyrchik deposit: Rock sample of “A”: (a) Hexahedral pyrite crystal with acicular-prismatic arsenopyrite; (b) Pyrite framboidal aggregate; (c) Pentagonal pyrite cross-sections and tabular arsenopyrite twin; (d) hexahedral pyrite in growth with tabular arsenopyrite; (e) Tabular-arsenopyrite twin. Rock sample of “B”: (f) Hexahedral crystal of pyrite.

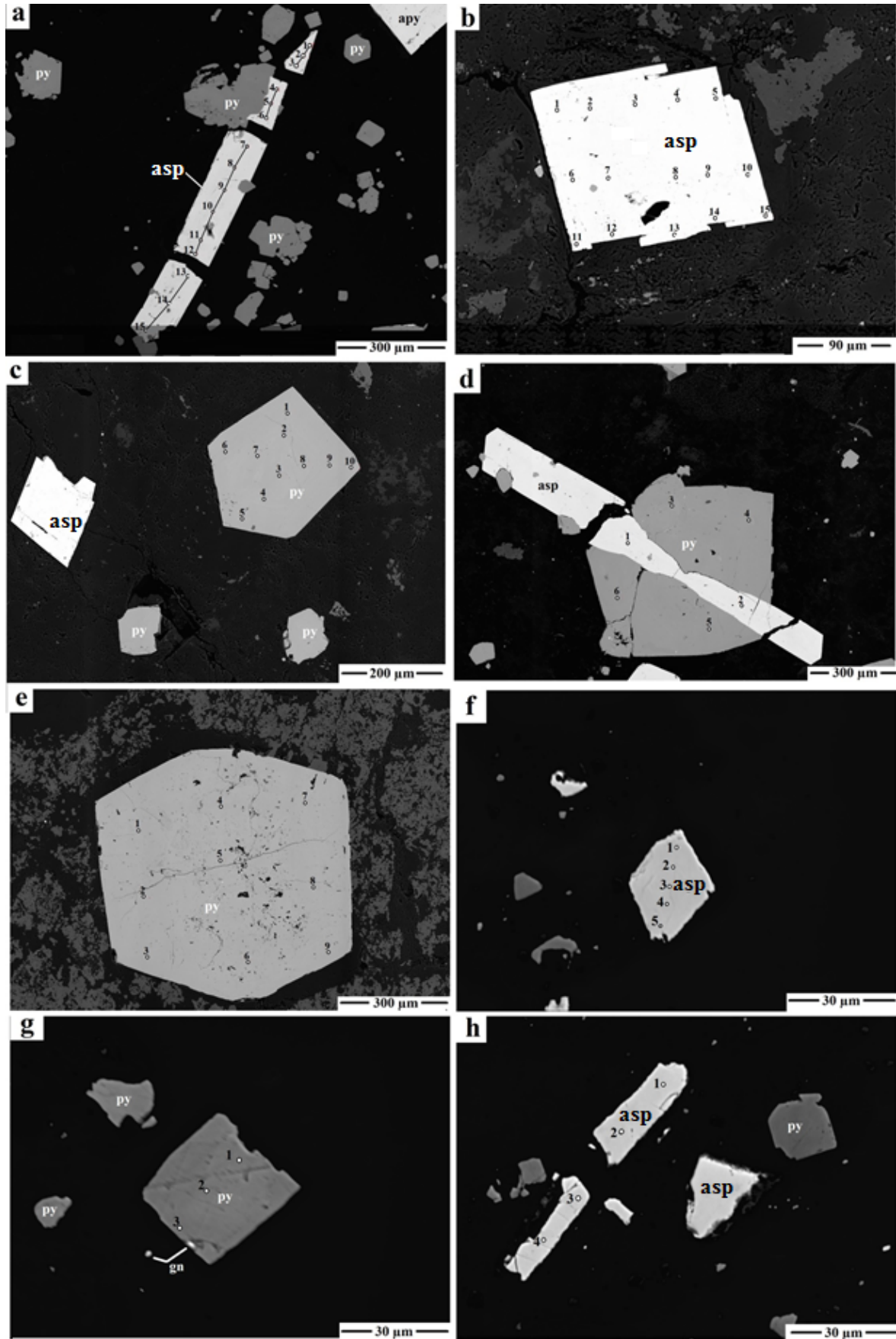


Figure 44 Micrographs of sulphide minerals with points for elemental measurement: a) acicular-prismatic arsenopyrite associated with cubic pyrite crystals, b) tabular-arsenopyrite twin, c) pentahedral pyrite crystal with tabular-arsenopyrite twin, d) integration of acicular-prismatic arsenopyrite and pentahedral pyrite crystal; e) hexahedral pyrite crystal; f) tabular arsenopyrite crystal, g) cubic pyrite crystal with galena inclusion, h) acicular-prismatic arsenopyrite with crystals of cubic pyrite. (asp-arsenopyrite, py-pyrite, gn-galena).

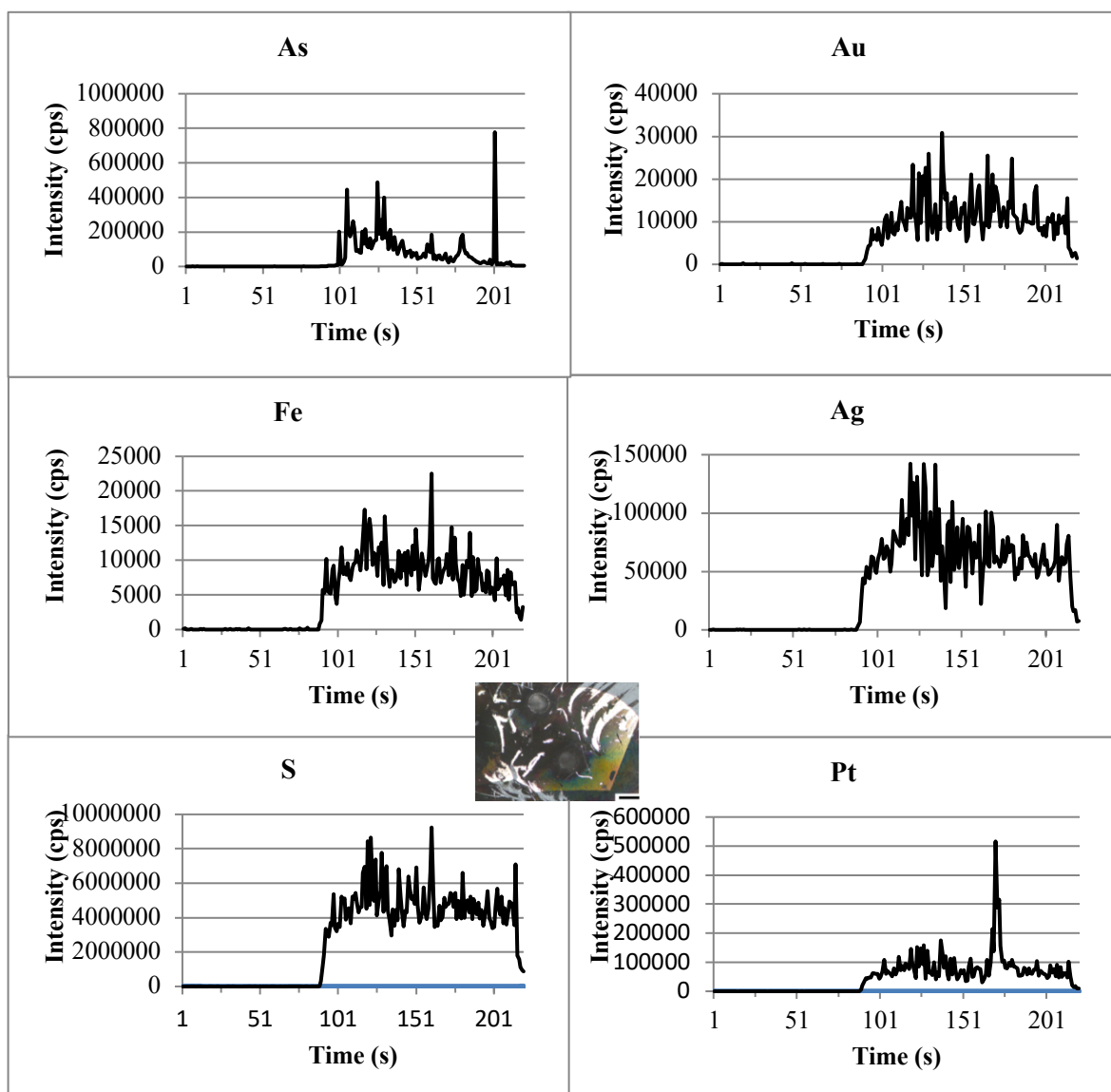


Figure 45 Representative time-resolved LA-ICP-MS depth profiles for Au, Ag, As, Pt, Fe and S along a liner track through grains of arsenopyrite in the sample of Bak 2.4. (Scale is 100 μm in the photomicrograph).

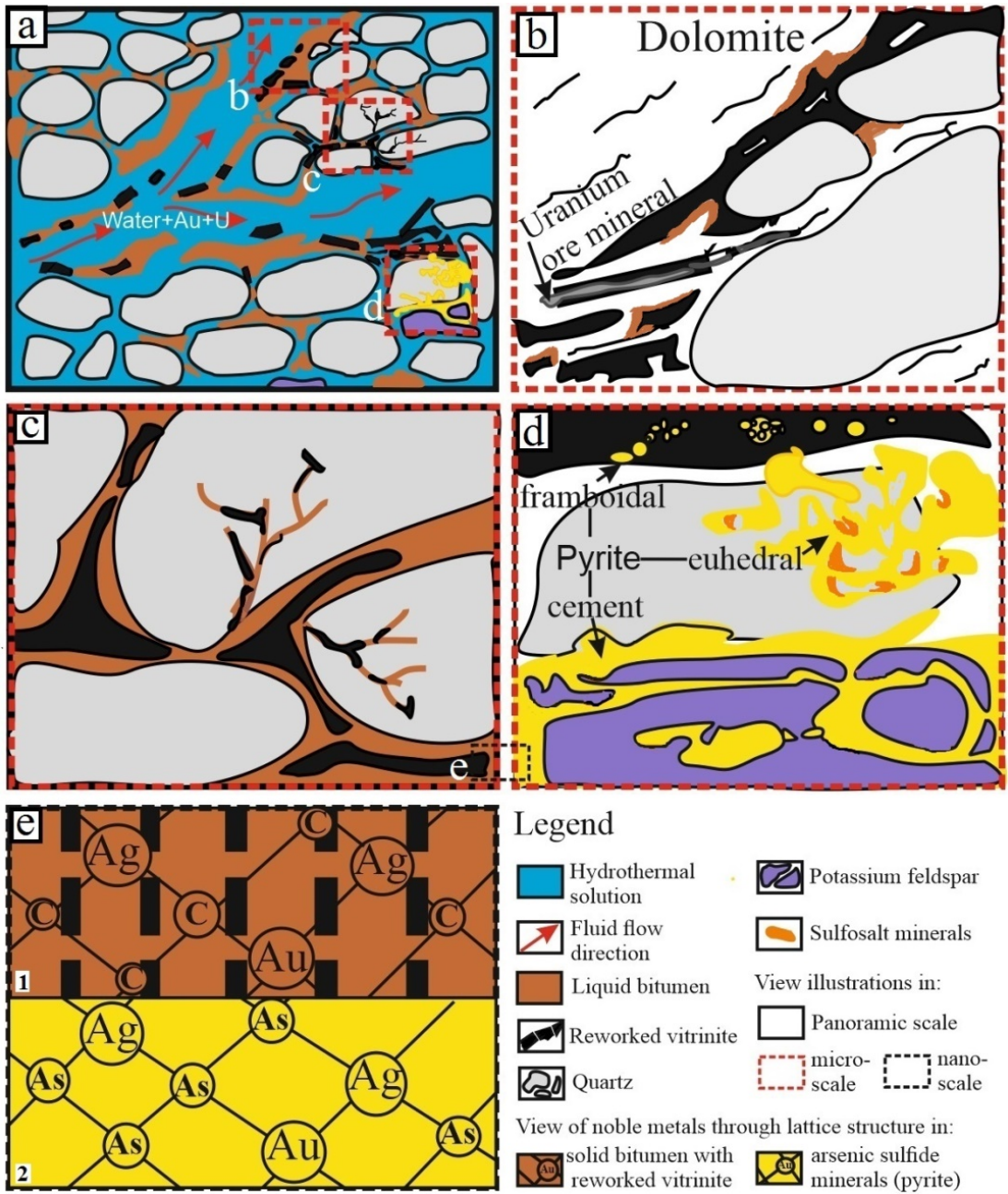


Figure 46 Schematic model formation of gold within OM and arsenic sulphide ore minerals of the W-Mecsek deposit.

Detailed view at the micron size (a-d) and nano-size (e).

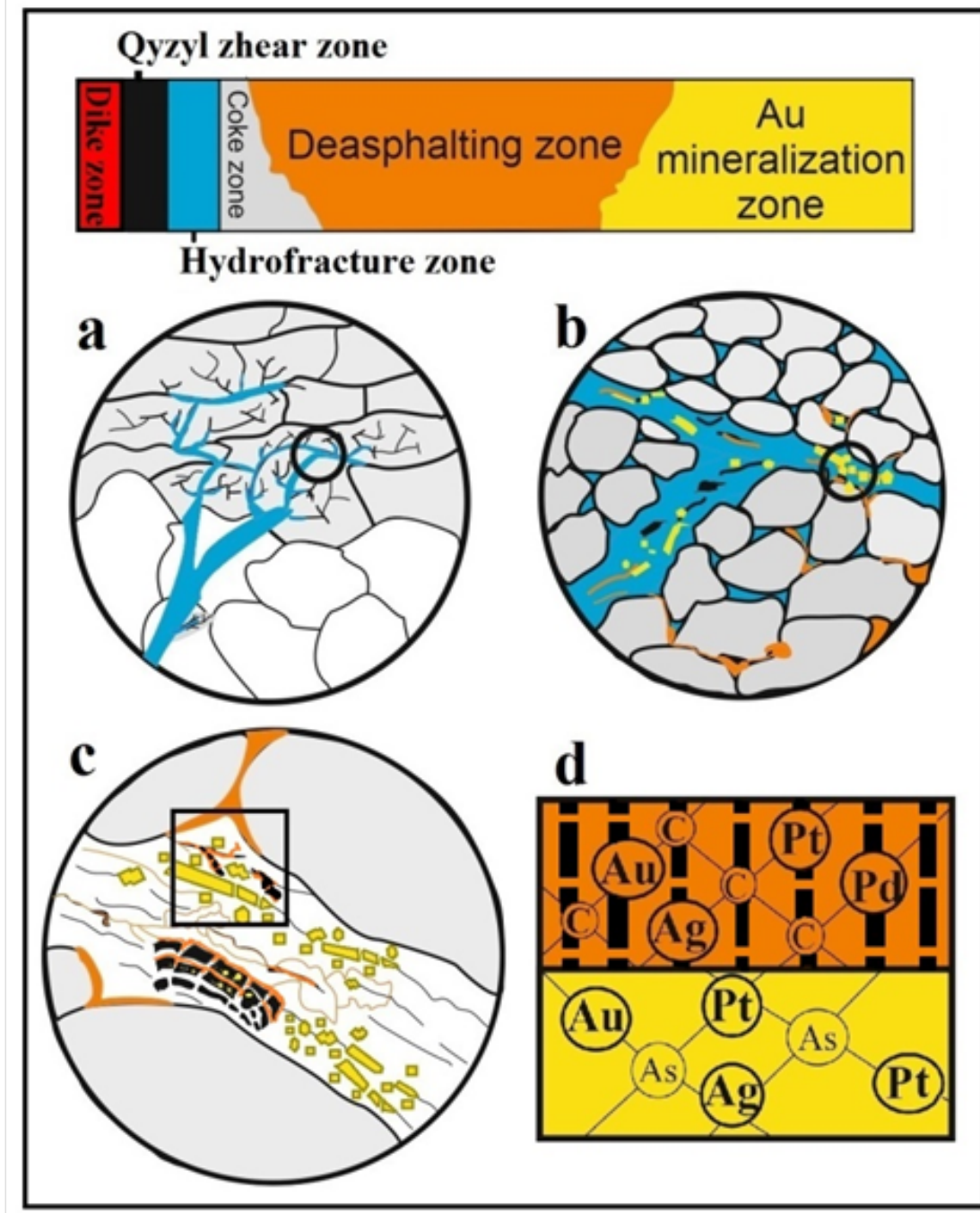


Figure 47 Schematic model of the formation of gold compounds of OM and arsenic sulphide ore minerals in six active zones of the Bakyrchik gold deposit.

Detailed view at the micron size (a-c) and nano-size (d).

Table 11 Sampling preparation of W-Mecsek and Bakyrchik

№	Samples	Sampling preparation and used analytical methods		
		Powder samples (piece)	polished sections (2 pieces for W-Mecsek) (3 pieces for Bakyrchik)	thin sections (1 piece)
Sampling preparation of W-Mecsek				
1	WH2-057	WD-XRF, XRPD, FTIR, OEA, ICP-OES	EMPA, OPM, Raman	-
2	WH2-065	WD-XRF, XRPD,	EMPA, OPM, Raman, LA-ICP-MS	OPM
3	WH2-070	WD-XRF, XRPD,	EMPA, OPM,	OPM
4	WH2-071	WD-XRF, XRPD,	EMPA, OPM,	-
5	WH2-072	WD-XRF, XRPD,	EMPA, OPM, Raman, LA-ICP-MS	OPM
6	WH2-073	WD-XRF, XRPD, FTIR, OEA, ICP-OES; 2 for Soxhlet	EMPA, OPM, Raman, LA-ICP-MS	-
7	WH2-076	WD-XRF, XRPD,	EMPA, OPM, LA-ICP-MS	OPM
8	WH2-077	WD-XRF, XRPD, FTIR, OEA, ICP-OES, 2 for Soxhlet	EMPA, OPM,	-
Sampling preparation of Bakyrchik				
1	Bak 1	WD-XRF, XRPD, ICP-OES	EMPA, OPM, Raman	-
2	Bak 2	WD-XRF, XRPD, OEA, ICP-OES	EMPA, OPM, Raman, LA-ICP-MS	OPM
3	Bak 2.5	WD-XRF, XRPD, FTIR, OEA, ICP-OES	EMPA, OPM, LA-ICP-MS	OPM
4	Bak 2.1	WD-XRF, XRPD, FTIR, ICP-OES	EMPA, OPM,	OPM
5	Bak 2.2	WD-XRF, XRPD, FTIR, OEA; ICP-OES, 2 for Soxhlet	EMPA, OPM,	-
6	Bak 2.3	WD-XRF, XRPD, ICP-OES	EMPA, OPM,	-
7	Bol	WD-XRF, XRPD, ICP-OES	EMPA, OPM,	-
8	Bak 2.4	WD-XRF, XRPD, OEA, ICP-OES	EMPA, OPM, Raman, LA-ICP-MS	OPM
9	Bak 2.25	WD-XRF, XRPD, ICP-OES, 2 for Soxhlet	EMPA, OPM, Raman	-
Total samples (pieces)		65	43	8

Note: without number in the column of powder samples is 1 piece for the analytical equipment;

Abbreviations: WD-XRF - Wavelength Dispersive X-ray fluorescence; XRPD - X-ray powder diffraction; and FTIR - Fourier-transform infrared spectroscopy; Soxhlet -Soxhlet bitumen extraction; ICP-OES- inductively coupled plasma-optical emission spectroscopy; LA-ICP-MS laser ablation inductively coupled plasma mass spectrometry; EMPA-electron probe microanalysis, OPM-optical microscope, Raman - Raman microscope; OEA-organic elemental analyser.

Table 12 Quantitative results of minerals and amorphous organic matter from eight whole-rock samples of W-Mecsek.

	Samples
--	---------

Contents	WH2-057	WH2-065	WH2-070	WH2-071	WH2-072	WH2-073	WH2-076	WH2-077
<i>Minerals</i>	<i>Mineralogical composition (unit, wt%)</i>							
Amorphous matter	4.0	7.0	6.0	31.0	17.0	4.0	7.0	6.0
Pyrite	-	0.6	9.1	14.4	33.4	2.6	0.8	2.2
Quartz	35.2	34.8	42.9	0.9	5.4	22.7	31.5	14.2
Muscovite	16.2	-	-	-	-	-	-	-
Albite	9.9	12.1	10.5	-	1.8	11.0	10.9	3.0
Microcline	-	16.6	14.7	-	12.0	16.0	16.2	9.1
Ankerite	8.3	2.3	1.9	15.8	8.7	1.1	0.6	6.3
Mg-siderite	-	-	-	-	-	3.4	-	-
Mn-siderite	-	-	-	-	-	1.4	-	-
Dolomite	19.6	2.8	2.9	37.9	21.5	9.9	4.0	47.3
Smectite	0.3	1.2	0.9	-	-	1.3	0.9	-
Kaolinite	-	1.0	-	-	-	1.6	0.4	1.2
Illite	6.0	19.8	10.1	-	0.2	25.0	22.7	10.7
Titano-magnetite	0.5	1.8	1.0	-	-	-	0.3	-
Chlorite	-	-	-	-	-	-	4.7	-
<i>Oxide</i>	<i>Chemical composition (unit, wt%)</i>							
SiO ₂	57.8	63.3	65.3	1.2	13.8	51.7	62.1	30.3
Al ₂ O ₃	8.9	16.6	11.3	0.2	2.7	14.5	16.8	5.9
MgO	5.34	1.72	1.4	5.31	4.88	3.59	2.08	10.28
CaO	10.4	1.53	1.45	13.9	10.1	4.06	1.06	17.2
Na ₂ O	1.15	1.26	1.27	0.10	0.20	0.87	1.22	0.45
K ₂ O	3.88	5.67	4.06	0.13	0.99	5.26	6.20	2.66
Fe ₂ O ₃	2.26	1.31	6.71	11.1	19.5	6.24	2.24	3.43
MnO	0.436	0.047	0.042	0.269	0.128	0.155	0.038	0.360
TiO ₂	0.205	0.418	0.179	0.009	0.124	0.584	0.478	0.258
P ₂ O ₅	0.051	0.058	0.040	0.059	0.090	0.097	0.259	0.074
S	0.17	1.0	9.0	27.9	32.4	3.1	0.97	3.0
Differences	9.4	7.0	-	39.7	15.1	9.8	6.7	26.1
<i>Elements</i>	<i>Chemical composition (unit, ppm)</i>							
As	13	43	2301	4265	5027	532	100	354
Cu	< 10	22	101	2662	2345	32	15	23
Zn	18	24	14	315	261	241	41	45
Pb	12	36	89	287	431	117	30	515

Note: Differences show CO₂, water etc.

Table 13 LA-ICP-MS spot analyses measurement on the OM of the sample WH2-065 showing concentrations of trace elements.

Spot numbers	The concentrations of elements (unit, ppm)					
	Ag	Au	As	Fe	Th	U
1	2	3.02	43	8 525	9	46
2	1	0.05	49	9 582	27	101
3	1	5.06	61	7 599	6	61
4	4	0.22	121	38 246	5	10

5	2	0.52	56	13 343	8	26
6	3	0.10	80	24 821	5	8
7	2	0.03	46	12 816	19	29
8	0	0.06	14	6 544	7	14
9	0	0	16	6 709	19	37
10	90	4.52	2 558	101 946	2	18
11	16	1.26	515	27 535	18	44
12	42	2.08	1 528	74 998	5	17
13	30	1.19	897	92 354	10	36
14	2	0.02	123	17 780	16	17
15	4	0.01	264	29 099	13	57
16	3	0.01	153	17 606	17	50
17	1	0.02	41	9 929	27	39
18	8	0.25	306	55 494	14	42
19	11	0.04	330	76 043	14	67
20	1	2.81	49	3 774	2	8
21	2	0.10	71	26 914	10	88
22	1	0.10	27	10 483	11	50
23	1	0.06	28	6 780	1	7
24	0	0.11	10	28 352	1	18
25	0	0.05	6	714	4	8
26	0	0.02	11	2 447	6	10
27	0	0.02	12	13 885	1	8
28	0	0.01	114	8 452	222	241
29	2	0.02	85	29 678	8	15
30	2	0.03	170	15 992	121	495
31	2	0.04	41	16 590	15	24
32	13	0.25	435	37 818	14	48
33	9	0.03	211	39 363	84	203
Average	7.7	0.67	256.7	26 431	22.4	58.8

Table 14 LA-ICP-MS spot analyses measurement on the grains of pyrite of the sample WH2-072 showing concentrations of trace elements.

Spot Numbers	Elemental concentrations of cement pyrite (unit, ppm)								
	Al	Si	Ti	Mn	Fe	Ni	Cu	Zn	As
1	5 877	38 262	113	41	465500	96	458	22	22301
2	3 792	17 819	24	55	465500	95	497	18	28452
3	10 535	16 244	409	117	465500	244	295	14	16181
4	5 413	23 978	32	20	465500	109	674	58	25146
Average	6 404	24 075	145	58	465500	136	481	28	23020
Spot Numbers	Elemental concentrations of euhedral pyrite (unit, ppm)								
	Al	Si	Ti	Mn	Fe	Ni	Cu	Zn	As
1	5 810	21 814	162	17	465500	81	2 366	391	22504
2	2 890	9 677	47	33	465500	66	1 206	189	24806
3	2 216	4 177	14	25	465500	111	3 513	523	15805
Average	3 638	11 889	74	25	465500	86	2361	367	21083

Table 15 Continued

Spot Numbers	Elemental concentrations of cement pyrite (unit, ppm)								
	Sr	Nb	Mo	Ag	Sb	Ba	W	Au	Pb
1	3	0.94	710	36	20	40	0.13	0.26	890
2	2	0.23	711	43	20	26	0.05	0.20	1028
3	18	0.37	552	31	17	7	0.11	0.67	1102
4	2	1.59	666	34	25	36	0.07	0.22	837
Average	6	3	659	36	23	27	0.09	0.34	964
Spot Numbers	Elemental concentrations of euhedral pyrite (unit, ppm)								
	Sr	Nb	Mo	Ag	Sb	Ba	W	Au	Pb

1	3	0.47	768	24	72	10	0.15	0.46	669
2	2	0.14	910	26	40	7	0.09	0.29	605
3	1	0.02	403	18	80	2	0.03	0.22	4803
Average	2	0.21	693	23	64	6	0.09	0.32	2025

Table 16 Quantitative results for minerals and amorphous matter from nine whole-rock samples.

Contents	Samples								
	Bak 2	Bak 1	Bak 2.5	Bak 2.2	Bak 2.3	Bak 2.1	Bol	Bak 2.4	Bak 2.25
<i>Minerals</i>	<i>Mineralogical composition (unit, wt%)</i>								
Amorphous matter	14	10	-	12	14	8	8	-	9
Pyrite	-	-	-	32.7	21.4	2.9	2.6	-	1.4
Arsenopyrite	-	-	-	12.5	10.3	2.2	-	-	1.5
Stibnite	-	-	-	-	-	-	7.7	5.2	-
Valentinite	-	-	-	-	-	-	3.9	3.9	-
Quartz	24	15.8	41.5	25	31.1	41.4	63.7	80.4	36.2
Muscovite	20.6	32.9	-	-	-	7.9	13.7	-	9
Albite	2.9	20.8	-	0.1	2.6	13.3	0.4	0.7	15.3
Ankerite	-	3.3	-	3.4	2.8	2.7	-	-	2.2
Siderite	38.5	6.3	-	-	-	-	-	-	-
Smectite	-	2.4	-	14.3	-	-	-	-	-
Illite	-	8.5	28.7	-	17.3	21.4	-	9.8	25.2
Digenite	-	-	0.5	-	-	-	-	-	-
Dolomite	-	-	-	-	0.5	-	-	-	-
Gypsum	-	-	0.5	-	-	-	-	-	-
Dravite	-	-	19.9	-	-	-	-	-	-
Rutile	-	-	8.9	-	-	-	-	-	-
Anatite	-	-	-	-	-	0.2	-	-	0.2
Biotite	-	-	-	-	0.1	0.2	-	-	0.2
<i>Oxide</i>	<i>Chemical composition (unit, wt%)</i>								
SiO ₂	37.1	51.5	58.4	34.1	47.4	60.7	19.4	74.0	60.2
Al ₂ O ₃	11.9	23.3	17.7	8.8	11.2	19.3	0.9	6.0	18.2
MgO	1.92	0.93	1.38	1.17	1.18	0.95	0.03	0.2	0.86
CaO	1.01	0.75	0.73	1.71	1.45	1.14	-	<0.01	1.13
Na ₂ O	0.27	1.97	0.76	0.25	0.34	1.60	0.03	0.16	1.73
K ₂ O	2.17	4.02	2.40	1.37	1.84	3.04	<0.01	0.95	2.91
Fe ₂ O ₃	29.8	4.51	5.96	23.1	18.1	4.87	0.07	0.25	3.83
MnO	0.733	0.049	0.061	0.028	0.030	0.036	<0.005	<0.005	0.035
TiO ₂	0.432	0.878	0.893	0.231	0.323	0.690	0.006	0.116	0.710
P ₂ O ₅	0.504	0.125	0.145	0.618	0.195	0.012	<0.005	0.007	0.009
S	2.6	0.25	0.9	27.3	19.1	2.8	26.3	3.9	2.2
Differences	11.5	11.7	10.6	1.3	-	4.9	53.2	14.4	8.2
<i>Elements</i>	<i>Chemical composition (unit, ppm)</i>								
As	956	1537	4018	34520	35185	17098	346	1902	13100
Sb	-	-	102	124	241	88	-	137000	50
Cu	16	42	55	46	39	51	18	23	24
Zn	97	61	104	17	29	218	-	10	100
Pb	835	1304	17	15	11	27	336	35	-

Note: Differences: CO₂, water etc.;

Group I has samples of Bak 2, Bak 1, Bak 2.5; Group II includes Bak 2.2, Bak 2.3, Bak 2.1; and Group III has samples of Bol, Bak 2.4, Bak 2.25

Table 17 Concentrations of extracted noble metals of whole-rock samples at the 3 stages (unit, ppm for Au and Ag; ppb for Pt and Pd).

Elements	Samples group I			Samples group II			Samples group III		
	Bak 2	Bak 1	Bak 2.5	Bak 2.3	Bak 2.2	Bak 2.1	Bol	Bak 2.4	Bak 2.25
Stage 1 (pyrite)									
Au	0.1	0.13	0.09	0.08	0.05	0.13	0.01	0.10	0.05
Ag	-	-	1.4	0.4	1.1	2	-	0.4	1.4
Pt	-	-	-	-	-	130	-	-	100
Pd	-	-	-	-	-	-	-	-	-
As	13	4	4.5	43.2	3608	295	-	68.8	4.5
Fe	8297	13044	3757	1556	10261	1339	-	1824	130
S	8450	4272	467	2236	6829	2431	-	27	175
Stage 2 (solid pyrobitumen)									
Au	2.0	3.0	0.21	0.19	0.22	0.76	0.20	0.44	0.21
Ag	1.7	1.7	-	0.12	0.01	0.32	-	-	-
Pt	-	-	5	-	25	-	-	-	1
Pd	-	-	10	-	-	-	-	-	16
As	12	7	66	85	138	16.6	-	23	57
Fe	3989	1499	11.5	2507	1003	132	-	948	9.4
S	34	44	129	72	132	28	-	22	24
Stage 3 (arsenopyrite)									
Au	0.5	4.0	0.11	0.81	1.26	2.1	0.40	0.43	0.48
Ag	0.6	27	1.67	0.27	0.62	0.42	-	0.24	1.85
Pt	-	-	-	105	139	-	-	19	-
Pd	-	-	-	-	-	-	-	-	-
As	986	4050	288	5057	4748	1192	-	2381	309
Fe	8700	10400	4177	14285	10923	2527	-	5008	4177
S	2779	5199	156	10246	5954	445	-	1431	156